UNIVERSITY OF CALIFORNIA
Santa Barbara

Cosmic Ray Dynamics in Galaxies and Galaxy Clusters

A Dissertation submitted in partial satisfaction
of the requirements for the degree of

Doctor of Philosophy

in

Physics

by

Joshua Wiener

Committee in Charge:

Professor Peng Oh, Chair

Professor Omer Blaes

Professor Ben Mazin

June 2015

The Dissertation of
Joshua Wiener is approved:

Professor Omer Blaes

Professor Ben Mazin

Professor Peng Oh, Committee Chairperson

June 2015

Cosmic Ray Dynamics in Galaxies and Galaxy Clusters

by

Joshua Wiener

Curriculum Vitæ

Joshua Wiener

Education

2008–2015: Ph.D. in Astrophysics, University of California Santa Barbara, Santa Barbara, CA

2003–2007: Bachelor's Degree in Physics and Mathematics, Cornell University, Ithaca, NY

Research Experience

Sept. 2014: Research Associate, Heidelberg Institute for Theoretical Studies, Heidelberg, Germany. Studied numerical simulations of cosmic ray transport in hydrodynamic setting. Supervised by Christoph Pfrommer.

Fall 2012: Research Associate, University of Wisconsin Madison, Madison, WI. Studied cosmic ray heating in the warm ionized medium of the Milky Way. Supervised by Prof. Ellen Zweibel.

2007–2008: Research Associate, Cornell University, Ithaca, NY. Performed data analysis and computer simulations on particle accelerator cell efficiency for Prof. Hasan Padamsee, Newman Lab.

Summer 2007: LERCIP intern, NASA Glenn Research Center, Cleveland, OH. Analyzed Mars rover photographical data to model the Martian atmosphere.

Summer 2006: RIPS intern, UCLA Institute for Pure and Applied Mathematics, Los Angeles, CA. Worked in group sponsored by Pixar, investigated the computer modeling of large numbers of colliding deformable solids.

Teaching Experience

2012–2013: Teaching Assistant, UCSB College of Letters and Sciences, Santa Barbara, CA. Taught undergraduate EM and quantum courses.

2008–2011: Teaching Assistant, UCSB College of Creative Studies, Santa Barbara, CA. Taught physics courses in first two years of physics main sequence.

2006–2007: Teaching Aide, Cornell University, Ithaca, NY. Assisted students in self-taught lab course Physics 101.

Skills

Programming: Fortran, C++, Java

Languages: Japanese (conversational)

References

Peng Oh

peng@physics.ucsb.edu

805 893 7254

Christoph Pfrommer
christoph.pfrommer@h-its.org
+49 6221 533 271

Ellen Zweibel
zweibel@astro.wisc.edu
608 262 7921

Abstract

Cosmic Ray Dynamics in Galaxies and Galaxy Clusters

Joshua Wiener

Cosmic rays comprise a significant amount of energy in galaxy clusters, and are as energetically important in galaxies as the thermal gas. A careful treatment of cosmic ray transport is necessary to predict dynamics (such as CR driven winds) based on the radio observations which indicate their abundance. Yet the physics of cosmic ray transport are not very well understood. In this dissertation I will discuss how cosmic rays travel through and couple energetically with magnetized plasma, focusing specifically on the effects of streaming and heating in cluster and galactic environments.

Contents

List of Figures

Introduction

Cosmic rays (CRs) comprise a significant amount of energy in the Milky Way - they are in rough equipartition with galactic magnetic fields and thermal gas. Their dynamics thus impact a great deal on the evolution of our galaxy. This dissertation is a collection of work dedicated to understand how cosmic rays evolve in the fluid approximation, and how their resulting transport mechanisms affect observable phenomena in galaxies (i.e. CR driven winds) and galaxy clusters (i.e. radio halos).

I begin with a very broad overview of CR dynamics in the fluid approximation, including the idea of CR self-confinement which will be instrumental in the work described here. An individual CR is just a highly-energetic, charged particle traveling through space. In the presence of a uniform magnetic field, its trajectory can be described by a simple helix twirling around the magnetic field lines. A CR traveling along a magnetic field line in this way can scatter off of irregularities in

the field, changing its pitch angle (the angle between the CR trajectory and the background magnetic field).

If we now consider a large population of CRs traveling along a magnetic field, we can treat the CRs as a fluid if we assume the scattering rate of the CRs off of these magnetic irregularities is fast, by some measure. That is, that the mean free path of CRs to this scattering is small. Modeling CR dynamics in this approximation is then relatively straightforward.

There is a situation where we can reasonably expect this approximation to hold true. A well-known instability involving CRs called the streaming instability was described by Kulsrud and Pearce [58]. Imagine a CR population drifting with some bulk streaming speed v_s with respect to the ambient gas, along the magnetic field. If this streaming speed exceeds the local Alfvén speed (the characteristic speed of magnetohydrodynamic Alfvén waves), this causes Alfvén waves to be unstably generated at a rate that depends on v_s. These waves then act as CR scatterers, scattering CRs in pitch angle until the CRs are isotropic in the frame of the waves. Once isotropy is established the CRs are streaming at the Alfvén speed v_A and the instability shuts off. In this way the CRs are forced to stream at the Alfvén speed.

This picture, where the CRs cannot stream faster than v_A, is referred to as CR self-confinement. The CRs generate the same magnetohydrodynamic (MHD)

waves that they then scatter off. In all of the works presented here, we assume self-confinement holds. This includes the assumption that scattering from external sources of MHD waves is small, such that the CRs are not externally confined. We will see that the self-confinement picture carries along with it a certain energetic coupling between the CRs and the ambient gas, using the magnetic field as an intermediary, that plays an important role in many of the observed phenomena we discuss.

In chapter 1, we discuss how MHD wave damping mechanisms can allow CRs to stream faster than v_A, and how this may affect predictions of radio emission in radio halos in galaxy clusters. In chapter 2 we examine how the energy coupling alluded to above might serve as an additional heating mechanism in certain regions of the Milky Way, potentially explaining observed ion abundances. In chapter 3 we consider the effects of CR dynamics on cold clouds embedded in galactic halos with the aim of predicting the structure of thermal interfaces of clouds. Finally in chapter 4 we present a series of simulations demonstrating the difference in CR dynamics when the self-confinement picture is and is not applicable.

Chapter 1

Cosmic Ray Streaming in Clusters of Galaxies

This article has been accepted for publication in Monthly Notices of the Royal Astronomical Society

http://mnras.oxfordjournals.org/content/434/3/2209

1.1 Introduction

Cosmic rays (CRs) in the intra-cluster medium (ICM) can arise from structure formation shocks [73, 81], turbulent reacceleration of existing non-thermal particles [22], galactic winds and supernovae [109], and radio galaxy jets [37, 39, 71].

They are visible in clusters in radio emission, and gamma-ray emission (via hadronic interactions). However, unlike in our interstellar medium (ISM), CRs in the ICM are energetically subdominant; for instance, current upper limits on CR-induced gamma-ray emission in Perseus suggest CRs are $\lesssim 1-2\%$ of the thermal energy density [2]. Why then are CRs in clusters of astrophysical significance? Firstly, unlike in the ISM, cosmic ray protons (CRp) with $E \lesssim 10^7$GeV remain confined and have lifetimes of order a Hubble time [109, 10]; they therefore encode archaeological information about the cluster assembly history as well as AGN and supernova activity. Secondly, the ICM provides stringent tests of plasma physics in a regime very different from the ISM. CRs in clusters represent an opportunity to study the unknown efficiency of shock acceleration [12] in a low Mach number $\mathcal{M} \sim 1-5$ and high plasma beta $\beta \sim 100$ regime. Transient radio phenomena can also teach us about magnetic field amplification at shocks. Thirdly, even a low level of CRs could have interesting astrophysical implications. These range from pressure support (thus affecting the use of clusters for cosmology) to heating which suppresses cooling flows [51] or energizes filaments [45, 46], and distributing metals and heat via buoyancy-induced turbulent convection [26, 102].

One drawback of cosmological simulations of CRs in clusters is that they generally do not include CR transport processes; the CRs are assumed to be frozen into the gas, and advected with it. In practice, CRs can move relative to the gas

by streaming along magnetic field lines down a CR gradient, as well as diffusing across field lines by scattering off plasma waves. As CRs stream, their momentum anisotropy excites plasma waves, which in turn scatter the CRs, isotropizing the CR distribution in the frame of the waves. This generally limits streaming speeds to the speed of the waves, which is the Alfvén speed $v_{\rm A}$. In our ISM, rapid pitch-angle scattering due to the CR streaming instability[1] [64, 58, 113, 105] can explain the observed spatial isotropy of CRs, as well as the escape time of CRs from the Galaxy [99, 60]. Applying the same CR self-confinement scenario to the ICM, the low implied drift speed of CRs $v_{\rm D} \sim v_{\rm A} \sim 100\,{\rm km\,s^{-1}}$, seems to justify neglect of cosmic ray transport [56]. Early calculations of CRs in isolated clusters [13, 66] which considered CR diffusion at a level comparable to ISM values found it to be negligible as a transport process. They argued that if CRs were injected at the cluster center by an AGN, they would quickly dominate pressure support at a level inconsistent with observations. [51] resolved this in their calculations of CR heating by allowing CRs to be transported by rising buoyant bubbles, as seen in high resolution Chandra images, which are subsequently shredded by Kelvin-Helmholz and Rayleigh-Taylor instabilities to disperse the CRs.

[1] In principle, CRs can also scatter off MHD turbulence, though this is thought to be weak due to the increasing anisotropy at small scales, with power concentrated in modes with wave-vectors transverse to the B-field, while CRs efficiently scatter off the parallel component [25, 118]. Fast magnetosonic modes could potentially scatter CRs more efficiently [22], but a treatment of this is beyond the scope of this paper.

However, this assumption of slow CR streaming and diffusion may not be fully justified. The plasma waves which scatter the CRs are also subject to a variety of damping mechanisms. If damping is stronger in the ICM than in the ISM, then pitch-angle scattering of the CRs off the attenuated waves will be reduced, and the CRs retain some momentum anisotropy in the frame of the waves. They can therefore stream faster than the waves, and will no longer be limited by the Alfvén speed. In principle, if the waves are very strongly damped, the CRs could stream up at speeds up to $\sim c$. While the possibility of super-Alfvénic or even free streaming was appreciated early on [58, 61, 105, 43, 40] — albeit largely in cold clouds in the ISM where ion-neutral damping of Alfvén waves is extremely strong — generally $v_{\rm D} \sim v_{\rm A}$ and diffusion coefficients appropriate for the hot ISM have been uncritically applied to the ICM environment. In an influential recent paper, [36] noted the interesting possibility of super-Alfvénic streaming in the ICM, adopted the sound speed $c_{\rm s}$ as a characteristic streaming speed, and were the first to discuss the wide-ranging observational consequences.

A particularly interesting possibility they focused on was whether the interplay between advection and streaming could be responsible for the observed bimodality seen in radio halo luminosity. Giant radio halos are generally only seen in disturbed clusters which show signs of merger activity. This bimodality has been a stumbling block for hadronic models (e.g., [83]). These models track the long-

lived CR protons (CRp) formed during structure formation shocks, and find that the secondary electrons formed when the CRps undergo hadronic interactions are sufficient to explain radio halo observations. Transience or correlation with turbulence is generally not expected in such models. As a result, radio halos are often attributed to the re-energization of seed electrons by Fermi II acceleration when the ICM turbulence becomes transonic during mergers [23, 22]. As the turbulence dies away, the CR electrons (CRe) cool via synchrotron and inverse Compton emission on a relatively short ($\sim 10^8$ yr) timescale. However, the origin of the seed electrons is uncertain; low energy electrons will rapidly Coulomb cool in the dense cluster center. [36] suggested instead that transonic turbulence advects CRs from the plentiful reservoir on the cluster outskirts. Hadronic interactions of the inwardly advected CRp with the dense central ICM can then produce CRe[2]. Once turbulence dies down, subsequent outward CR streaming switches off the radio halo. This rapid outward streaming also explains why radio halos turn off in the original hadronic scenario, which is otherwise difficult to understand. For these explanations to work, the CR streaming timescale must be relatively short, or $v_{\rm D} \gg v_{\rm A}$. [36] adopted $v_{\rm D} \sim c_{\rm s}$ and examined its implications, but only justified this assumption qualitatively.

[2]Alternatively, low energy relic CRe advected from the cluster outskirts could provide seeds for turbulent reacceleration.

This paper aims to critically examine the possibility that super-Alfvénic streaming could play a crucial role in CR transport in the ICM, by building more quantitative models to clarify its plausibility and importance. It has three main goals: (i) a quantitative calculation of CR streaming speeds in quasi-linear theory and its dependence on plasma parameters, when a variety of wave damping mechanisms are at play. In particular, we consider the effects of non-linear Landau damping and turbulent damping. We also give expressions for parallel diffusivities and CR heating rates in this regime. Of particular interest is the countervailing effects of turbulence: it affects CR transport both by turbulent advection of CRs from the cluster outskirts, as well as damping of CR generated waves, which enables faster outward streaming. We assess their relative importance. (ii) A reevaluation of CR heating due to central injection by an AGN [51], taking these streaming effects into account. (iii) A 1D simulation of radio halo turnoff due to CR streaming, to establish if the required dimming by at least an order of magnitude can take place within a reasonable timescale. We also calculate how the gamma-ray luminosity evolves with time. A non-linear, time-dependent calculation is needed since the streaming speed itself depends on CR energy density. In their analytic calculations, [36] consider a steady-state profile where inward turbulent advection and outward CR streaming are in rough balance. This scenario seems somewhat unlikely; it seems more probable that at a given point in time, either inward advec-

tion or outward streaming dominates. To calculate radio halo turnoff, we consider the latter. These calculations also enable us to compute a fundamental prediction of this model: spectral steepening and frequency-dependent dimming which arise from energy-dependent streaming speeds. We compare these with observations.

The outline of this paper is as follows. In §1.2, we calculate in quasi-linear theory cosmic-ray streaming speeds when different wave damping mechanisms are dominant, and derive expressions for the resulting parallel diffusivity, as well as turbulent diffusion rates. In §1.3, we describe the equations we solve numerically with ZEUS, focusing in particular on the CR transport equation. We describe our initial conditions for the cosmic ray profile, which are tuned to match radio halo observations for the Perseus and Coma clusters. We also present a test case of CR heating by a central AGN. In §1.4, we present the results of simulations of radio halo turnoff due to CR streaming. In §1.5, we show how aspects of these results can be understood analytically. Finally, we conclude in §1.6.

1.2 Cosmic Ray Streaming: Quasi-linear Theory

In this section, we derive the basic equations we use, in particular the streaming speeds and diffusion coefficients which are used in the cosmic-ray transport equation. Our treatment is by design semi-quantitive rather than fully rigorous.

1.2.1 Cosmic Ray Streaming

Resonant Scattering and Wave Growth

We begin by reviewing the classical cyclotron resonance streaming instability[3] [58, 115]. Consider a cosmic ray proton with Lorentz factor γ propagating along a magnetic field line of strength B_0 with cyclotron frequency $\Omega_0 = eB_0/(m_p c)$, gyroradius $r_{\rm L} = \gamma c/\Omega_0$, and pitch angle cosine μ. Since $v_{\rm A} \ll c$, Alfvén waves are perceived by the CR as a spatially varying but time-stationary B-field. An Alfvén wave is resonant with this cosmic ray if the resonance condition

$$k_{\parallel} = \frac{1}{\mu r_{\rm L}} \tag{1.1}$$

[3]Another instability which arises in the context of streaming cosmic rays is the Bell instability [8, 92]; it amplifies the magnetic field and transfers CR energy and momentum to the plasma on scales much less than the CR gyroradius. It only arises in weak-field regimes and thus is not relevant for the ICM. In particular, the criterion for the Bell instability can be written as [124]: $U_{\rm CR}/U_{\rm B} > c/v_{\rm D}$ (where $U_{\rm CR}, U_{\rm B}$ are the energy densities in CRs and B-field respectively), whereas in our models $U_{\rm CR}/U_{\rm B} < 1$, and $c/v_{\rm D} \gg 1$. Note that even in the weak field, low Alfvén speed regime where the Bell instability applies, its maximum growth rate is of order that of the classical resonant streaming instability.

is satisfied. This resonance is a requirement both for the wave to scatter the CR and for the CR to excite the wave. This condition can be easily understood: if the magnetic field changes on a length scale much longer than the projected gyroradius, the CR will simply follow the field line adiabatically, with no change in pitch angle. If the field varies on much smaller scales, the CR will see a rapidly oscillating Lorentz force during its orbit and remain unaffected, essentially only seeing the background field. At resonance, the CR sees a constant field due to the wave, and hence a steady force. The $k_{\|}$ portion of the wave is the relevant one, since it has a transverse magnetic field $\delta B_{\perp}$ which can exert a Lorentz force on the $v_{\|}$ component of a streaming cosmic-ray.

If the distribution of cosmic rays in the frame of the Alfvén waves is completely isotropic, then the effect of a cosmic ray traveling along the magnetic field line in one direction is cancelled by an equivalent cosmic ray traveling in the opposite direction, and there is no wave growth. However, [58] showed that even a slight anisotropy in the cosmic rays–which naturally arises in the presence of sources and sinks–will cause unstable growth in the waves, caused by momentum transfer from the CRs to the waves in the course of pitch-angle scattering. The resulting wave growth rate is [58]:

$$\Gamma_{\rm CR}(k_{\|}) \sim \Omega_0 \frac{n_{\rm CR}(>\gamma)}{n_{\rm i}} \left(\frac{v_{\rm D}}{v_{\rm A}} - 1 \right) \tag{1.2}$$

In the above, $n_{\rm CR}(>\gamma)$ is the number density of cosmic ray protons with energies large enough to be resonant with the Alfvén wave for some pitch angle μ, namely $r_{\rm L} > 1/k_{\parallel}$ (though since the CR spectrum falls off rapidly with energy, generally $k_{\parallel} \sim 1/r_{\rm L}$), $n_{\rm i}$ is the ion density in the plasma, and $v_{\rm D}$ and $v_{\rm A}$ are the cosmic ray streaming and Alfvén speeds respectively. This expression is derived from balancing CR momentum loss with wave momentum gain, but we can understand its main features qualitatively. The rate of wave growth scales with that for momentum loss for a single CR, $\dot{p} \propto p\Omega_{\rm rel} = (\gamma mc^2)(\Omega_{\rm o}/\gamma) \propto \Omega_o$, i.e. the non-relativistic, rather than the relativistic gyro-frequency. This has to be multiplied by the fraction of ions which can drive wave growth, $n_{\rm CR}(>\gamma)/n_{\rm i}$ (non-resonant ions simply provide inertia, slowing down wave growth), and the anisotropy which seeds the wave growth $(v_{\rm D}/v_{\rm A} - 1)$.

The streaming instability causes the waves to grow until pitch-angle scattering renders the CR distribution isotropic in the frame of the waves, i.e. $v_{\rm D} \sim v_{\rm A}$. If we assume $(v_{\rm D}/v_{\rm A} - 1) \sim \mathcal{O}(1)$, we can estimate the growth time of the waves. If we assume that the energy density is CRs is $\sim 10\%$ of the thermal energy density, $\epsilon_{\rm CR} \sim 0.1\epsilon_{\rm therm}$, then $n_{\rm CR}\langle E_{\rm CR}\rangle \sim 0.1 n_{\rm i}\langle E_{\rm i}\rangle$ where $\langle E_{\rm CR}\rangle \sim$ GeV (as is true for most reasonable power-law momentum distributions–e.g., see Fig. 1 of [38]), and $\langle E_{\rm i}\rangle \sim$ keV are the typical energies of CRs and thermal ions respectively, and so $n_{\rm CR}/n_{\rm i} \sim 10^{-7}$. A similar ratio holds in the coronal regions of our Galaxy. For

$\sim \mu$G fields, $\Omega_{\rm o} = eB/mc \sim 10^{-2}\,{\rm s}^{-1}$, implying from equation (1.2) a wave growth time of $\Gamma_{\rm CR}^{-1} \sim 30$ yr, i.e. extremely short.

The above arguments suggest that self-confinement of cosmic-rays is very efficient, and should always reduce the streaming velocities $v_{\rm D} \sim v_{\rm A}$. The general success of the self-confinement picture for our Galaxy means that this has been uncritically assumed in other environments such as the ICM, and/or CR diffusion coefficients scaled to the measured Galactic values. In fact, $v_{\rm D}$, and the associated diffusion coefficient D_θ depend on the amplitude of the wave field $\delta B/B$, which can be calculated by assuming equilibrium between growth and damping. If damping processes are sufficiently strong, then $\delta B/B$ will be insufficient to efficiently confine the CRs, and super-Alfvénic streaming is possible. We now examine this possibility.

Non-linear Landau Damping

Parallel propagating MHD waves do not suffer any linear damping. However, they can undergo non-linear Landau damping when two waves A & B of slightly different frequency interact to form a beat wave. This beat wave can resonantly interact with thermal particles with parallel velocity identical to the wave's phase speed, $v_\parallel = (\omega_{\rm A} - \omega_{\rm B})/(k_{\rm A} - k_{\rm B})$ (for parallel propagating waves, $v_\parallel = v_{\rm A}$). Particles moving more slowly than the beat wave will extract energy from the

wave (thus damping it), while particles moving faster than the wave will add energy to it. For a Maxwellian plasma, typically $(\partial f/\partial v)_{v_\parallel = v_\mathrm{A}} < 0$, and damping dominates.[4] The high frequency wave gives up energy to a combination of the low frequency wave and resonant particles.

To aid in physical insight, we present a simplified derivation of streaming speeds to be expected if non-linear Landau damping dominates, before employing the formulae from more detailed derivations [63, 59, 43]. The damping rate in a high-β plasma is [60]:

$$\Gamma_\mathrm{NL} \approx \frac{1}{2}\sqrt{\frac{\pi}{2}}\left(\frac{v_\mathrm{i}}{v_\mathrm{A}}\right)\left(\frac{\delta B}{B}\right)^2 \omega \approx 0.3\frac{\Omega}{\mu}\frac{v_\mathrm{i}}{c}\left(\frac{\delta B}{B}\right)^2 \tag{1.3}$$

How can we qualitatively understand the first relation? The wave frequency $\omega = k_\parallel v_\mathrm{A}$ sets the fundamental frequency, while interactions involving the beat wave arise to second-order in perturbed field strength $(\delta B/B)^2$. Since the resonant condition $v_\parallel = \mu v_\mathrm{i} = v_\mathrm{A}$ implies that thermal particles with $\mu = v_\mathrm{A}/v_\mathrm{i}$ are resonant, it is clear that the damping rate should depend on this ratio. However, the exact dependence only emerges from a detailed calculation–either by calculating the slope $(\partial f/\partial v)_{v_\parallel = v_\mathrm{A}}$, or from the plasma dispersion relation [48]. Note that since $v_\mathrm{i}/v_\mathrm{A} = \beta^{1/2}/2$, we have $\Gamma_\mathrm{NL} \propto \beta^{1/2}$. In the second relation, we use the dispersion relation $\omega = k_\parallel v_\mathrm{A}$ and the resonance condition, equation (1.1).

[4] In a high β plasma, $(\partial f/\partial v)_{v_\parallel = v_\mathrm{A}}$ is relatively flat for electrons, while still steep for ions; hence, ions dominate the damping rate [72].

In steady state, the Vlasov equation for CRs is [58]:

$$v_z \frac{\partial f}{\partial z} = \frac{\partial}{\partial \mu}\left[\frac{1-\mu^2}{2}\nu(\mu)\frac{\partial f}{\partial \mu}\right] \tag{1.4}$$

where $B = B_z\hat{z}$, $\nu(\mu) \approx \Omega(\delta B/B)^2$ and $v_z = \mu c$. This expresses the condition that the net streaming along field lines is set by diffusion in pitch-angle. In the limit of strong scattering, we can expand $f = f_0 + f_1 + f_2 + ...$ where $f_0(p, z, t)$ is isotropic and $f_1(p, z, t, \mu) \ll f_0$, $f_2 \ll f_1$. Let us also define $\mathcal{F} = f_1/f_0$ and the scale height $L_z(p, z) = f_0/(\partial f/\partial z)$. Integrating both sides of equation (1.4) with respect to μ and dividing by f_0, we obtain:

$$\frac{\partial \mathcal{F}}{\partial \mu} = -\frac{c}{\nu L_z}. \tag{1.5}$$

If we set

$$\mathcal{F} = 1 + \frac{3(v_D - v_A)}{c}\mu \tag{1.6}$$

so that $\langle \mu c \mathcal{F}(\mu)\rangle = (v_D - v_A)$ (i.e., the leading order anisotropy in the distribution function yields the net drift relative to the frame of the waves), this yields:

$$(v_D - v_A) \approx \frac{r_L}{3L_z}\left(\frac{\delta B}{B}\right)^{-2} c \approx \frac{\lambda}{3L_z}c \tag{1.7}$$

where $\lambda \sim r_L(\delta B/B)^{-2}$ is the mean free path. In steady state, the wave growth rate (equation (1.2)) equals the wave damping rate (equation (1.3)). Together with equation (1.7), this gives us two equations which we can solve for two unknowns, v_D and $(\delta B/B)^2$. The result is:

$$\left(\frac{\delta B}{B}\right)^2 = \left(\frac{c}{v_{\rm A}}\frac{c}{v_{\rm i}}\frac{r_0}{3L_{\rm z}}\frac{n_{\rm CR}(>\gamma)}{n_i}\gamma^2\right)^{1/2} \tag{1.8}$$

where $f_0 \propto p^{-n}$ (note that our result differs from [43], who explicitly specialize to $\gamma \sim 5$ for the ISM from the outset). If we scale to numbers characteristic of the ICM, we obtain:

$$\left(\frac{\delta B}{B}\right)^2 = 1.6\times10^{-6}\frac{(n_{-10}^{\rm CR})^{1/2}\gamma_{100}^{(5-n)/2}10^{4.6-n}}{(n_{-3}^{i})^{1/4}B_{\mu\rm G}T_{4\,\rm keV}^{1/4}L_{\rm z,100}^{1/2}} \tag{1.9}$$

where $T_{4\,\rm keV} = (T/4\,\rm keV)$, $B_{\mu\rm G} = (B/1\,\mu G)$, $L_{\rm z,100} = (L_z/100\,\rm kpc)$, $n_{-3}^{\rm i} = (n_{\rm i}/10^{-3}\,\rm cm^{-3})$, $n_{-10}^{\rm CR} = n^{CR}(\gamma > 1)/10^{-10}\,\rm cm^{-3})$, $\gamma_{100} = \gamma/100$, and we have scaled to $n = 4.6$. Note that $n^{CR}(>\gamma) = 10^{-10}\gamma^{-1.6}\,\rm cm^{-3}$ roughly corresponds to a CR energy density in equipartition with a $\sim$ μG B-field. The fact that $(\delta B/B)^2 \ll 1$ self-consistently implies that quasi-linear theory is applicable. If we insert this into equation (1.7), we obtain for the drift speed:

$$v_{\rm D} = v_{\rm A}\left(1 + 0.9\frac{(n_{-3}^{i})^{3/4}T_{4\,\rm keV}^{1/4}10^{n-4.6}}{B_{\mu\rm G}L_{\rm z,100}^{1/2}(n_{-10}^{\rm CR})^{1/2}}\gamma_{100}^{(n-3)/2}\right) \tag{1.10}$$

Several points should be noted. For these parameters, streaming speeds do not significantly exceed the Alfvén speed for the ∼100 GeV cosmic-ray protons which in turn produce the 10 GeV CR electrons which in turn produce ∼GHz radio emission. For Alfvén speeds of $v_{\rm A} \approx 70\,\rm km\,s^{-1}\,B_{\mu\rm G}n_{i,-3}^{-1/2}$, this implies radio halo turnoff times of $t \sim 1.4\,\rm Gyr\,L_{100}B_{\mu\rm G}^{-1}n_{i,-3}^{1/2}$, which may seem too long. However, note that $L_{\rm z}, n^{\rm CR}$ will be time-dependent functions during the streaming process,

so it is necessary to check how streaming evolves in a time-dependent calculation. Our results should be contrasted with those of [36], who describe similar estimates based on [43], but do not give explicit expressions. Unlike them, we find $v_{\rm D} \ll c_{\rm s}$ for plasma parameters corresponding to observed clusters; nothing in the problem singles out the sound speed as a reference speed. Note that all the parameters in equation (1.10) are observationally constrained, so order of magnitude departures are unlikely. Also note that even though $\Gamma_{\rm NL} \propto \beta^{1/2}$, there is no explicit β dependence in $v_{\rm D}$.

Turbulent Damping

Another source of wave damping comes from the highly anisotropic nature of MHD turbulence [42, 118]. We adopt the [50] theory (hereafter 'GS') for strong, incompressible MHD turbulence; an excellent summary can be found in [65]. Turbulence in clusters is generally incompressible since it is significantly subsonic except at the cluster periphery. The strong turbulence regime where GS theory is applicable sets in at wavenumbers $k \lesssim k_o M_{\rm A}^{-2}$ (e.g., see [76]); since $M_{\rm A} \gtrsim 1$ in clusters, the theory is clearly applicable, particularly at the small scales relevant for CR scattering. GS theory has support both from numerical simulations

[29, 69, 28] and solar wind measurements [55, 86, 116, 27]. It is anisotropic, with:

$$v_{\lambda_\perp} \sim v_{\rm A}\left(\frac{\lambda_\perp}{L_{\rm MHD}}\right)^{1/3} \sim (\epsilon\lambda_\perp)^{1/3} \tag{1.11}$$

$$\frac{\Lambda_\parallel(\lambda_\perp)}{\lambda_\perp} \sim \left(\frac{L_{\rm MHD}}{\lambda_\perp}\right)^{1/3} \tag{1.12}$$

where $\lambda_\perp$ is the length scale transverse to the local mean magnetic field, $v_{\lambda_\perp}$ is the rms velocity fluctuation across $\lambda_\perp$, $\Lambda_\parallel(\lambda_\perp)$ is the length scale parallel to the local mean magnetic field across which the velocity fluctuation is $v_{\lambda_\perp}$,$L_{\rm MHD}$ is the length scale at which turbulence is excited with velocity perturbations comparable to the Alfvén speed $v_{\rm A}$ (i.e., with $M_{\rm A} \sim 1$), and $\epsilon \sim v_{\lambda_\perp}^3/\lambda_\perp \sim v_{\rm A}^3/L_{\rm MHD}$ is the (constant) energy cascade rate per unit mass. Note that $L_{\rm MHD}$ is *defined* to be the scale at which $M_{\rm A} = 1$; if turbulence is already sub-Alfvénic at the outer scale, then it should be considered an extrapolation. Equation (1.11) describes a standard Kolmogorov cascade in the transverse direction. Equation (1.12) indicates that an eddy becomes increasingly elongated along the magnetic field, $\Lambda_\parallel \gg \lambda_\perp$ as the cascade proceeds deep into the inertial range $\lambda_\perp \ll L_{\rm MHD}$. It can be derived from the assumption of "critical balance", which states that characteristic linear and non-linear interaction times are approximately equal at all scales (e.g., see [76]). Thus, the cascade proceeds primarily in the transverse direction, and most of the power is concentrated in modes with transverse wave vectors. Intuitively, we can understand this from the fact that in MHD turbulence, non-linear inter-

actions arise from collisions of oppositely directed Alfvén wave packets travelling along field lines. A wave packet is distorted when it follows field lines perturbed by its collision partner; it cascades when the field lines along which it is propagating have spread by a distance comparable to $\lambda_\perp$. Since the magnetic and velocity fluctuations associated with Alfvén waves are transverse to the local mean field, the cascade proceeds primarily in the transverse direction. This anisotropic damping of waves by turbulence has been demonstrated numerically in [9].

Turbulence therefore suppresses the waves responsible for self-confinement of cosmic rays, since they cascade to smaller scales before they have an opportunity to scatter CRs. In particular, the small scale transverse components injected by the cascade mean that the CR no longer experiences a time-steady force in its orbit; instead it sees an oscillating force which leads to inefficient scattering. For these same reasons, MHD turbulence scatters CRs inefficiently [25, 118]. The damping rate of a wave is simply the eddy turnover rate [42]:

$$\Gamma_{\rm turb} \sim \frac{v_{\lambda_\perp}}{\lambda_\perp} \sim \frac{\epsilon^{1/3}}{\lambda_\perp^{2/3}} \tag{1.13}$$

where we use equation (1.11). Growth rates are highest, and damping rates lowest, for the most closely parallel-propagating waves, i.e. those with the largest $\lambda_\perp$. Even if a CR-generated wave starts out as parallel-propagating, the turbulent cascade injects transverse components which subsequently cascade. The amplitude

of magnetic field fluctuations across a scale $\lambda_\perp$ thus define a minimal aspect ratio[5] $(k_\perp/k_\parallel)_{\rm min} \sim \delta B(\lambda_\perp)/B \sim v_{\lambda_\perp}/v_{\rm A} \sim (\lambda_\perp/L_{\rm MHD})^{1/3}$ (using equation (1.11) in the last step). From the resonance condition $k_\parallel^{-1} \sim r_{\rm L}$, the smallest possible perpendicular wavenumber is $k_{\perp,{\rm min}} \sim \epsilon^{1/4}(r_{\rm L}v_{\rm A})^{-3/4}$. Inserting the largest possible perpendicular wavelength $\lambda_\perp \sim k_{\perp,{\rm min}}$ into equation (1.13), the minimal damping rate for a wave with $k_\parallel \sim r_{\rm L}^{-1}$ is [42]:

$$\Gamma_{\rm turb,min} \sim \left(\frac{\epsilon}{r_{\rm L}v_{\rm A}}\right)^{1/2}. \tag{1.14}$$

If in steady state we balance the wave growth rate (equation (1.2)) with this damping rate, we obtain a streaming speed:

$$v_{\rm D} = v_{\rm A}\left(1 + 1.2\frac{B_{\mu{\rm G}}^{1/2} n_{i,-3}^{1/2}}{L_{\rm MHD,100}^{1/2} n_{\rm CR,-10}}\gamma_{100}^{n-3.5} 10^{2(n-4.6)}\right) \tag{1.15}$$

where $L_{\rm MHD,100} = L_{\rm MHD}/100$ kpc. We also obtain $(\delta B/B) \sim 10^{-3}$. At first blush, non-linear Landau damping and turbulent damping both seem to give similarly slow streaming speeds. However, note that $v_{\rm D} - v_{\rm A} \propto (n_{\rm CR}^{-1/2}, n_{\rm CR}^{-1})$ for these two sources of damping respectively. This difference becomes crucial during non-linear evolution, enabling CRs in the turbulent damping case to stream much more effectively.

[5]This should not be confused with the eddy aspect ratio $\Lambda_\parallel(\lambda_\perp)/\lambda_\perp \gg 1$, whereas we have $(\lambda_\parallel/\lambda_\perp)_{\rm min} < 1$. Typical eddies in the MHD cascade vary mostly in the transverse direction, $k_\perp \gg k_\parallel$, whereas we seek waves injected by CRs with the least possible transverse variation, $k_\perp \ll k_\parallel$.

General Remarks on Cosmic-Ray Streaming

We have now derived streaming speeds for two different damping mechanisms, which depend both on CR energy ($v_{\rm D} \propto \gamma^{0.8}, \gamma^{1.1}$ for non-linear Landau damping and turbulent damping respectively) and plasma parameters – most notably the CR number density. The streaming speed is thus a function of both position and time, and is best self-consistently solved in a time-dependent calculation, as we will soon tackle.[6] Before we forge ahead and use these expressions, there are several potential complications worth discussing.

Our streaming speeds for the ICM are characteristically of order the Alfvén speed, although this can vary spatially and temporally as plasma parameters vary, particularly the CR number density. [36] argue against the Alfvén speed as a characteristic CR propagation speed in a high β plasma, arguing that in the limit where the background magnetic field $B \rightarrow 0$, this would imply that $v_{\rm D} \approx v_{\rm A} \rightarrow 0$, rather than $v_{\rm D} \rightarrow c$, as might be expected if there is no magnetic field to couple the CRs to the plasma. Instead, they advocate the sound speed $c_{\rm S}$ as a characteristic streaming speed. We have several remarks. The streaming speeds we have calculated via quasi-linear theory assumes $(\delta B/B) \ll 1$, and we have checked that this condition is self-consistently fulfilled in the ICM (typically, $(\delta B/B) \sim 10^{-4}$), an amplitude similar to that inferred for the coronal gas in our

[6] We have also assume $n(>\gamma)$ to be a fixed power-law, whereas it steepens with time due to energy dependent streaming.

Galaxy. The hypothetical limit $B \to 0$ (which is not realized in the ICM) clearly violates this assumption, and requires a fully non-linear calculation.[7]There, we might expect that instabilities generated by a current of streaming CRs (e.g., [7]) would nonetheless generate a B-field which will confine the CRs. Nothing in our calculations singles out the sound speed as a reference velocity.

The resonance condition, equation (1.1), shows that CRs of larger pitch angle ($\mu \to 0$) interact with waves of progressively shorter wavelength. However, growth rates $\Gamma_{\rm CR} \propto \mu$ (e.g., [60]), while non-linear Landau damping $\Gamma_{\rm NL} \propto 1/\mu$ (equation (1.3)), so there is relatively little energy in such short wavelength waves as $\mu \to 0$. On the face of it, this would imply that it is impossible for particles to scatter across the $\theta = 90^\circ$ point via resonant scattering to reverse direction, the well-known '90° problem' (in fact, the affected region is small; quasi-linear interactions can effectively scatter CRs down to $\mu_{\rm c} \sim 10^{-4}$. The gap is a little larger, $\sim v_i/c \sim 3\times10^{-3}$, in a high-$\beta$ plasma when ion-cyclotron damping is effective [54]). The fact that CRs appear to be efficiently confined and isotropized in our Galaxy implies that Nature has found a way around it. The leading explanation appears to be mirror interactions from MHD waves created by the $\theta \sim 0^\circ$ CRs, which are able to trap the particles and turn them around [43]. These mirror interactions can also be thought of as resonance broadening [1, 120] of the long wavelength waves.

[7]Note that even in linear calculations, the real part of the dispersion relation is significantly modified, with the wave speed itself becoming super-Alfvénic [48, 123, 124].

[43] conduct a detailed boundary layer calculation of the mirror interaction and find that it introduces a minor logarithmic correction (which we have ignored) to the standard calculation. We note that if there were indeed a 90° problem in the ICM, the resulting light-speed streaming speeds would imply flat CRp and CRe profiles, which is inconsistent at least with observations of radio mini-halos such as Perseus. It would also shut off radio halos extremely rapidly, regardless of how the relativistic electrons are produced.

The wave damping rate is the sum of all damping processes, and thus in principle one should always consider the contribution from both turbulent and non-linear Landau damping. In practice, we consider limiting regimes where one process dominates. Their ratio is:

$$\frac{\Gamma_{\rm turb}}{\Gamma_{\rm NL}} \approx 1. \frac{B_{\mu\rm G}^{3/2} n_{i,-3}^{1/4} L_{\rm z,100}^{1/2}}{L_{\rm MHD,100}^{1/2} T_{\rm 4keV}^{1/4} n_{\rm CR,-10}^{1/2}} \gamma_{100}^{n/2-2} \propto \left(\frac{1}{\nabla f}\right)^{1/2}. \tag{1.16}$$

Turbulent damping thus always dominates at late times as the CR profile falls ($n_{\rm CR} \to 0$) and flattens ($L_{\rm z} \to \infty$).

We have only considered CR self-confinement, and ignored other possible mechanisms for scattering CRs. As we have previously discussed, the anisotropic nature nature of Alfvénic MHD turbulence (which is mostly transverse on small scales comparable to the gyro-radius, in contrast to the parallel modes required to scatter CRs) make them inefficient scatterers of CRs [25, 119]. While the distribution of slow magnetosonic waves follows that of Alfvén waves [65], fast mag-

netosonic modes can potentially have an independent non-linear cascade which is isotropic and can efficiently scatter CRs [99, 22]. For now, we eschew this possibility, in favor of the well-established self-confinement picture, which is the generally accepted theory in our Galaxy. One failing of the self-confinement picture in our Galaxy is that both non-linear Landau damping and turbulent damping appear to damp the waves too efficiently at high energies; the increase of streaming speeds with energy appear inconsistent with the low observed CR anistropy for $E > 100$ GeV [42]. [25] has proposed that magnetic mirror interactions in dense molecular clouds could provide this further confinement, though the possibility remains that some aspects of the physics are still not well understood. A conservative reading of these possible complications would take our derived streaming speeds and diffusion coefficients as upper bounds; they could potentially be lower if scattering is more efficient.

1.2.2 Cosmic-Ray Transport

Cosmic-Ray Transport Equation

The cosmic ray transport equation in the limit of large wave-particle scattering is [105]:

$$\begin{aligned}\frac{\partial f_{\rm p}}{\partial t} + (\mathbf{u} + \mathbf{v}_{\rm A}) \cdot \nabla f_{\rm p} = \nabla \cdot (\kappa_{\rm p} \mathbf{n}\mathbf{n} \cdot \nabla f_{\rm p}) \\ + \frac{1}{3} p \frac{\partial f_{\rm p}}{\partial p} \nabla \cdot (\mathbf{u} + \mathbf{v}_{\rm A}) + Q\end{aligned} \tag{1.17}$$

Here, $f_{\rm p}(\mathbf{x}, p, t)$ is the cosmic ray distribution function (isotropic in momentum space), u is the gas velocity, $\mathbf{v}_{\rm A}$ is the Alfvén velocity, $\mathbf{n}$ is a unit vector pointing along the magnetic field, and Q is a cosmic ray source function. Throughout this paper, we shall always use the 3D distribution function $f_{\rm p}$, which does not include the differential volume factor $4\pi p^2$. All momenta p, unless otherwise specified, will always be in units of mc throughout this paper. The actual momentum will be written $\tilde{p}_i = p_i m_i c$, the subscript denoting the particle type. Any distribution functions written as functions of particle energy rather than momentum will be related by

$$\mathrm{d}n_i = 4\pi p^2 f_i(p_i)\mathrm{d}p_i = f_i(E_i)\mathrm{d}E_i \tag{1.18}$$

$$E_i = \sqrt{1 + p_i^2} m_i c^2 \rightarrow \mathrm{d}E_i = \frac{p_i m_i c^2 \mathrm{d}p_i}{\sqrt{1 + p_i^2}}$$

Equation (1.17) is derived from the collisionless Vlasov equation, which expresses conservation of phase space density:

$$\frac{\partial f}{\partial t} + \nabla \cdot (f\mathbf{v}) + \nabla_p \cdot \left(f \frac{\partial \mathbf{p}}{\partial t} \right) = 0 \tag{1.19}$$

but evaluated in the frame of the Alfvén waves (which has velocity $\mathbf{u}+\mathbf{v}_{\rm A}$, the sum of the local gas and Alfvén velocities). The distribution function is then expanded in inverse powers of the CR-wave collision frequency ν, $f = f_0 + f_1 + f_2 + ...$, where $f_r = \mathcal{O}(\nu^{-r})$. Equation (1.17) is obtained after averaging over pitch angle (justified in the limit of frequent scattering), and is accurate to second order, $\mathcal{O}(\nu^{-2})$. The term with κ_p expresses diffusion relative to the wave frame, and is discussed in detail below. For the details of this expansion we refer the reader to [105]. This equation implicitly assumes that $f_0 \gg f_1$, i.e. to leading order strong wave-particle scattering renders the distribution function isotropic in the wave frame. As we have seen, for most plasma parameters $(v_{\rm D} - v_{\rm A})/c \ll 1$, so this assumption is justified.

The physical interpretation of equation (1.17) is easy to understand. The left-hand side of this equation is a total time derivative, including an advection term in the frame of the waves. The first two terms on the right-hand side represent diffusion along magnetic field lines relative to the wave frame and adiabatic losses/gains respectively. As long as we have a functional form for $\kappa_{\rm p}$ and Q, this equation completely describes the evolution of the cosmic ray population.

Note that in the frame of the wave, and considering the isotropic part of the distribution function f_0 (so that there is no diffusion relative to the wave frame, $\kappa_p = 0$), we have:

$$\frac{Df_0}{Dt} = \frac{1}{3}p\frac{\partial f_0}{\partial p}\nabla \cdot (\mathbf{u} + \mathbf{v}_\mathrm{A}) \tag{1.20}$$

i.e. the CRs evolve adiabatically in the wave frame, with $p \propto n_\mathrm{CR}^{1/3}$ [105]. This makes physical sense: there are no electric fields in the frame of the wave, and hence the particles conserve energy; they can only scatter in pitch angle. However, the CRs do *not* evolve adiabatically in the frame of the gas, where there are electric fields associated with the hydromagnetic waves. Thus, there is an irreversible energy transfer from the CRs to the gas, with volumetric heating rate (e.g., [60]):

$$\Gamma_\mathrm{wave} = -\mathbf{v}_\mathrm{A} \cdot \nabla P_c, \tag{1.21}$$

which we shall refer to as the "wave heating rate". This may be thought of as the rate at which work is done on the gas by CR pressure forces, $\mathbf{v_A} \cdot \mathbf{F}$. Importantly, this heating rate is *not* $\Gamma_\mathrm{wave} = -\mathbf{v}_\mathrm{D} \cdot \nabla P_c$, as has sometimes been adopted elsewhere in the literature (e.g., [107]). The latter expression gives rise to unphysically large heating rates when $v_\mathrm{D} \gg v_\mathrm{A}$. Super-Alfvénic streaming arises due to a *reduction* in coupling between CRs and gas; it is unphysical that this would give rise to greater heating. Physically, all momentum and energy transfer between the CRs and gas is mediated by hydromagnetic waves; the rate at which

work is done by any transmitted forces is therefore set by the velocity of the waves $\mathbf{v}_{\rm A}$.

To next order in ν^{-1}, slippage with respect to the wave frame is expressed by the diffusion coefficient κ_p:

$$\kappa(\gamma) = c^2 \Big\langle \frac{1-\mu^2}{\nu(\mu,\gamma)} \Big\rangle \tag{1.22}$$

where the wave-particle collision frequency $\nu(\mu,\gamma)$ is [58]:

$$\nu(\mu,\gamma) = \frac{\pi}{4}\Omega_0 \left(\frac{\delta B}{B}\right)^2 (\mu,\gamma) \tag{1.23}$$

and the average is taken over pitch angle [105]. This expression is obtained from equation (1.4) as shown by [58], and we assume relativistic CRs such that $v \sim c$. From equation (1.22), the more frequently CRs interact with Alfvén waves, the more slowly they diffuse relative to the waves— as one might expect, since scattering isotropizes the CR in the wave frame. Equation (1.23) can be understood from the fact that a single CR-wave encounter in one gyro-period τ leads to a change in pitch angle $\Delta\theta \approx (\delta B/B)$ [60]; thus $N \sim t/\tau$ encounters leads to a net random walk in pitch angle of $(\Delta\theta)^2 \sim N(\delta B/B)^2 \sim t/\tau(\delta B/B)^2$, or a pitch angle diffusion rate of $D_\theta \sim (\Delta\theta)^2/t \sim \Omega_0(\delta B/B)^2$[8]. Equation (1.22) can be evaluated by equating wave growth and damping rates to obtain the amplitude of the waves,

[8]The mean free path of a CR is roughly the distance over which the pitch angle diffuses by order unity (so that the CR reverses direction), $\lambda \sim cD_\theta^{-1} \sim 3\times10^{12}(\delta B/B)^{-2}$ cm, where the pitch angle diffusion coefficient $D_\theta \sim (\delta B/B)^{-2}\Omega_0$. Thus, even small fields of $(\delta B/B) \sim 10^{-3}$ would lead to mean free paths of $\lambda \sim 1$ pc, implying that the diffusive approximation is excellent.

$(\delta B/B)^2$, as for instance in equation (1.9). It can also be intuitively written in terms of streaming speeds. From equation (1.17), we can write the net streaming speed (i.e. the frame in which the mean CR flux vanishes), as [12]:

$$v_{\rm D} = \frac{1}{f_{\rm p}(p)} \left[-\frac{1}{3} v_{\rm A} p \frac{\partial f_{\rm p}}{\partial p} - \kappa \mathbf{n} \cdot \nabla f_{\rm p} \right] \tag{1.24}$$

where $\mathbf{n}$ is a unit vector pointing along the magnetic field, down the CR gradient. The first term effectively corrects for the Compton-Getting effect, i.e. the differential Doppler shifts of particle energies in transforming from the wave to the inertial frame (depending on whether particles are moving parallel or anti-parallel to the wave, when we calculate the particle flux in the inertial frame, we must compare particles of slightly different energy in the wave frame). If we solve this for the diffusion coefficient, we obtain:

$$\kappa(\gamma) = \frac{f_{\rm p}}{\mathbf{n} \cdot \nabla f_{\rm p}} \left[-v_{\rm D} - \frac{1}{3} v_{\rm A} \frac{\partial \log f_{\rm p}}{\partial \log p} \right] \approx L_{\rm z} [v_{\rm D} - \frac{3}{2} v_{\rm A}] \tag{1.25}$$

Here we have set $\partial \log f_{\rm p} / \partial \log p \approx -4.5$; as before, the energy dependent CR scale length is $L_{\rm z}(\gamma) = |f_{\rm p}/(\mathbf{n} \cdot \nabla f_{\rm p})|$. If we insert this into the diffusion term in equation (1.17), we obtain:

$$D(r) \equiv \nabla \cdot (\kappa_{\rm p} \mathbf{n}\mathbf{n} \cdot \nabla f_{\rm p}) \approx \nabla \cdot (f_{\rm p} \mathbf{n} (v_{\rm D} - v_{\rm A})). \tag{1.26}$$

where we evaluate the drift speed relative to the wave frame, $(v_{\rm D} - v_{\rm A})$, from equations (1.10) and (1.15). Note that the gradient of the distribution function

$\nabla f_{\rm p}$ (or equivalently, the scale height $L_{\rm z}$) does not appear in the diffusion term. It only appears if $(v_{\rm D} - v_{\rm A})$, has a functional dependence on $L_{\rm z}$. This is true for non-linear Landau damping, where $(v_{\rm D} - v_{\rm A}) \propto L_z^{-1/2}$ (so that the diffusion term $\propto (\nabla f_{\rm p})^{1/2}$ rather than $(\nabla f_{\rm p})$), but false for turbulent damping, where the diffusion term is therefore *independent* of the magnitude of ∇f.

The latter unusual behavior was first noted by [105] for the case of ambipolar damping, which shares similarities with turbulent damping in this regard (although he dismissed it as unimportant, since the effects of diffusion were small for the applications he considered). From equations (1.22) & (1.23), and equating wave growth and with a generic damping rate $\Gamma_{\rm D}$, the diffusion term can be expressed more transparently as [105]:

$$D(r) = \frac{1}{p^3}\nabla\cdot\left(\frac{\Gamma_{\rm D}B^2\mathbf{n}}{4\pi^3 m_p\Omega_0 v_{\rm A}}\frac{\mathbf{n}\cdot\nabla f_{\rm p}}{|\mathbf{n}\cdot\nabla f_{\rm p}|}\right) \tag{1.27}$$

$$\approx \frac{1}{4\pi^3 p^{7/2} e^{1/2} m_p^{1/2}}\nabla\cdot\left(\frac{B^{3/2}\mathbf{n}}{L_{\rm MHD}^{1/2}}\frac{\mathbf{n}\cdot\nabla f_{\rm p}}{|\mathbf{n}\cdot\nabla f_{\rm p}|}\right) \tag{1.28}$$

where we specialize to the case of turbulent damping in the second equality, and substitute $\Gamma_{\rm turb} \approx v_{\rm A}/(r_{\rm L}L_{\rm MHD})^{1/2}$. Note that, other than the sign of $\mathbf{n}\cdot\nabla f_{\rm p}$, the term within the divergence is independent of $f_{\rm p}$. This has important consequences for us, in that diffusion does not slow down with time as $\nabla f_{\rm p}$ decreases. Instead, it is independent of $f_{\rm p}$ and depends only on plasma properties. If these plasma properties are roughly constant over the streaming timescale, then $\dot{f}_{\rm p}(r,p,t) \approx$

$D(r,p) \approx$ is roughly constant and $t_{\rm stream} \propto f_{\rm p}/\dot{f}_{\rm p} \propto f_{\rm p}$, with decreases with time as $f_{\rm p}$ falls. This acceleration is key in our more detailed calculations which show that large changes in radio halo luminosity are possible despite apparently long initial diffusion times. It is important to stress, however, that while the diffusion time with turbulent damping is not sensitive to the *magnitude* of $\nabla f_{\rm p}$, it is still sensitive to the *sign* of $\nabla f_{\rm p}$. The sign of $\mathbf{n} \cdot \nabla f_{\rm p}$ reflects the fact that CRs can only stream along B-fields, down their gradient[9]; diffusion has no further effect if $\nabla f_{\rm p} = 0$. Failure to carefully treat this can result in spurious numerical instabilities [103], which we discuss in §1.3.1.

1.2.3 Collisional Losses

Cosmic ray protons can also lose energy from direct collisions with gas particles, either through Coulomb interactions, or hadronic interactions (pion production). While these are generally subdominant to losses from wave-particle interactions, we include them for completeness. This transfer of energy from CRs in turn heats the gas.

[9]CRs can only stream up a gradient if the sign of energy transfer is reversed – i.e., the gas gives energy to the CRs, rather than vice-versa, as in Fermi acceleration. In this case, the picture of self-confinement is clearly not applicable.

The energy loss rate of a CR of speed $\beta = v/c$ and kinetic energy E due to Coulomb collisions in ionized gas is: ([68])

$$\left(\frac{\mathrm{d}E}{\mathrm{d}t}\right)_{\mathrm{C}} = -4.96 \times 10^{-19} \mathrm{erg\ s^{-1}} \left(\frac{n_{\mathrm{e}}}{\mathrm{cm^{-3}}}\right) \frac{\beta^2}{\beta^3 + x_{\mathrm{m}}^3}. \tag{1.29}$$

Here $x_{\mathrm{m}} = 0.0286[T/(2 \times 10^6\ \mathrm{K})]^{1/2}$, with T and n_{e} the gas electron temperature and number density. The energy loss rate of a CR due to hadronic collisions is ([68]):

$$-\left(\frac{\mathrm{d}E}{\mathrm{d}t}\right)_{\mathrm{h}} \approx 0.5 n_{\mathrm{N}} \sigma_{\mathrm{pp}} \beta c E\, \theta(E - E_{\mathrm{thr}}) \tag{1.30}$$

where the pp cross section for hadronic interactions is σ_{pp} and the target nucleon density is $n_{\mathrm{N}} = n_{\mathrm{e}}/(1 - 0.5Y)$, Y being the helium mass fraction. The above assumes an inelasticity of $K = 1/2$ for the collision. The Heaviside step function enforces the condition that only cosmic rays with kinetic energy above $E_{\mathrm{thr}} =$ 282 MeV undergo pion production. All of the energy loss in Coulomb collisions goes toward heating the gas, whereas only $\sim 1/6$ of the inelastic energy in hadronic collisions goes toward secondary electrons which heat the gas, the rest escaping as gamma rays and neutrinos.

These loss terms are represented in the CR Vlasov equation as:

$$\left(\frac{\partial f_{\mathrm{p}}}{\partial t}\right)_{\mathrm{C,h}} = -\frac{\partial}{\partial p}(\dot{p}_{\mathrm{C,h}} f_{\mathrm{p}}) \tag{1.31}$$

$$\dot{p}_{\mathrm{C,h}} = \left(\frac{\mathrm{d}E(p)}{\mathrm{d}t}\right)_{\mathrm{C,h}} \left(\frac{\mathrm{d}E(p)}{\mathrm{d}p}\right)^{-1}$$

where $E = (\sqrt{1 + p^2} - 1) m_{\mathrm{p}} c^2$ and the momentum p is in units of $m_{\mathrm{p}} c$.

1.2.4 Turbulent Diffusion

As we have seen, turbulent gas motions can damp MHD waves and enhance CR streaming. However, they can also directly transport CRs advectively. A proper treatment of the interplay between these effects requires 3D MHD simulations. Here, we will simply treat turbulent motions as a diffusive term in the CR transport equation. If $P_{\rm CR}/P_{\rm gas}$ is small and CRs have negligible effect on the dynamics, they simply act as a passive tracer species. Analogously to the mixing of metals by turbulent diffusion [90], we can write:

$$\left(\frac{\partial n_{\rm CR}}{\partial t}\right)_{\rm turb} = -\nabla \cdot \left[\kappa_{\rm turb} n_e \nabla \left(\frac{n_{\rm CR}}{n_e}\right)\right], \tag{1.32}$$

where

$$\kappa_{\rm turb} \approx \frac{v_t L_t}{3} \approx \frac{v_A L_{\rm MHD}}{3} \tag{1.33}$$

i.e., if turbulent mixing is vigorous, the CRs will have uniform relative abundance, $n_{\rm CR} \propto n_e$. This has some support from simulations where CR dynamics are taken into account [102]. There, turbulent convection results in constant CR entropy $P/n_{\rm CR}^{\gamma_{\rm CR}}$ (where $\gamma_{\rm CR} = 4/3$) and $P_{\rm CR}/P_{\rm g}$ =const. This implies $n_{\rm CR} \propto P_{\rm g}^{1/\gamma_{\rm CR}}$. Since stratified gas in a cluster has a polytropic equation of state $P_{\rm g} \propto \rho_g^{\gamma_{\rm pt}}$ where $\gamma_{\rm pt} \approx 1.2 - 1.3$ (e.g., [24]), this implies $n_{\rm CR} \propto (\rho_g)^{\gamma_{\rm pt}/\gamma_{\rm CR}} \propto \rho_g^{0.9-0.98}$, consistent with our assumptions. Alternatively, [36] suggest a target profile set by gas entropy, rather than CR entropy: $n_{\rm CR} \propto P_g^{1/\gamma_g}$, where $\gamma_g = 5/3$. In this

case, all occurrences of $n_e(r)$ in equation (1.32) will be replaced by $\eta(r) = P_g^{1/\gamma_g}$, and $n_{\rm CR} \propto \rho_g^{\gamma_{\rm pt}/\gamma_g} \propto \rho_g^{0.72-0.78}$. Given the many uncertainties in the model, this difference in scalings is of secondary importance.

We also need to take adiabatic heating and cooling into account. The normalization of the distribution function f varies with adiabatic changes as $C \propto n_{\rm CR}^{\alpha/3}$ (e.g., [38]), where $\alpha = 4 - 5$ is the spectral slope of the distribution function. Thus, the overall effect of turbulent diffusion on the distribution function is:

$$\frac{\partial f}{\partial t} = -\nabla \cdot \left[\kappa_{\rm turb} \delta^{\alpha/3} \nabla \left(\frac{f}{\delta^{\alpha/3}} \right) \right], \tag{1.34}$$

and $\delta(r) = P_{\rm g}^{1/\gamma_{\rm CR}} \approx n_e(r)$, or $\delta(r) = \eta(r) = P_g^{1/\gamma_g}$.

These equations show that turbulent diffusion, acting alone, will lead to a centrally peaked CR profile similar to the gas profile. On the other hand, turbulence also damps MHD waves, leading to enhanced outward streaming, which flattens the CR profile. Which effect dominates? While we explore this in detail in our numerical calculations, it is useful to first get an order of magnitude estimate. From equations (1.25) and (1.33), we obtain:

$$\frac{\kappa_{\rm stream}}{\kappa_{\rm turb}} \approx \left(\frac{v_{\rm D}}{v_{\rm A}} - 1 \right) \left(\frac{L_{\rm z}}{L_{\rm MHD}} \right) \propto \frac{1}{L_{\rm MHD}^{3/2}} \tag{1.35}$$

We expect $L_{\rm z}/L_{\rm MHD} \gtrsim 1$, and $(v_{\rm D}/v{\rm A} - 1) \gtrsim 1$ (from equation (1.15)) for turbulent damping; moreover, these factors increase during the streaming processes as $L_{\rm z}$ rises and $n_{\rm CR}$ fall. Thus, $\kappa_{\rm stream} \gtrsim \kappa_{\rm turb}$ in our fiducial model. Moreover,

if the strength of turbulence increases such that $L_{\rm MHD}$ falls, $\kappa_{\rm stream}/\kappa_{\rm turb}$ *rises*. Stronger turbulence has a larger effect on damping of MHD waves than on inward advection of CRs, and the CRs stream outward faster. Thus, in this framework, turbulent diffusion can never establish a centrally peaked profile, regardless of its strength. In practice, coherent bulk motions (triggered by mergers, or perhaps by gas 'sloshing') can potentially bring CRs to the cluster center, and/or produce a magnetic topology which is unfavorable for outward streaming. However, modeling such stochastic events is beyond the scope of this paper.

A few comments about our choice of fiducial parameters for turbulence is in order. It is customary to define $(L_{\rm t}, v_{\rm t})$, where $L_{\rm t}$ is the outer scale, and $v_{\rm t}$ is the velocity at this scale. Instead, we work with $(L_{\rm MHD}, v_{\rm A})$, where $L_{\rm MHD}$ is *defined* to be the scale at which the turbulent velocity is $v_{\rm A}$. In general, $v_t \sim v_{\rm A}(L_{\rm t}/L_{\rm MHD})^{1/3}$, and more vigorous turbulence can be characterized by smaller values of $L_{\rm MHD}$. However, if there is equipartition between $U_{\rm B} = B^2/8\pi$ and $U_t = 1/2\rho v_t^2$, then $v_{\rm t} \sim v_{\rm A}$ and thus $L_{\rm t} \sim L_{\rm MHD}$. Thus, $(L_{\rm MHD}, v_{\rm A})$ are sensible fiducial parameters. Secondly, we have assumed that $L_{\rm MHD}$ (or equivalently, v_t at a fixed scale) is independent of radius. Is this consistent with cosmological simulations, which show that turbulent pressure support becomes increasingly important with radius? A fit to low-redshift clusters gives ([104], see also [6]):

$$\left(\frac{P_{\rm turb}}{P_{\rm therm}}\right) = \alpha_0 \left(\frac{r}{R_{500}}\right)^{n_{\rm nt}} \tag{1.36}$$

where $\alpha_0 \approx 0.18 \pm 0.06$ and $n_{\rm nt} = 0.8 \pm 0.25$. This implies $v_{\rm t} \propto r^{0.4-\alpha_T/2}$, where $T \propto r^{-\alpha_T}$, and $\alpha_{\rm T}$ is generally small (e.g., $\alpha_T \approx x^2/(1+1.5x)$ [67], where $x \equiv r/r_{\rm vir}$, so $\alpha_{\rm T} \approx 0.2$ at $r = 0.5 r_{\rm vir}$). On the other hand, given our assumption that $B \propto \rho^{\alpha_{\rm B}}$ (see §1.3.4), we have $v_{\rm A} \propto r^{(0.5-\alpha_{\rm B})\alpha_\rho}$, where $\rho \propto r^{-\alpha_\rho}$, and $\alpha_\rho \approx 2-3$ over most of the cluster. The radial scalings for $v_{\rm t}$ and $v_{\rm A}$ are thus roughly consistent: for instance, $\alpha_{\rm B} \approx 0.3$ (as assumed for Perseus & Coma) gives $v_{\rm A} \propto r^{0.4-0.6}$. Finally, we note that for our assumed levels of turbulence, heat dissipation is relatively unimportant. The heating time is:

$$t_{\rm heat} \sim \frac{U_{\rm therm}}{\epsilon} \sim t_{\rm turb} \left(\frac{U_{\rm therm}}{U_{\rm turb}} \right) \sim 5\,{\rm Gyr} \frac{f_{\rm t,5} L_{\rm MHD,100}}{v_{\rm A,100}} \tag{1.37}$$

where $f_{t,5} = [(U_{\rm therm}/U_{\rm turb})/5]$, $L_{\rm MHD,100} = (L_{\rm MHD}/100\,{\rm kpc})$, and $v_{\rm A,100} = (v_A/100\,{\rm km\,s^{-1}})$.

1.3 Method

Our main task is to solve the CR transport equation, in the form:

$$\begin{aligned} \frac{\partial f_{\rm p}}{\partial t} + (\mathbf{u} + \mathbf{v}_{\rm A}) \cdot \nabla f_{\rm p} &= \nabla \cdot (\kappa_{\rm p} \mathbf{nn} \cdot \nabla f_{\rm p}) \\ + \frac{1}{3} p \frac{\partial f_{\rm p}}{\partial p} \nabla \cdot (\mathbf{u} + \mathbf{v}_{\rm A}) &+ Q - \frac{\partial}{\partial p} (\dot{p}_{\rm C,h} f_{\rm p}) \\ -\nabla \cdot \left[\kappa_{\rm turb} \delta^{\alpha/3} \nabla \left(\frac{f}{\delta^{\alpha/3}} \right) \right] & \end{aligned} \tag{1.38}$$

where the last two terms are as in equations (1.31) and (1.34) respectively. To do so, we have written a new module in a 1D spherically symmetric version of

ZEUS3D, previously used to solve the CR equations in the fluid approximation [51].

Our goal in this paper is to determine if CR streaming is a plausible means of turning off radio halos in the hadronic scenario. We therefore run numerical simulations where the cluster is assumed to be in strict hydrostatic and thermal equilibrium, and only solve the CR transport equation (ignoring the fluid equations for the gas, equations , by setting all time derivatives to zero) to examine the effects of CR streaming. In the absence of a cooling flow, the only time-dependent terms in the fluid equations for the gas (equations (1.44),(1.45), and (1.46)) relate to the CRs, and have negligible effect. We initialize the CR profile so as to reproduce the observed radio surface brightness profiles in the classical hadronic model, and follow the time evolution of radio emission as the CRs stream out. In this methods section, we discuss numerical regularization of CR streaming (§1.3.1), a test comparison of our CR transport solver in the fluid approximation (§1.3.2), calculating radio and gamma-ray emission (§1.3.3), and our initial conditions (§1.3.4) for a prototypical radio mini-halo (Perseus) and a prototypical giant radio halo (Coma). Results are then presented in the following section, §1.4.

1.3.1 CR streaming: Numerical Stability

Cosmic rays can only stream down their gradient, in a direction:

$$\mathbf{s} = -\mathrm{sgn}(\mathbf{B} \cdot \nabla f_{\mathrm{p}}) \frac{\mathbf{B}}{|\mathbf{B}|}. \tag{1.39}$$

In our 1D simulations, $\mathbf{s} = -\hat{\mathbf{r}}\,\mathrm{sgn}(\mathrm{d}f_{\mathrm{p}}/\mathrm{d}r)$. However, if this is enforced in equation (1.28), it leads to numerical instabilities and unphysical oscillations in the distribution function. The origin of this difficulty is easy to understand [103]; it essentially arises at local extrema. If the simulation at any time produces a local density maximum, diffusion out of the local maximum will cause the density to drop significantly there. If the time step is not properly restricted, this decrease will overshoot, causing the density to drop below neighboring regions, creating a local minimum. The opposite problem will then occur, with inwardly diffusing CRs causing the CR density to increase too much. The result is an unphysical oscillation that eventually spreads out to all space. Because CR streaming results in a flat profile where $(\mathrm{d}f/\mathrm{d}r)$ vanishes everywhere, this problem can become acute as time goes on.

[103] show that for an explicit code (such as ZEUS3D), the restriction on the time-step such that new local extrema are not created is:

$$\Delta t \leq |f''|\Delta x^3/f|v| \tag{1.40}$$

which is much more onerous than the standard Courant condition (we have explicitly verified that simulations which satisfy the Courant condition suffer from spurious oscillations). They suggest regularizing the CR transport equation by replacing the discontinuous $\mathrm{sgn}(f'_{\rm p})$ with the smooth function $\tanh(f'_{\rm p}/\epsilon)$ for some choice of ϵ. As ϵ tends to zero, the tanh function approaches the sign function. This effectively sets ϵ as a minimum scale value for $f'_{\rm p}$: if $f'_{\rm p} \ll \epsilon$, the simulation behaves as if $f'_{\rm p} = 0$, and suppresses CR streaming. Alternatively, it can be viewed as introducing a diffusive term at an extremum, with diffusion coefficient $f_{\rm p}/\epsilon$, similar to the use of explicit viscosity to regularize Euler/Burger's equations. In this case, the maximum time step allowed to suppress the instability is:

$$\Delta t \leq \Delta x^2 \epsilon / 2 f_p |v|. \tag{1.41}$$

For us, the relevant speed v is the streaming speed, calculated via equation (1.24), which we insert into this equation.

We have found that a scale value of:

$$\epsilon = f_p / L\,; \quad L = 3\,\mathrm{Mpc} \tag{1.42}$$

is sufficiently small that decreasing it any further does not significantly change the results. In Fig 1.1, we show a convergence test (showing the radio luminosity of Perseus as a function of time when $L_{\rm MHD} = 100$ **kpc**; see Fig 1.3b) where the

figure converges to the correct solution as ϵ is decreased; a value of ϵ half of our fiducial value ($\epsilon = 10^{-25} f_{\rm p}$) gives identical results.

In practice, although we use a smoothing scale ϵ, we use the time constraint (1.40) rather than (1.41) and we use $v = v_{\rm A}$ rather than $v = v_{\rm s}$. Additionally, to prevent the time step from dropping to zero we impose a minimum time step

$$\Delta t \geq 1 \times 10^{-7} \Delta x^2 \epsilon / 2 f_p |v| \tag{1.43}$$

where the numerical factor out front is arbitrary. We do all of this to regulate the runtime of the simulation - the less stringent time steps will be less accurate but will run quicker, and we can adjust the minimum time step (1.43) to the desired balance of speed and accuracy. As a result, local minima and maxima do develop at some points of our simulations, however this will always happen as the CR profile flattens; as long as the local extrema do not grow unstably the results should be robust.

In addition, we enforce the constraint that $\Delta f_{\rm p} \leq 0.05 f_{\rm p}$ in a single time-step (and similarly for the gas energy and density). Note that while (1.40) is only applied at local extrema, this condition is held everywhere. Eventually, as $f_{\rm p}$ falls, this shrinks the time-step to zero. To avoid this, we define a momentum dependent minimum $f_{\rm p,min}(p) = 10^{-3} f_{\rm p}(r_{\rm max}, p, t_0)$, where $r_{\rm max}$ is the outer boundary of the simulation, and t_0 is the initial time. The distribution function $f_{\rm p}$ is then never

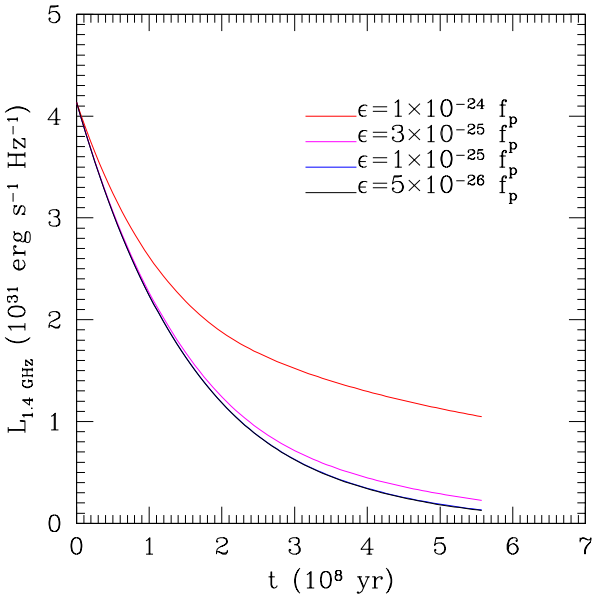

Figure 1.1: Convergence test for the smoothing scale parameter ϵ. We plot the 1.4 GHz radio luminosity of Perseus, which declines with time due to cosmic-ray streaming (here we assume $L_{\rm MHD} = 400$kpc; see §1.4.1 for details). As ϵ is decreased, our calculations converge. Our fiducial value is $\epsilon = 10^{-25} f_{\rm p}$.

allowed to drop below this value. Also, once $f_{\rm p}$ falls below $50 f_{\rm p,min}(p)$ anywhere, all time step restrictions there are ignored, including (1.40).

1.3.2 Test Case: AGN Feedback

To test our solver for the CR transport equation, it is useful to compare against previous results where CRs are treated in the fluid approximation. Specifically, we compare against the results of [51], which simulates the effects of CRs injected by a central AGN on the thermal state of a cool core cluster. It was found that a combination of electron thermal conduction (at some fraction f of the Spitzer

value) and CR mediated wave heating was sufficient to stem a cooling flow. The following governing equations for the two-fluid ICM (gas and cosmic rays) were used:

$$\frac{\partial \rho}{\partial t} + \nabla \cdot (\rho \mathbf{u}) = 0 \tag{1.44}$$

$$\frac{\partial \mathbf{S}}{\partial t} + \nabla \cdot (\mathbf{S}u) = -\nabla P_{\rm g} - \nabla P_{\rm c} - \rho \nabla \Phi \tag{1.45}$$

$$\begin{aligned} \frac{\partial E_{\rm g}}{\partial t} + \nabla \cdot (E_{\rm g}\mathbf{u}) = &-P_{\rm g}\nabla \cdot \mathbf{u} - \nabla \cdot \mathbf{F} \\ &- n_{\rm e}^2 \Lambda(T) + \eta_{\rm c} n_{\rm e} E_{\rm c} - \mathbf{v}_{\rm A} \cdot \nabla P_{\rm c} \end{aligned} \tag{1.46}$$

$$\frac{\partial E_{\rm c}}{\partial t} = (\gamma_{\rm c} - 1)(\mathbf{u} + \mathbf{v}_{\rm A}) \cdot \nabla E_{\rm c} - \nabla \cdot \mathbf{F}_{\rm c} + Q_c. \tag{1.47}$$

$$\mathbf{F}_{\rm c} = \gamma_{\rm c} E_{\rm c}(\mathbf{u} + \mathbf{v}_{\rm A}) - \mathbf{n}\kappa_{\rm c}(\mathbf{n} \cdot \nabla E_{\rm c}), \tag{1.48}$$

where ρ is the gas density, $P_{\rm g}$ is the gas pressure, $E_{\rm g}$ is the gas energy density, $\mathbf{S} = \rho\mathbf{u}$ is the gas momentum vector, E_c is the cosmic ray energy, $P_{\rm c} = (\gamma_{\rm c} - 1)E_{\rm c}$ is the cosmic-ray pressure, $\mathbf{F}$ is the electron conduction heat flux, and Φ is the gravitational potential. The term $\eta_{\rm c} n_{\rm e} E_{\rm c}$, where $\eta_{\rm c} = 2.63 \times 10^{-16}$ cm^3 s^{-1}, takes Coulomb and hadronic heating of the gas by cosmic rays into account. The initial conditions, gravitational potential $\Phi(r)$, and cooling function $\Lambda(T)$ are as spelled out in [51]; please refer to the paper for details. The source function Q represents the injection of CRs by an AGN, triggered by gas cooling:

$$Q_{\rm c} = -\frac{\nu \epsilon \dot{M}_{\rm in} c^2}{4\pi r_0^3} \left(\frac{r}{r_0}\right)^{-3-\nu} [1 - e^{-(r/r_0)^2}] \tag{1.49}$$

Here, $\epsilon = 3 \times 10^{-3}$ is an efficiency parameter, $\nu = 0.3$, and $r_0 = 20$ kpc is a scale distance.

The code of [51] uses the CR energy density E_c as the fundamental dynamic variable for CRs. It is:

$$E_{\rm c} = 4\pi \int_0^\infty p^2 T_{\rm p}(p_{\rm p}) f_{\rm p}(p_{\rm p}) {\rm d}p \tag{1.50}$$

where

$$T_{\rm p}(p) = \left[\sqrt{1+p^2} - 1\right] mc^2. \tag{1.51}$$

is the kinetic energy of a CR proton of momentum $p_{\rm p}$. By using E_c as the main CR dynamic variable, all momentum dependence has been integrated out. By contrast, we wish to retain momentum dependence, and instead use $f(r, p, t)$ as our fundamental variable. We therefore continue to solve equations (1.44)−(1.46), but replace equations (1.47) & (1.48) with the equation for the distribution function, equation (1.38), and solve for E_c as required in equations (1.45), (1.46) via equations (1.50) and (1.51). In calculating the momentum-dependent source function Q for use in equation (1.38), we suppose that the injected spectra has the form:

$$f_{\rm p}(E) = \frac{A_{\rm cr}\theta(E - E_{\rm l})}{(E/E_*)^{\tilde{\alpha}} + (E/E_*)^{(\tilde{\alpha}-2)/2}} \tag{1.52}$$

which assumes a steady state spectrum at low (high) energies due to Coulomb (hadronic) losses, and smoothly connects these regimes (see [51] for details). Here,

$E_* = 706$ MeV is a cross-over energy separating the low- and high-energy regimes, while the assumed spectral index is $\tilde{\alpha} = 2.5$, and cutoff energy is $E_\mathrm{l} = 10$ MeV. We create a source function with the same momentum dependence as equation (1.52), and then normalize it to the total CR injection rate given by equation (1.49):

$$Q_\mathrm{c} = 4\pi \int_0^\infty p^2 T_\mathrm{p} Q \, \mathrm{d}p. \tag{1.53}$$

To maintain consistency with [51], we use the same momentum-independent diffusion coefficient used there.

The simulation grid has two ghost zones at each end in the radial direction, and one ghost zone at each end in the momentum direction. The density and temperature of the ICM are linearly extrapolated into the spatial ghost zones. For the CR spectrum, constant boundary conditions are enforced in the radial direction, i.e. $f_\mathrm{p}(p)$ at the spatial ghost zones are set equal to $f_\mathrm{p}(p)$ in the adjacent active zones. In the momentum direction we required that $\mathrm{d}\log f_\mathrm{p}/\mathrm{d}\log p$ be constant across the boundary. As for time step constraints, for this test case we do not allow ρ_g or E_g to change by more than 25% in any time step. We also enforce the Courant condition for all cells, $\Delta t < \Delta x^2/2\kappa_\mathrm{p}$.

We find that our full model reproduces the results of [51] extremely well. A example is shown in Fig. 1.2, where we show the temperature as a function of time for several select radii. The cluster is initialized to be isothermal; after an initial

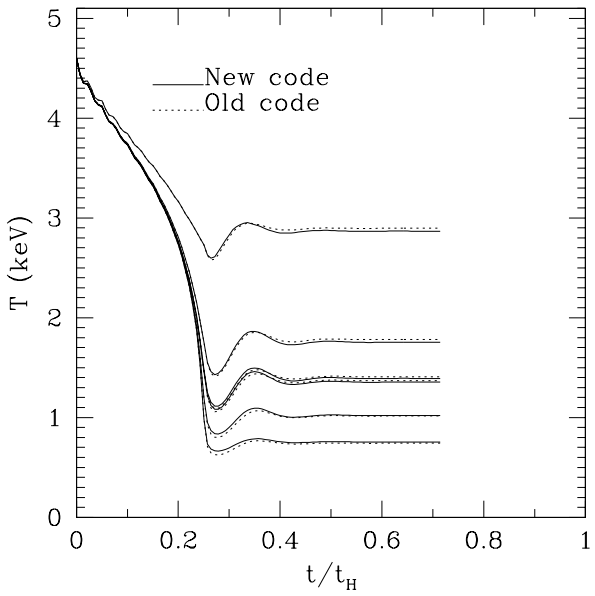

Figure 1.2: Temperature versus simulation time at some select radii for the new code, where we solve the CR transport equation (1.38). The results of the old code, which treats CRs in the fluid limit (equations (1.47), (1.48)), are displayed in the dotted lines.

transient, it is thermally stabilized against a cooling catastrophe by a combination of CR heating and electron thermal conduction. The dotted lines show the results from the code of [51], which integrates the fluid equations, while the solid lines indicate the results of the new code, which computes the distribution function. Indeed, even when we include the full momentum dependence of the diffusion coefficient, the results barely change (for this particular example, we have assumed non-linear Landau damping). This is because most of the energy density of CRs is dominated by low energy CRs ($\sim 1\,\mathrm{GeV}$) for which the diffusion time is negligibly long. As we shall soon see, diffusion cannot be neglected for the high-energy CRs which are responsible for observed radio emission.

1.3.3 Computing Emissivities

Our fundamental simulation variable is the CRp distribution function, $f_{\rm p}(r,p,t)$. Here, we describe how radio and gamma-ray emission can be inferred from $f_{\rm p}(p)$ (hereafter, we suppress r,t) in the hadronic model, given an assumed gas density and magnetic field.

How is radio emission produced? CR protons undergo hadronic interactions to produce pions, which in turn decay to produce relativistic electrons (CRp + nucleon $\rightarrow \pi^{\pm},\pi^{0}$; $\pi^{\pm} \rightarrow \mu^{\pm} + \nu_{\mu}/\bar{\nu}_{\mu} \rightarrow e^{\pm} + \nu_{e}/\bar{\nu}_{e} + \nu_{\mu} + \bar{\nu}_{\mu}$; $\pi^{0} \rightarrow 2\gamma$). The high energy electrons which produce observable synchrotron emission have short cooling lifetimes and we therefore assume a steady-state between injection and cooling. A CRp distribution $f_{\rm p}(p)$ gives rise to a pion source function due to the hadronic pp interaction [84]:

$$\begin{aligned} s_{\pi^{\pm}}(p_{\pi}) = \frac{2}{3}\int_{-\infty}^{\infty} {\rm d}p_{\rm p} f_{\rm p}(p_{\rm p}) c n_{\rm N} \xi(p_{\rm p}) \sigma_{\rm pp}^{\pi} \\ \times \delta\left(p_{\pi} - \frac{m_{\rm p}}{4m_{\pi}} p_{\rm p}\right) \theta(p_{\rm p} - 0.78) \end{aligned} \tag{1.54}$$

where $\sigma_{\rm pp}^{\pi} = 32(0.96 + e^{4.4-2.4\alpha_{\rm p}})$ mbarn [10]. The delta function enforces the mean pion momentum $\langle \tilde{p}_{\pi} \rangle = \tilde{p}_{\rm p}/4$ and the Heaviside step function θ incorporates the threshold proton momentum for the pion production to occur. Approximating

[10] We follow [83] in absorbing the weak energy dependencies of the pion multiplicity and the inelastic cross-section in this semi-analytical parametrization of the cross-section, where $\alpha_{\rm p}$ is the average CR spectral index.

the pion multiplicity ξ as 2, this gives:

$$\begin{aligned} s_{\pi^\pm}(p_\pi) =& \frac{16}{3}\frac{m_\pi}{m_\mathrm{p}} c n_\mathrm{N} \sigma^\pi_\mathrm{pp} 4\pi \left(\frac{4m_\pi}{m_\mathrm{p}} p_\pi\right)^2 \\ & \times f_\mathrm{p}\left(\frac{4m_\pi}{m_\mathrm{p}} p_\pi\right) \theta\left(\frac{4m_\pi}{m_\mathrm{p}} p_\pi - 0.78\right) \end{aligned} \tag{1.55}$$

Under this approximation, the neutral pion source function s_{π^0} is the same.

The charged pion population will undergo pion decay, producing electrons (and other particles). This electron production is described with the electron source function:

$$s_\mathrm{e}(p_\mathrm{e}) = s_{\pi^\pm}(p_\pi(p_\mathrm{e}))\frac{\mathrm{d}p_\pi}{\mathrm{d}p_\mathrm{e}} \tag{1.56}$$

$$\begin{aligned} \Rightarrow s_\mathrm{e}(p_\mathrm{e}) =& \frac{64}{3}\frac{m_\mathrm{e}}{m_\mathrm{p}} c n_\mathrm{N} \sigma^\pi_\mathrm{pp} 4\pi \left(\frac{16m_\mathrm{e}}{m_\mathrm{p}} p_\mathrm{e}\right)^2 \\ & \times f_\mathrm{p}\left(\frac{16m_\mathrm{e}}{m_\mathrm{p}} p_\pi\right) \theta\left(\frac{16m_\mathrm{e}}{m_\mathrm{p}} p_\mathrm{e} - 0.78\right) \end{aligned} \tag{1.57}$$

In the second equation we have used $\tilde{p}_\pi = 4\tilde{p}_e$. If we assume an equilibrium between this source and any losses, i.e. a steady state solution, the electron spectrum is then determined from

$$f_\mathrm{e}(p_\mathrm{e}) = \frac{1}{|\dot{p}_\mathrm{e}|}\int_{p_\mathrm{e}}^\infty \mathrm{d}p'_\mathrm{e} s_\mathrm{e}(p'_\mathrm{e}) \tag{1.58}$$

where the losses $\dot{p}_\mathrm{e}$ are

$$\dot{p}_\mathrm{e}(p_\mathrm{e}) = \frac{\dot{E}_\mathrm{e}}{m_\mathrm{e}c^2} = \frac{4}{3}\frac{\sigma_\mathrm{T} c p_\mathrm{e}^2}{m_\mathrm{e}c^2}(\varepsilon_\mathrm{B} + \varepsilon_\mathrm{cmb}) \tag{1.59}$$

from synchrotron radiation and inverse Compton (IC) scattering. Here, σ_T is the Thompson scattering cross section, and $\varepsilon_\mathrm{B}, \varepsilon_\mathrm{cmb}$ are the energy density of the B-field and cosmic microwave background.

From the electron distribution function we can determine the resulting synchrotron emissivity [96]:

$$j_\nu(r) = 0.333\frac{\sqrt{3}}{2\pi}\frac{e^3 B(r)}{m_\mathrm{e}c^2}\int_1^\infty \mathrm{d}\gamma_\mathrm{e} f_\mathrm{e}(r,\gamma_\mathrm{e}) F\left(\frac{\nu}{\nu_\mathrm{c}}\right) \tag{1.60}$$

In the above, $\nu_\mathrm{c} = 3eB\gamma_\mathrm{e}^2/4\pi m_\mathrm{e}c$ and the function F is an integral of a modified Bessel function, $F(x) = x\int_x^\infty K_{5/3}(x')\mathrm{d}x'$. The numerical factor in front comes from averaging the CRe population over pitch angle, assuming isotropy. The observed surface brightness is:

$$S_\nu(r_\perp) = \int_{-\infty}^\infty j_{\nu'}(r(l))\mathrm{d}l = \frac{2}{(1+z)^3}\int_{r_\perp}^\infty j_{\nu'}(r)\frac{r\,\mathrm{d}r}{\sqrt{r^2 - r_\perp^2}} \tag{1.61}$$

where $\nu' = \nu(1+z)$. The luminosity is:

$$L_\nu = \int \mathrm{d}^3\mathbf{r} j_\nu(r) \tag{1.62}$$

We also make predictions for gamma-ray emission. We only consider gamma-ray emission from neutral pion decay $\pi^0 \rightarrow 2\gamma$ and ignore the subdominant contribution from inverse Compton scattering. The analysis is much the same as above. Following [68], we derive a photon source function from the pions:

$$s_\gamma(E_\gamma) = 2\int_{E_\gamma + \frac{(m_\pi c^2)^2}{E_\gamma}}^\infty \frac{\mathrm{d}E_\pi s_{\pi^0}(E_\pi)}{\sqrt{E_\pi^2 - m_\pi^2 c^4}} \tag{1.63}$$

where the neutral pion source function $s_{\pi^0}(E_\pi)$ is assumed to be the same as for charged pions, equation (1.55). From this source function, we determine a number

production rate per unit volume λ_γ:

$$\lambda_\gamma(> E_\gamma) = \int_{E'_\gamma}^{\infty} \mathrm{d}E'_\gamma s_\gamma(E'_\gamma) \tag{1.64}$$

and the flux detected at Earth above an energy E_γ:

$$F_\gamma(> E_\gamma) = \frac{1}{4\pi d_{\mathrm{L}}^2} \int \mathrm{d}^3\mathbf{r} \lambda_\gamma(> E_\gamma) \tag{1.65}$$

Given the strong momentum dependence of CR streaming, it is worth clarifying which range of CRp momenta are most observationally relevant. For radio emission, the characteristic synchrotron frequency is $\sim 3\gamma^2\nu_c$, where ν_c is the non-relativistic synchrotron frequency. For a given observational frequency ν_s, the greatest contribution comes from electrons with:

$$p_{\mathrm{emit}} \approx \gamma_{\mathrm{emit}} \approx 4 \times 10^3 \left(\frac{\nu_s}{1\,\mathrm{GHz}}\right)^{1/2} \left(\frac{B}{3\,\mu\mathrm{G}}\right)^{-1/2} \tag{1.66}$$

Thus, ~ 10 GeV electrons are responsible for $\sim$GHz emission in μG fields. Typically, $\tilde{p}_e \sim (1/16)\tilde{p}_{\mathrm{p}}$, where $\tilde{p}_e$ is the momentum of a secondary CRe produced hadronically. The reduction in energy by a factor of ~ 16 comes from the fact that the limiting inelasticity is $\sim 1/2$ [68], the pion multiplicity is a factor of ~ 2 due to 2 pion jets leaving the interaction site [75], and $\langle E \rangle = (1/4)\langle E_{\pi^\pm} \rangle$ in the reaction $\pi^\pm \rightarrow e^\pm + 3\nu$. Thus for $\sim$ GHz emission, ~ 100 GeV protons are most relevant, while for LOFAR observations at ~ 100 MHz, ~ 10 GeV protons are most relevant. For γ-ray emission, $E_\gamma \approx (1/8)E_p$ (all the factors are as before,

except $E_\gamma = 1/2E_{\pi^0}$). Thus, Fermi, which is most sensitive in the $E_\gamma \approx 0.1 - 3$ GeV range (rather than $0.1-300$ GeV, due to the pion bump), probes $E_\mathrm{p} \sim 1-30$ GeV, while imaging air Cerenkov telescopes such as MAGIC, HESS and VERITAS are most sensitive in the $E_\gamma \sim 0.3 - 1$ TeV range (rather than 0.3-10 TeV, due to the steep CRp spectrum), probes $E_\mathrm{p} \sim 3 - 10$ TeV.

1.3.4 Initial and Boundary Conditions

We choose to simulate a prototypical radio mini-halo, Perseus, and a prototypical giant radio halo, Coma. We choose initial conditions which reproduce current observations of their radio surface brightness, and then watch how this evolves under the influence of streaming. For the Perseus cluster, we adopt empirical fits to the cluster temperature and electron density profiles ([85]) based on observed X-ray emission ([30]):

$$\begin{aligned}\frac{n_\mathrm{e}}{10^{-3}\mathrm{cm}^{-3}} = 46 &\left[1 + \left(\frac{r}{57\ \mathrm{kpc}}\right)^2\right]^{-1.8} \\ &+ 4.79\left[1 + \left(\frac{r}{200\ \mathrm{kpc}}\right)^2\right]^{-0.87}\end{aligned} \tag{1.67}$$

$$T = 7\ \mathrm{keV}\frac{1 + (r/71\ \mathrm{kpc})^3}{2.3 + (r/71\ \mathrm{kpc})^3}\left[1 + \left(\frac{r}{380\ \mathrm{kpc}}\right)^2\right]^{-0.32} \tag{1.68}$$

From these we determine an internal energy distribution (via the ideal gas law) and a gravitational potential (via hydrostatic equilibrium). Similarly, for Coma

the fits are ([85], based on [17]):

$$\frac{n_{\rm e}}{10^{-3}{\rm cm}^{-3}} = 3.4\left[1+\left(\frac{r}{294\ {\rm kpc}}\right)^2\right]^{-1.125} \tag{1.69}$$

$$T = 8.25\ {\rm keV}\left[1+\left(\frac{r}{460\ {\rm kpc}}\right)^2\right]^{-0.32} \tag{1.70}$$

The radio surface brightness profiles at 1.4 GHz are fit by a β profile:

$$S(r) = S_0[1+(r/r_{\rm c})^2]^{-3\beta+0.5} \tag{1.71}$$

which is reproduced by an initial emissivity of

$$j_\nu(r) = j_{\nu,0}[1+(r/r_{\rm c})^2]^{-3\beta} \tag{1.72}$$

$$j_{\nu,0} = \frac{S_0}{2\pi r_c}(6\beta-1)\mathcal{B}\left(\frac{1}{2},3\beta\right)$$

where $\mathcal{B}$ is the beta function. For Perseus, $\beta = 0.55$, $r_c = 30$ kpc, and $S_0 = 2.3\times10^{-1}$ Jy arcmin^{-2} [79], while for Coma $\beta = 0.78$, $r_{\rm c} = 450$ kpc, and $S_0 = 1.1\times10^{-3}$ Jy arcmin^{-2} [34].

We assume that the magnetic field scales with gas density:

$$B = B_0\left(\frac{n_{\rm e}(r)}{n_e(0)}\right)^{\alpha_B} \tag{1.73}$$

Such a scaling is motivated by simulations [35] and Faraday rotation measurements [14, 57]; for instance, rotation measurements for Coma are well fit by $\alpha_{\rm B}\approx 0.3-0.7$ [14]. In the future it would be interesting to explore other scalings, if for instance this relationship also has temperature dependence [62]. We find that radio surface

brightness profiles can be well fit by $\alpha_{\rm B} = 0.3$ for both clusters, but for Perseus $B_0 = 10\,\mu$G, while for Coma $B_0 = 5\,\mu$G. We choose a cosmic ray distribution function motivated by cosmological hydrodynamic simulations of galaxy clusters where cosmic rays are accelerated via diffusive shock acceleration [85]:

$$f_{\rm p}(r, p_{\rm p}) = C(r) \sum_i \Delta_i p_{\rm p}^{-\alpha_i} \tag{1.74}$$

$$\mathbf{\Delta} = (0.767, 0.143, 0.0975) \qquad \alpha = (2.55, 2.3, 2.15). \tag{1.75}$$

and the normalization

$$C(r) = \frac{(C_{\rm vir} - C_{\rm center})}{1 + \left(\frac{r}{r_{\rm trans}}\right)^{-\beta_{\rm C}}} + C_{\rm center}. \tag{1.76}$$

Note that these simulations do not take into account the effects of cosmic ray streaming. The parameters $C_{\rm vir}, C_{\rm center}, r_{\rm trans}$ are then chosen such that the model radio brightness profile agrees with fits to observations (equation (1.3.4)). For Perseus, if we define $C(r) = \tilde{C}(r) n_{\rm e}(r)$, then $\tilde{C}_{\rm center} = 8.3 \times 10^{-8}, \tilde{C}_{\rm vir} = 7.2 \times 10^{-8}$, $r_{\rm trans} = 36$ kpc, $\beta_{\rm C} = 1.0$. For Coma, $C_{\rm center} = 6 \times 10^{-11}\,{\rm cm}^{-3}$, $C_{\rm vir} = 5.2 \times 10^{-11}\,{\rm cm}^{-3}$, $r_{\rm trans} = 55$ kpc, $\beta_{\rm C} = 1.09$. The initial radio surface brightness profiles derived from these parameters are shown in Fig 1.3a and 1.5a.

When we solve equation (1.38), the simulation grid has two ghost zones at each end in the radial direction, and two ghost zones at each end in the momentum direction. To set values in the ghost zones, we use $\mathrm{d}\log f_{\rm p}/\mathrm{d}\log p$ =const in the momentum direction at both the inner and outer boundary, i.e. a power law

extrapolation. In the spatial direction, we use $\mathrm{d}\log f_\mathrm{p}/\mathrm{d}\log r$ =const at the inner boundary. The outer boundary requires a little more care, since it can fall to extremely low values which result in round-off error; also, if the CR gradient goes to zero at the outer simulation boundary, this artificially suppresses CR streaming. For Perseus, we use $\mathrm{d}\log f_\mathrm{p}/\mathrm{d}\log r$ =const at the outer boundary, but subject to the condition that $f_\mathrm{min} \leq f_{i_\mathrm{max}+1} \leq X f_{i_\mathrm{max}}$, $f_\mathrm{min} \leq f_{i_\mathrm{max}+2} \leq X f_{i_\mathrm{max}+1}$, where i_max is the index of the last active zone, $f_\mathrm{min}(p) = 10^{-3} f_\mathrm{p}(r_\mathrm{max}, p, t_0)$, and $X = 0.98$. For Coma, where the initial profile is already extremely flat, we simply adopt $f_{i_\mathrm{max}+1} = X f_{i_\mathrm{max}}$, $f_{i_\mathrm{max}+2} = X f_{i_\mathrm{max}+1}$. To conserve CRs during the process of turbulent advection, we also enforce the CR turbulent diffusion flux, defined as $\mathbf{F}_\mathrm{turb} = \kappa_\mathrm{turb} \delta^{\alpha/3} \nabla(f_p \delta^{-\alpha/3})$ (see equation (1.34)), to be zero at both spatial boundaries.

For both Perseus and Coma, we use 1.4 GHz data. Note that for Coma, which is the most well-studied giant radio halo, recent 1.4 GHz and 352 MHz data cannot be reconciled by the classical hadronic model with a power-law spectrum [19], though this conclusion is subject to systematic uncertainties in the zero-point of 1.4 GHz data [121]. We shall also see that energy dependence in the streaming speed alters the CR distribution function, so that it is no longer a power-law in momentum, potentially solving this problem.

1.4 Results

We now show results for a canonical radio mini-halo in a cool core cluster (Perseus), and giant radio halo in a non-cool core cluster (Coma), starting from the initial conditions given in §1.3.4. We use Perseus to illustrate most of the relevant physics. Unless otherwise noted, all calculations assume $L_{\rm MHD} = 100$kpc, where $L_{\rm MHD}$ is the lengthscale at which $v_{\rm A} = v_{\rm turb}$ (note from $\epsilon = v_{\rm A}^3/L_{\rm MHD}$ that smaller values of $L_{\rm MHD}$ correspond to more vigorous turbulence).

1.4.1 Perseus Cluster

The initial conditions for Perseus correspond to a CR profile where the ratio of CR energy to the thermal gas energy is almost constant throughout the cluster, decreasing slightly in the outskirts. In Fig 1.3a we compare radio emission from our initial conditions to surface brightness observations at 1.4 GHz from [79]. Note that the observations only span a limited radial range (which produces $\sim 1/2$ of the total radio luminosity in our model). The normalization of the profile falls substantially in several hundred Myr, while its shape does not evolve significantly[11]. Fig 1.3b shows the evolution of the 1.4 GHz radio luminosity with time, and how it depends on the strength and nature of loss processes. The fall in

[11] This is mostly due to projection effects; note that the CR radial profile *does* evolve significantly; see Fig. 1.3e.

luminosity is exponential, on a characteristic $\sim 10^8$ yr timescale. For our fiducial $L_{\rm MHD} = 100$ kpc simulation, $L_{1.4\rm GHz}$ falls by an order of magnitude in several hundred Myr; the decrease is faster for smaller values of $L_{\rm MHD}$, which corresponds to strong damping. If only non-linear Landau damping operates, the decline in luminosity is very slow, and insufficient to turn off radio halos. We also show how $L_{1.4\rm GHz}$ evolves if we ignore diffusion (i.e., the no damping limit) or adiabatic losses in equation (1.38).

The streaming speeds relative to the wave frame for 100 GeV CRps at a radius of 100 kpc are shown in figure 1.3c, for different values of $L_{\rm MHD}$ and if only non-linear Landau damping dominates. We see that even if the streaming speeds start out slow, they can quickly become super-Alfvénic as the CR density drops. This non-linear behavior, which is due to the unusual $\kappa \propto 1/\nabla f$ scaling of the diffusion coefficient for turbulent damping, allows very fast streaming. It is not seen if only non-linear Landau damping operates; in that case, $v_{\rm D} \sim \mathcal{O}(v_{\rm A})$ at all times. Note from equation (1.7) that $v_{\rm D} - v_{\rm A} \sim (\lambda/3L_{\rm z})c$. Thus, as $v_{\rm D} \to c$, $\lambda \to L_z$, and our equations break down, as the CRs can no longer be described by a distribution function. Instead, a fully kinetic approach is needed. This limitation is relatively unimportant since by this stage CRs are no longer self-confined but stream freely along field lines; thus, turn-off is extremely rapid.

The individual contributions to $\dot{f}_{\rm p}$ at 100 GeV are shown in Figure 1.3d in the $L_{\rm MHD} = 100$ kpc case. The values are taken at a fixed radius of 100 kpc, and displayed as a function of time. Interestingly, no one process dominates (and we have verified that adiabatic and diffusive losses acting in tandem are much more effective than either process alone). Initially, adiabatic losses dominate, although they decrease continuously with time. This is to be expected, since the adiabatic loss term is proportional to $f_{\rm p}$, and decreases as $f_{\rm p}$ falls. On the other hand, the diffusion loss term from turbulent damping is independent of $f_{\rm p}$ (equation (1.28)), and thus independent of time as long as there is a spatial gradient. At $t \sim 190$ Myr, the profile at $r \sim 100$ kpc flattens (see Fig. 1.3e), and all terms plummet, although the adiabatic loss term falls most drastically. In §1.5, we explore the nature of this change when the profile flattens: inside the flat core, $\dot{f}_{\rm p}$ changes since it is determined solely by the flux at the outer boundary of the core. From this plot, we can see why adiabatic and diffusive losses in tandem are much more efficient that either alone: adiabatic losses are much more effective in the early stages when the profile is centrally peaked, while diffusive losses are more effective once the profile flattens. We also see that inward turbulent advection is non-negligible but subdominant. It also changes once the region becomes incorporated inside the flat core (since once again only the flux through the core boundary matters at that point).

Fig 1.3e shows $4\pi p^3 f_{\rm p}$ (i.e., CR density) for 100 GeV CRs. As previously discussed, the CR density profile develops a flat core, which expands in size at roughly the streaming speed. Meanwhile, the normalization of the CR profile falls continuously, even for the flat portion. The end result is a profile in which the CR profile has completely flattened and fallen by several orders of magnitude by the end of the simulation.

Finally, the expected γ-ray flux as calculated from equation (1.65) is shown in Fig 1.3f. Observed upper limits are also shown; note that our initial conditions are consistent with these upper limits. Due to the finite momentum grid $p_{\rm p} \leq 5000$, our calculations are only accurate in the range $E_\gamma \lesssim 200$ GeV, although the high energy CRs stream so quickly that the CR transport equation quickly breaks down, in any case. The gamma-ray fluxes decline extremely rapidly with time, with the decline being much sharper at higher energies, due to the fact that higher energy CRs stream faster. The upshot is that at the $E_\gamma \sim 0.3-1$ TeV ($E_{\rm CR} \sim 3-10$ TeV) energies probed by imaging air Cherenkov telescopes (MAGIC, HESS, VERITAS), the decline in gamma-ray luminosity is very rapid. Any detection of gamma-ray emission at these energies, where a source is not immediately apparent (suggesting that it is long-lived), would strongly disfavor the model of CR streaming presented here. However, the $E_\gamma \sim 0.1-3$ GeV ($E_{\rm CR} \sim 1-30$ GeV) energies probed by Fermi correspond to CRs which stream and turn off gamma-ray emission more

slowly. The latter is thus a more robust measure of the cluster's CR injection history. Note that since $\langle E_\gamma \rangle \sim 1/8 \langle E_{\rm CR} \rangle$, gamma-ray emission at $E_\gamma \sim 10$ GeV corresponds to the $E_{\rm CR} \sim 100$ GeV CRs relevant for ∼GHz radio emission, and declines by a similar amount.

By the same token, the energy dependence of CR streaming implies that radio luminosity turns off more slowly at lower frequencies. We show this in Fig 1.7. We can also see this in figure 1.4 which plots the distribution function versus momentum. The higher energy CRps drop in density much faster than lower energy CRps. The corresponding high energy synchrotron emission then also drops faster. This behavior could explain radio halos such as Abell 521, which is detected at 240, 325 and 610 MHz, but not at 1.4 GHz, implying a cutoff or strong spectral curvature at high frequencies [21]. We therefore predict that at the low frequencies probed by LOFAR, radio halos should be significantly more abundant.

1.4.2 Coma Cluster

We now turn to Coma, a prototypical giant radio halo. We focus on the differences with our previous example, Perseus. Due to the flat and extended observed surface brightness profile, which extends out to 1 Mpc (Fig 1.5a, observations from [34]), the inferred CRp distribution is much flatter. Indeed, for the B-field

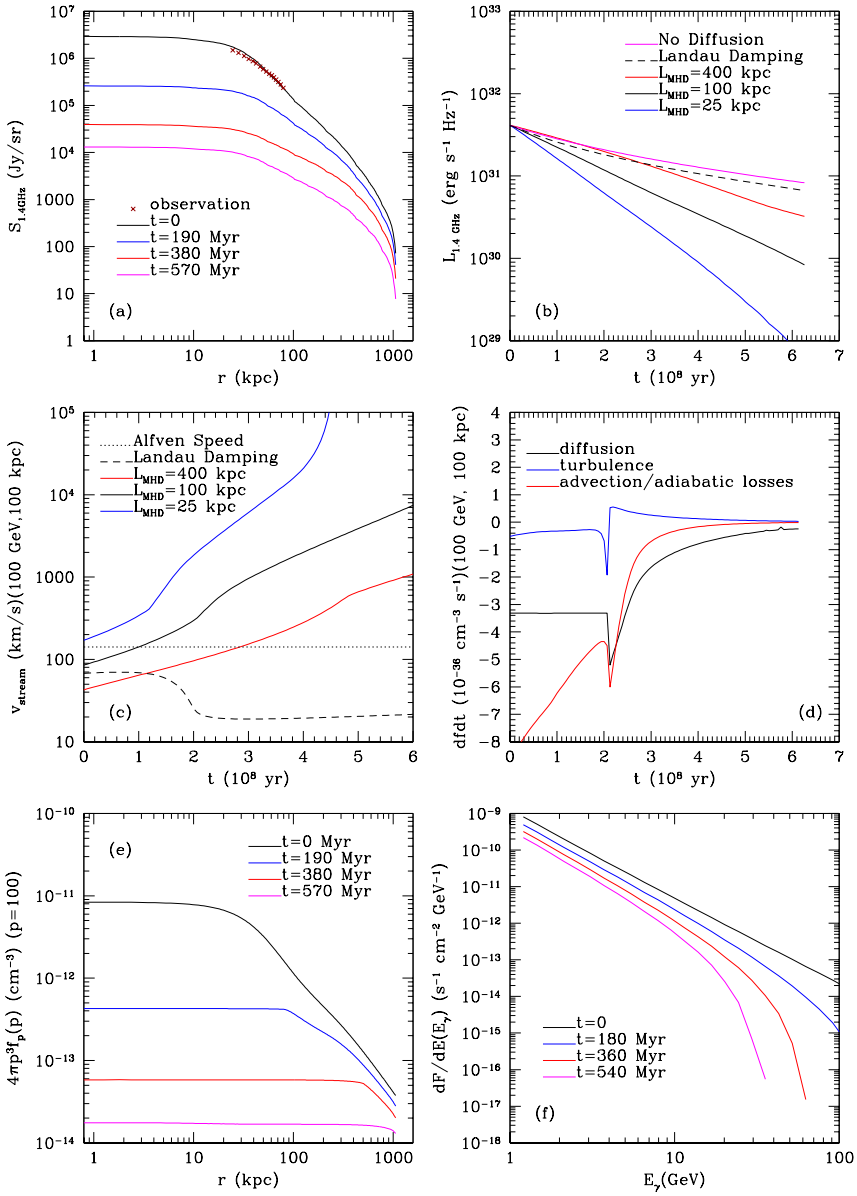

Figure 1.3: Simulation results for the Perseus cluster. **(a)** Radio surface brightness of Perseus for $L_{\rm MHD} = 100$ kpc. Observations from [79]. **(b)** The time evolution of the Perseus cluster's radio luminosity for different levels of damping. The solid lines show MHD turbulence damping at various strengths. The dashed line shows non-linear Landau damping. **(c)** Cosmic ray streaming speeds of 100 GeV CRs at a fixed radius of 100 kpc. **(d)** Different contributions to $\dot{f}_{\rm p}$ for the $L_{\rm MHD} = 100$ kpc Perseus simulation. **(e)** Radial distribution of 100 GeV protons for $L_{\rm MHD} = 100$ kpc. **(f)** Predicted gamma-ray fluxes. Upper limits from observations are at higher energies than those plotted here.

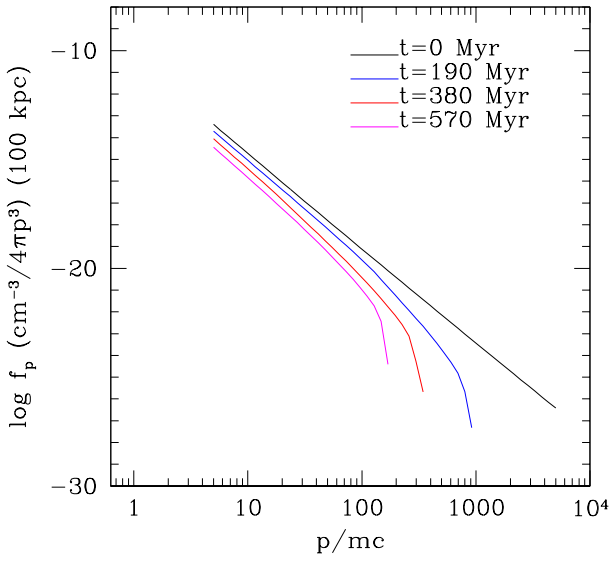

Figure 1.4: CR distribution function versus momentum at a fixed radius of 100 kpc. The dropoff time scales with energy, leading to the spectral steepening discussed above.

we have assumed, $B \propto \rho^{\alpha_B}$, $\alpha_B \approx 0.3$ (which is consistent with rotation measure observations [14]), the radio profile can be fit by a nearly flat CRp density (Fig. 1.5e). This large flat inferred profile is suggestive that extensive streaming has already taken place. Coma thus presents an interesting challenge, to see if a significant decline in luminosity is possible despite the absence of significant CR gradients except a small one at the outer boundary. We emphasize once again that for turbulent wave damping, our solutions are independent of the magnitude of the CR gradient ∇f. Our solutions depend only on where ∇f is non-zero, and its sign.

We show our results in Fig. 1.5. All figures are analogs of those for Perseus in Fig. 1.3 (except we adopt r=300 kpc as our fiducial radius when displaying time-varying quantities—due to the much larger extent of the Coma radio halo, this is a more representative radius), and we again adopt $L_{\rm MHD} = 100$ kpc for our fiducial model. In Fig 1.5a, we see that the surface brightness falls in normalization, but does not significantly change shape, as for Perseus. The decline in $L_{1.4\rm GHz}$ is slower than for Perseus, although $L_{1.4\rm GHz}$ is still down by an order of magnitude after $\sim$ 600 Myr for the fiducial model, and declines more quickly with more vigorous turbulence as expected. Non-linear Landau damping alone produces a slow decline. While streaming is super-Alfvénic (Fig 1.5c), it does not 'run away' with time as quickly as for Perseus. The acceleration of CR streaming is tied to the decline of the CR density, which is slower in this case.

Since the flat region encompasses the entire cluster at the outset, there is no transition in energy loss regimes as for Perseus (where the profile gradually flattens). Instead, loss rates vary mildly with time (Fig 1.5d), with diffusive losses always more important than adiabatic losses, which are essentially negligible. This can be understood from the fact that adiabatic flux at the outer boundary scales with $f_{\rm p}(R_{\rm max})$, which is small (see §1.5 for more discussion), whereas the diffusive flux is independent of $f_{\rm p}(R_{\rm max})$. The flat CR density profile simply decreases in normalization with time (Fig 1.5e). Similar to Perseus, Coma's gamma-ray

flux declines quickly with time, particularly at the high energies associated with imaging air Cherenkov telescopes.

Spectral steepening in Coma's radio emission has been seen in multi-frequency observations [20], a feature which occurs naturally in our models due to the energy dependence of CR streaming. We show this in Fig 1.6; spectral steepening very similar to that observed arises. Given the flat inferred profile of Coma, which suggests that substantial streaming has already taken place, this raises the possibility that a power-law population with a slightly higher normalization was transformed by streaming into the curved population we see today.

We have chosen a rather extreme case of a completely flat profile, to illustrate that radio halo turn-off is still possible in this case. The observational data also permit an initial CR profile that is less flat. Using the same B-field, we can still reproduce the observations very well with a profile that has a mild central peak. Since we now have a significant density gradient, the radio luminosity can drop off faster in the beginning, although the overall evolution is qualitatively the same as before. The streaming speeds ramp up faster than in the flat profile fit.

We have assumed a magnetic field profile $B \propto \rho^{\alpha_{\rm B}}$, with $\alpha_{\rm B} = 0.3$. This choice assumes the B-field is in rough equipartition with turbulence, as discussed in §1.2.4, agrees with Faraday rotation measures, and enables us to reproduce the observed surface brightness distribution. However, the Faraday rotation mea-

surements are consistent with a range of values $\alpha_{\rm B} \sim 0.4 - 0.7$ at 1σ [14]. A steeper scaling of B with density implies lower B-fields at the cluster outskirts; in this case the rate of turn-off and development of spectral steepening will be slower. While lowering B decreases the Alfvén speed, the dominant effect is a decrease in the CR flux F due to streaming, which scales as $B^{3/2}/L_{\rm MHD}^{1/2}$ (equation (1.28)). The rate of CR streaming is set by the minimum value of this flux, which generally occurs at the cluster outskirts. As we shall we shall see in §1.5, in this regime we can approximate $\dot{f}_{\rm p} \approx 3F(R_f, p)/R_f$. Specializing to our model for Coma ($4\pi p^3 f_{\rm p}(t=0) \approx 10^{-13}$ cm^{-3} for $p = 100$, $n_{\rm e}(0)/n_{\rm e}(1\text{ Mpc}) \approx 17$, and $B_0 = 5\ \mu$G):

$$t_{\rm off} \sim \left.\frac{f_{\rm p}}{\dot{f}_{\rm p}}\right|_{1\text{ Mpc}} \sim 370\,{\rm Myr}\,L_{\rm MHD,100}^{1/2} 70^{\alpha_B - 0.5} \tag{1.77}$$

Thus, a steeper scaling $\alpha_{\rm B} = 0.7$ would not permit turn off on an acceptably short timescale for a very flat profile (it could still be possible for a less flat profile, as above, but note that the observations cannot be fit well by a centrally peaked CR profile with this steep B-field scaling). Note that radio relic measurements are consistent with strong, $\sim \mu$G fields at the cluster outskirts [44]; in addition, the very strong turbulence at the cluster outskirts could be consistent with lower values of $L_{\rm MHD}$ than the constant value we have assumed. As we reiterate in the Conclusions, complex issues regarding magnetic field topology and strength are best further explored with 3D MHD simulations.

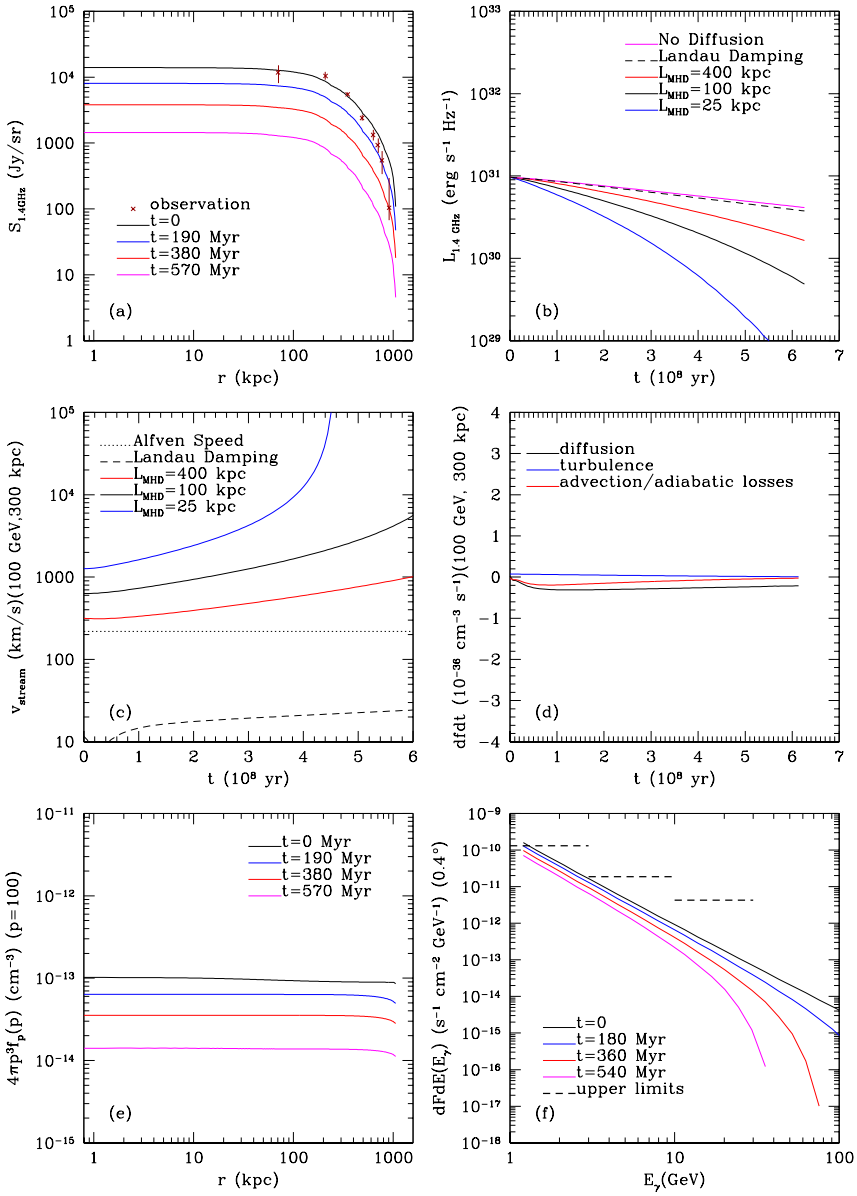

Figure 1.5: Simulation results for the Coma cluster. **(a)** Radio surface brightness of Coma for $L_{\rm MHD} = 100$ kpc. Observations from [34]. **(b)** The time evolution of the Coma cluster's radio luminosity for different levels of damping. The solid lines show MHD turbulence damping at various strengths. The dashed line shows non-linear Landau damping. **(c)** Cosmic ray streaming speeds of 100 GeV CRs at a fixed radius of 300 kpc. **(d)** Different contributions to $\dot{f}_{\rm p}$ for the $L_{\rm MHD} = 100$ kpc simulation. **(e)** Radial distribution of 100 GeV protons for $L_{\rm MHD} = 100$ kpc. **(f)** Predicted gamma-ray fluxes. Upper limits are taken from [3] with $\alpha = 2.5$.

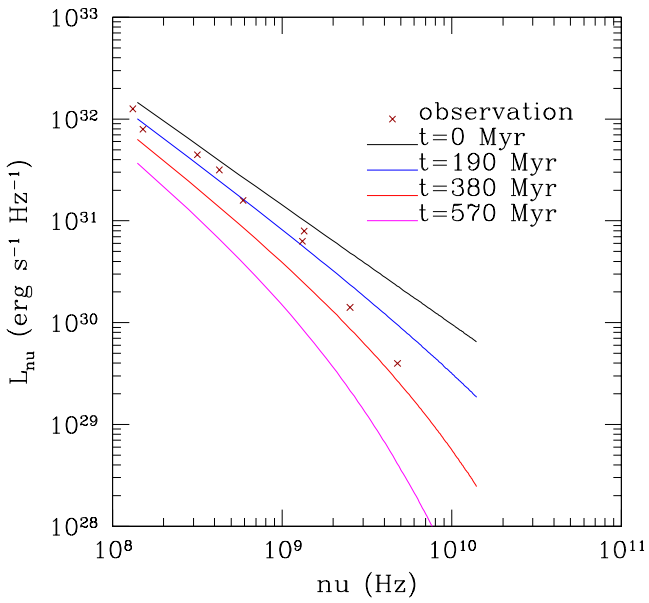

Figure 1.6: Luminosity as a function of energy for the Coma simulation including observations from [20]. The momentum dependence of the streaming speed leads to a spectral steepening very similar to observation.

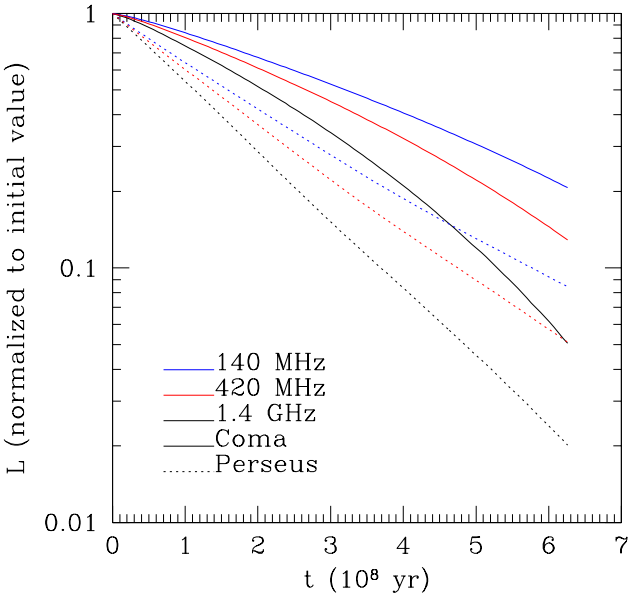

Figure 1.7: Luminosity dropoff in Coma for different frequencies. High energy CRs stream more quickly, so the higher frequency signals drop faster.

1.5 Analytic Expressions

In certain limiting cases, the evolution of the CR population can be derived analytically. These solutions serve two purposes: they serve as tests of our numerical code, particularly the regularization scheme (§1.3.1), and they also give physical insight into the behaviour of our solutions, and the circumstances under which particular processes dominate.

In the absence of sources Q and ignoring the negligible Coulomb and hadronic losses, we can write the CR transport equation (1.38) as:

$$\frac{\mathrm{D}f_{\mathrm{p}}}{\mathrm{D}t} \approx \frac{\partial f_{\mathrm{p}}}{\partial t} \approx -\nabla \cdot \mathbf{F} \tag{1.78}$$

where the total CR flux $\mathbf{F} = \mathbf{F}_{\mathrm{adia}} + \mathbf{F}_{\mathrm{str}} + \mathbf{F}_{\mathrm{turb}}$, is made up of the fluxes due to adiabatic losses in the wave frame, streaming relative to the wave frame, and turbulent advection respectively. We have approximated the Lagrangian derivative by the Eulerian derivative $\mathrm{D}f_{\mathrm{p}}/\mathrm{D}t \approx \partial f_{\mathrm{p}}/\partial t$, since $\mathbf{v}_{\mathrm{A}} \cdot \nabla f_{\mathrm{p}}$ is initially small and becomes increasingly negligible as the profile flattens.

As we have seen, the CR profile generally develops a flat inner core within some radius R_f, outside of which it declines. The flat core stems from the fact that while $\nabla \cdot \mathbf{F}$ increases inward[12], an inverted CR profile cannot develop, since CRs cannot stream up a gradient. Thus, a flat core develops, while its normalization

[12]This condition holds as long as $\mathbf{F}$ increases more slowly than r. In our case, the dominant fluxes $F_{\mathrm{stream}} \propto B^{3/2} \propto \rho^{3\alpha_{\mathrm{B}}/2}$ (equation (1.82)) clearly increases inward, and $F_{\mathrm{adia}} \propto f\mathbf{v}_{\mathrm{A}}$ is at most flat or increases inward. Thus, $|\nabla \cdot \mathbf{F}|$ clearly increases inward.

and radius R_f evolves due to the net flux of CRs from its outer boundary. In particular, if we set $\mathbf{F} = F\hat{\mathbf{r}}$ and integrate equation (1.78) over the volume of the flat region, we obtain:

$$\frac{4}{3}\pi R_f^3 \dot{f}_{\rm p}(R_f, p) = -4\pi R^2 F(R_f, p)$$

$$\dot{f}_{\rm p}(R_f, p) = -\frac{3F(R_f, p)}{R} \tag{1.79}$$

where we have used the fact that $\dot{f}_{\rm p}(r, p, t)$ is independent of r for $r < R_f$, and the divergence theorem. The evolution of the entire profile can then be described by

$$\dot{f}_{\rm p}(r, p, t) = \begin{cases} -\frac{3F(R_f,p,t)}{R_f(p,t)}, & r < R_f(p,t) \\ -\nabla \cdot \mathbf{F}(r, p, t), & r > R_f(p,t) \end{cases} \tag{1.80}$$

where the "flatness front" $R_f(p, t)$ is determined from $f_{\rm p}(0, p, t) = f_{\rm p}(R_f, p, t)$, or:

$$f_{\rm p}(0, p, 0) - \int_0^t \frac{3F(R_{\rm f}(p, t'), p, t')}{R_{\rm f}(p, t')} {\rm d}t' = f_{\rm p}(R_f, p, 0) - \int_0^t \nabla \cdot \mathbf{F}(R_{\rm f}(p, t'), p, t') dt' \tag{1.81}$$

As we have seen, $\mathbf{F}_{\rm stream}$ and $\mathbf{F}_{\rm adia}$ are the most important fluxes, while $\mathbf{F}_{\rm turb}$ is subdominant. Let us now consider the limiting cases when only one is at play.

Cosmic-Ray streaming only. We have:

$$\mathbf{F}_{\rm stream} = \frac{\Gamma_{\rm D} B^2 \hat{r}}{4\pi^3 p^3 m \Omega_0 v_{\rm A}} = F_{\rm stream} \hat{r} \tag{1.82}$$

Since $F_{\rm stream}$ is independent of $f_{\rm p}$ and depends only on plasma parameters (specifically, the B-field, turbulence and density profiles), in our model where the gas properties are time-steady (and thus in hydrostatic and thermal equilibrium), $F_{\rm stream}(r,p)$ is independent of time. Thus, $A(r,p) \equiv \nabla \cdot \mathbf{F}_{\rm stream}(r,p)$ is also time-independent, and we have for $r > R_f(p,t)$:

$$f(r,p,t) = f(r,p,0) - A(r,p)t; \quad r \geq R_f(p,t) \tag{1.83}$$

i.e., the distribution function outside the flatness front falls linearly with time. More generally, we can solve for the flatness front $R_{\rm f}$ and the overall solution both inside and outside $R_{\rm f}$ via equations (1.80) and (1.81).

To compare this analytic solution with our simulation we ran a simulation for Perseus and for Coma where only the diffusion term was used in (1.38), and all other terms ignored. The resulting CR densities for Perseus can be seen in figure 1.8. In this plot we show the CR density versus time at 100 GeV at a few select radii. The solid curves are the simulation, and the dotted lines are the analytic solution for a non-flat profile. The match is essentially perfect - the densities decrease at a constant rate (equation (1.83)) until the flatness front catches up to each radius. After this point the densities follow the same single curve corresponding to the evolution of the flat region. The same results for Coma show the agreement in the regime when the profile is already flat. In figure 1.9, the CR profile in Coma is nearly flat to begin with. Before very long the profile

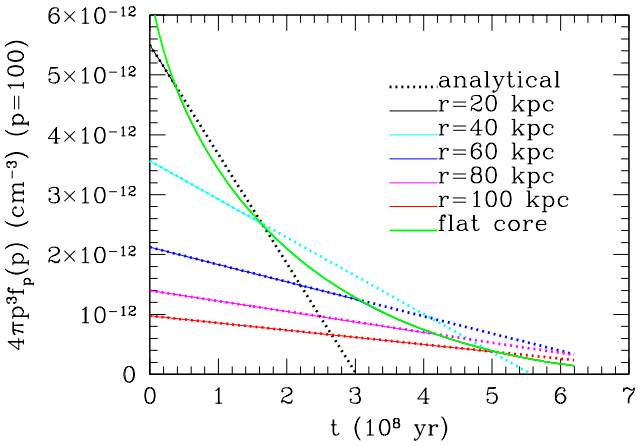

Figure 1.8: CR densities at 100 GeV for Perseus if only the flux from CR streaming $\mathbf{F}_{\rm stream}$ (equation (1.82)) is important. The dotted lines (bold curve) show the analytic solution for outside (inside) the flat front respectively; the solution initially follows the dotted curves until it intersects the green curve, when it follows the flat front solution. The solid lines show the simulation results, which match the analytic solution almost perfectly.

is flat across the entire simulated space and the $\dot{f}_{\rm p} = -3F_{\rm cr}(R_{\rm f})/R_{\rm f}$ regime kicks in. Again, the agreement between simulation and analytic solution is very good. This implies that our regularization of the CR streaming term (which is needed to prevent unphysical oscillations with such flat profiles) is not so strong that it artificially changes the rate of diffusion.

Adiabatic expansion only. We have:

$$\mathbf{F}_{\rm adia} = \frac{1}{3} p \frac{\partial f_{\rm p}}{\partial p} \mathbf{v}_{\rm A} \tag{1.84}$$

Thus, unlike the preceding case, the flux depends on the distribution function $f_{\rm p}$ and hence is time-dependent. We can readily solve this in the approximation that $v_{\rm A} \propto \rho^{\alpha_{\rm B}-0.5} \sim$ const (since it varies very weakly with radius), and $f_{\rm p} \propto p^{-\alpha}$,

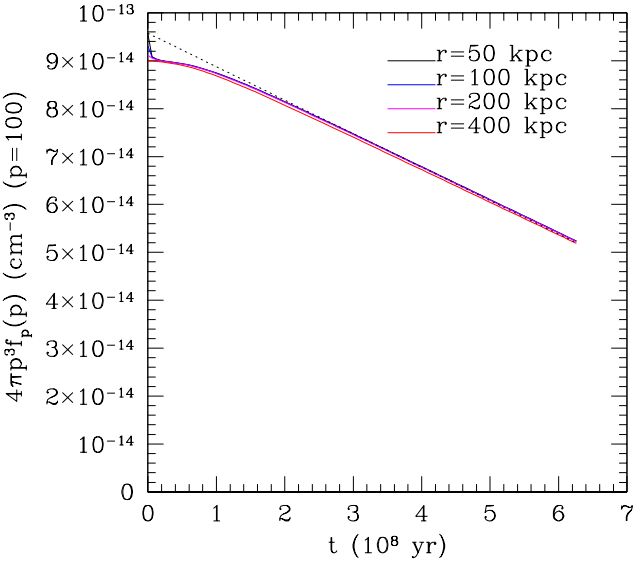

Figure 1.9: The same as for Fig 1.8 but for Coma. Since the profile is already almost flat, this is a test of the $\dot{f}_{\rm p} = -3F_{\rm cr}(R_{\rm f})/R_{\rm f} = $ constant regime.

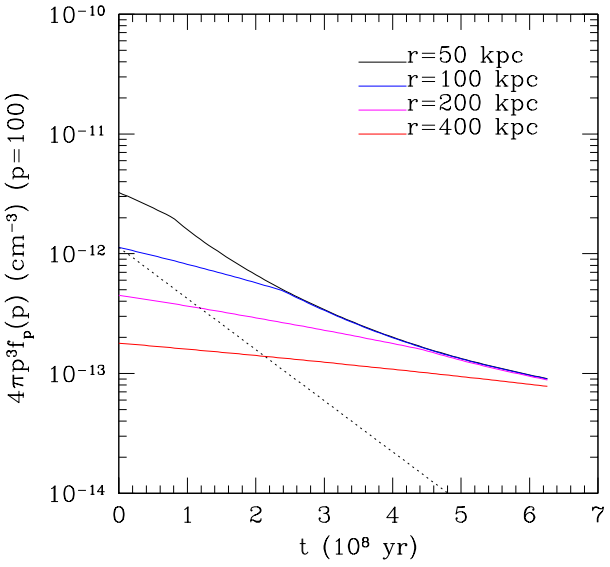

Figure 1.10: CR densities for Perseus in the absence of any diffusion, i.e. only adiabatic losses are used. The dotted line represents the analytic solution (1.85) and should be compared to the blue line.

approximately independent of radius. Then, for $r \geq R_{\rm f}$, we have $\dot{f} = \nabla \cdot \mathbf{F}_{\rm adia} \approx -2\alpha v_{\rm A} f_{\rm p}/3r$, or:

$$f_{\rm p}(r,p,t) \approx f_{\rm p}(r,p,0)\exp\left(-\frac{2\alpha v_{\rm A} t}{3r}\right); \quad r \geq R_{\rm f} \tag{1.85}$$

Thus, outside the flatness front, the distribution function falls exponentially with time, with e-folding time of order the Alfvén crossing time (which becomes long at large radii). To solve for the evolution of the flatness front and the entire profile, we insert equation (1.85) into equation (1.84) and hence equation (1.80) and (1.81). Note that we are only required to evaluate the flux $\mathbf{F}_{\rm adia}$ for $r \geq R_f$, where equation (1.85) is valid. We compare this analytic expression with a Perseus simulation that has no diffusion in Fig 1.10. The dashed line depicts (1.85) for $r = 100$ kpc and $p = 100$. Although the fit isn't perfect, the simulated values do fall exponentially with time until the flatness front catches up, with e-folding time comparable to that determined from (1.85). This is perhaps to be expected, since (1.85) assumes that the quantity $\alpha f_{\rm p}$ does not vary significantly with radius, which is not typically the case.

These solutions allow us to understand the nature of the numerical solutions we previously obtained. Coma, where the initial profile is almost completely flat, is obviously in the $\dot{f_{\rm p}} = -3F(R_{\rm max})/R_f$ regime; moreover, $\mathbf{F}_{\rm stream}(R_f) \gg \mathbf{F}_{\rm adia}(R_{\rm f})$, since the latter scales with the (small) value of the distribution function at the outer boundary. The evolution of the flatness front in Perseus is more interesting.

Initially, even though $v_{\rm D} - v_{\rm A} \sim \mathcal{O}(v_A)$, adiabatic losses dominate, since the distribution function falls exponentially with time (rather than linearly with time, for streaming losses). However, $\mathbf{F}_{\rm adia} \propto f$ also falls exponentially with time, while $\mathbf{F}_{\rm stream}$ is independent of time. Thus, streaming losses will always dominate at late times. Equivalently, the velocity associated with adiabatic losses, $v_{\rm A}$, is constant with time, while the streaming velocity $v_D \propto 1/f_{\rm p}$ increases with time: as the number density of cosmic rays fall, the confining wave amplitude $\delta B/B$ falls, and cosmic rays can stream progressively faster.

1.6 Conclusions

Shocks generated during hierarchical structure formation are expected to accelerate cosmic rays via diffusive shock acceleration. These cosmic rays in turn interact hadronically with thermal nucleons to produce pions, which decay to produce relativistic electrons. Tracking these well-understood processes, and assuming magnetic fields given by Faraday rotation measurements, leads to predictions for radio halo emission consistent with those observed [81]. However, this model predicts that *every* cluster hosts a bright radio halo. This is at odds with the observed bimodality of cluster radio emission: the majority of clusters are radio-quiet, and an order of magnitude fainter than the radio-loud population [44, 18]. Radio loudness is strongly associated with merger activity. For this reason, the

turbulent re-acceleration model [23, 80], where this association occurs naturally, is often favored. However, this still begs the question as to *why* hadronically induced radio emission is not omnipresent. All of the associated physics is well understood, and at face value the observations then require that CRp acceleration efficiencies be reduced by an order of magnitude below canonical values[13].

[36] took an important step forward when they suggested that CRp's could potentially stream super-Alfvénically, turning off radio halos. However, they assumed streaming speeds of order the sound speed $v_D \sim c_s$ instead of calculating it[14], and posited steady-state CR profiles that represent equilibria between outward streaming and inward turbulent advection, despite the long timescales for equilibration. In this paper, we attempt to place CR streaming in clusters on a more rigorous footing, by calculating the microphysical streaming speed as a function of plasma parameters in the self-confinement picture [64, 58, 113, 105]. We then solve the time-dependent CR transport equation (albeit in 1D) to see how the radio luminosity evolves with time. Our conclusions are as follows:

- CR streaming speeds depend on the source of wave damping. Non-linear Landau damping (e.g., [43], as assumed in [36]) is too weak to sufficiently inhibit wave growth, and $v_D \sim v_A$. However, if waves are instead damped

[13]A bimodality in cluster B-fields, with larger values during the turbulent, radio-loud state, appears inconsistent with cluster rotation-measure observations ([15], and references therein).

[14]In fact, given their assumptions, we find that cosmic rays should only stream Alfvénically.

by turbulent shear [118, 42], they can be sufficiently suppressed that super-Alfvénic streaming $v_{\rm D} \gg v_{\rm A}$ is possible. Moreover, $v_{\rm D} - v_{\rm A} \propto \gamma/n_{\rm CR}(>\gamma)$, (where γ is the CR Lorentz factor) so that: i) higher energy cosmic rays stream more rapidly; ii) CR streaming speeds continually increase as $n_{\rm CR}$ declines due to streaming.

- Streaming relative to the Alfvén wave frame can be incorporated into the CR transport equation via a diffusion term. For turbulent wave damping, the diffusion coefficient $\kappa \propto 1/\nabla f_{\rm p}$ (where $f_{\rm p}$ is the distribution function), so that remarkably $\nabla\cdot(\kappa\nabla f_{\rm p})$ is *independent* of $\nabla f_{\rm p}$. Thus, CRs can continue to stream unabated in giant radio halos (such as Coma) despite their fairly flat inferred CR profiles. Streaming is still sensitive to the *sign* of $\nabla f_{\rm p}$ (since CRs can only stream down a gradient), and for flat profiles we must implement numerical regularization [102] to ensure stable solutions. We test our solver for the CR distribution function against a code where CR mediated AGN heating is solved in the fluid approximation [51]. The solutions are identical. Note that CR heating is unaffected by super-Alfvénic streaming, since it scales as $\mathbf{v}_{\rm A}\cdot\nabla P_c$ and P_c is dominated by $\sim$GeV CRs, where streaming is Alfvénic.

- CR transport is thus clearly modified by ICM turbulence. Besides its effects on wave damping, turbulence can also advect CRs so that they roughly trace the gas density profile, creating a centrally peaked CR distribution. For the mildly subsonic $v_{\rm s} \sim v_{\rm A} \sim 100\,{\rm km\,s^{-1}}$ turbulence we assume, outward streaming dominates inward advection. Moreover, this trend *increases* with the amplitude of turbulence. It is therefore consistent with the flat inferred CR profiles in non cool-core clusters, which have generally stronger turbulent motions. Such a trend is hard to understand in scenarios where turbulence only draws CRs inward [36, 121].

- We then perform numerical time-dependent calculations of CR streaming, assuming an initial profile consistent with radio observations at 1.4 GHz. We find that the radio luminosity falls by an order of magnitude in several hundred Myr, both in a prototypical radio mini-halo (Perseus) and giant radio halo (Coma). The latter effect is particularly interesting in light of the flat inferred CR profile, and arises *only* for turbulent damping of MHD waves; if only non-linear Landau damping is at play, the turn-off is slow. Indeed, the inferred flatness of the CR profile suggests that streaming has already been at play in these systems. We also build an analytic model which aids in physical understanding. Adiabatic losses dominate until the profile flattens, when diffusive losses dominate. The turn-off timescale in the later

stage is set by the lowest value of the CR flux $F \propto B^{3/2}/L_{\rm MHD}$, generally at the cluster outskirts. The energy-dependence of CR streaming means that spectral curvature develops, and radio halos turn off more slowly at low frequencies, both consistent with observations [21, 20]. Streaming also rapidly diminishes the γ-ray luminosities at the $E_\gamma \sim 0.3 - 1$ TeV energies probed by imaging air Cerenkov telescopes (MAGIC, HESS, VERITAS), but not for the lower energies $E_\gamma \sim 0.1 - 3$ GeV probed by Fermi. The latter is therefore a more robust probe of the CR injection history.

The primary contribution of this paper is a physical proof of principle for turning off hadronically induced emission. Our 1D streaming calculations by nature omit important details best clarified by 3D MHD simulations. Chief amongst these are the effects of magnetic topology. We have effectively assumed radial magnetic fields in our 1D calculations. Of course, magnetic topology greatly influences the true value of macroscopic transport coefficients. There is some evidence both from observations [82] and cosmological MHD simulations [93] that outside the core, magnetic fields are largely radial, driven either by cosmological infall, or the magneto-thermal instability (MTI; [5, 78]). Alternatively, turbulence could fully tangle magnetic fields [94, 95, 77]. CRs have to follow the same field lines that

thermal particles do, albeit with a larger gyro radius[15]. As long as cross-field diffusivity remains small, transport coefficients should scale similarly; in the limit of a fully tangled field with a coherence length significantly larger than the gyro radius, a random walk in 3D rather than 1D will reduce the diffusion coefficient $\kappa_{\rm p} \rightarrow \kappa_p/3$, just as it reduces the Spitzer-Braginskii value for thermal conductivity by a factor of 3. This will effectively increase all quoted timescales in this paper for pure streaming by a factor of ~ 3. In the future, it would be interesting to conduct fully self-consistent 3D MHD simulations which include CR streaming, motivated and guided by the estimates here. We have also incorporated the advective effects of gas motions only in the diffusive approximation. Coherent bulk motions due to mergers or sloshing could potentially have stronger effects. More light on the nature of ICM motions in radio-bright halos from Astro-H (e.g., [122, 101, 100]) will surely help. We are also agnostic as to the cause of radio halo turn-on, which is clearly related to gas motions stimulated by mergers, and could be due to turbulent reacceleration of seed CRe [23, 80], inward advection of CRs from the cluster outskirts [36], or perhaps have separate mechanisms for different classes of radio halos [121]. Such issues await clarification from low frequency radio observations by LOFAR.

[15]Interestingly, 100 GeV CRs have a mean free path due to wave-particle interactions $\lambda_{\rm CR} \sim (\delta B/B)^{-2} r_{\rm L} \sim 1{-}10\,{\rm kpc} B_{\mu G}^{-1} \epsilon_{100\,{\rm GeV}} ([\delta B/B]/10^{-4})^{-2}$ which is similar to the electron collisional mean free path $\lambda_e \sim 6\,{\rm kpc}\, T_{4\,{\rm keV}}^2 n_{i,-3}$.

Acknowledgments

We acknowledge NSF grant 0908480 and NASA grant NNX12AG73G for support. We are grateful to Christoph Pfrommer for sparking our interest in this topic and stimulating discussions. We also thank Gianfranco Brunetti, Torsten Ensslin, Anders Pinzke and Ellen Zweibel for helpful conversations. SPO also thanks the KITP (supported by NSF PHY05-51164), the Aspen Center for Physics (NSF Grant No. 1066293) and UCLA for hospitality, and the Getty Center for inspiring views, during the completion of this paper.

Chapter 2

Cosmic Ray Heating in the Warm Ionized Medium

This article has been accepted for publication in The Astrophysical Journal

http://iopscience.iop.org/0004-637X/767/1/87/

2.1 Introduction

Observations of [S II]/Hα and [N II]/Hα line intensity ratios in the WIM show a spatial variation with distance from the galactic midplane $|z|$ - larger line ratios are seen further from the disk (see [91], [52]). Such variation might be

explained by variations in the ionization parameter U, the ratio of photon density to gas density. However, this would not explain the additional observation that the [S II]/[N II] ratio remains nearly constant with $|z|$. Under WIM conditions, variations in U inevitably produces larger changes in Sulphur (which can be either in the form of SII or SIII) compared to Nitrogen (which almost always appears as NII), due to their different ionization potentials.

These observations may be explained by a spatial variation of the electron temperature T_e. An increase in T_e with height above the disk could explain the enhanced [S II]/Hα and [N II]/Hα ratios. Also, because [S II] and [N II] have nearly the same excitation energy, the [S II]/[N II] ratio is nearly independent of T_e. So the near constant [S II]/[N II] ratio may also be explained this way.

But how can this variation in T_e be explained? If only photoionization heating is important, then this increase in $T_{\rm e}$ can potentially be accommodated by hardening of the spectrum away from the disk mid-plane. However, a hard spectrum is inconsistent with HeI λ5876 observations [87, 88]. On the other hand, if there were a secondary heating mechanism with a weaker dependence on electron density than the n_e^2 dependence of photoionization heating, such heating would dominate far from the disk, where densities are low, and we would see a variation in T_e that could explain the observed line ratio variations.

Many such supplementary heating mechanisms have been proposed, such as photoelectric heating from dust grains ([111]), magnetic reconnection ([89]), and turbulent dissipation ([74]). We study here the possibility of cosmic ray heating. The process was outlined by [114], but not applied to the WIM (which had not been discovered at that time). If a cosmic ray population has a bulk velocity faster than the local Alfvén speed $v_{Ai} = B/\sqrt{4\pi\rho_i}$, magnetohydrodynamic Alfvén waves are generated and exhibit unstable growth ([112], [58]). In a steady state, these waves are damped by some other process(es), transferring energy to the gas. In this way a cosmic ray density gradient can indirectly heat the plasma. We will see that the resulting gas heating rate is proportional to $n_e^{-1/2}$, and is of the order required to explain the necessary temperature variations. Note that this process is quite different from collisional cosmic ray heating ([106]). A strength of this mechanism is that the heating rate depends on only a few parameters which are either observable or can be estimated. We first consider the nature of CR trapping in the WIM in §2.2, before considering the CR heating rate and its local stability properties in §2.3.

2.2 Alfvén Wave Equilibrium

For cosmic ray heating to be in place we must ensure that Alfvén waves are present in the WIM with enough energy to scatter the cosmic rays. To do this

we determine the wave damping, which in the WIM environment is due to ion-neutral friction and non-linear Landau damping. We then balance this damping with the cosmic-ray-induced wave growth to obtain an equilibrium condition. This condition determines the power spectrum in the waves. We can then derive a mean free path for the cosmic rays and determine if they are well-trapped. We could also use the equilibrium damping rate to determine the heating of the gas, but as we will see the heating rate depends only on the characteristics of the cosmic ray population, *provided* they are well-trapped.

2.2.1 Ion-Neutral Damping in Nearly Ionized Gas

We follow Appendix C of [58]. These authors assumed the gas is nearly neutral; we assume it is almost fully ionized. We begin with the force equations for the neutral and charged components of the gas respectively. Assuming the transverse velocities of each component are in the form of an oscillator $v_i = A_i e^{i(kz-\omega t)}$, we have

$$\rho_n \omega^2 v_n = -i\nu_{ni}\omega\rho_n(v_n - v_i) \tag{2.1}$$

$$\rho_i \omega^2 v_i = \rho_i \omega_k^2 - i\nu_{in}\omega\rho_i(v_i - v_n) \tag{2.2}$$

These equations are essentially those of two coupled, damped oscillators, one of which is driven with frequency $\omega_k = kv_{Ai}$, the natural Alfvén wave frequency. The neutral-ion collisions are treated as a drag force parameterized by the collision

frequency ν_{ni}. The movement of the ions by the Alfvén waves is impeded by the neutral particle population. This nudges the neutral component to follow behind the oscillating ions, removing energy from the Alfvén waves to do so.

We can rearrange these equations into convenient matrix form by using $\nu_{ni}/\nu_{in} = \rho_i/\rho_n$:

$$(\omega^2 - \omega_k^2 + i\omega\nu_{ni})v_i - i\omega\nu_{ni}v_n = 0 \tag{2.3}$$

$$-i\omega\nu_{in}v_i + (\omega^2 + i\omega\nu_{in})v_n = 0 \tag{2.4}$$

Setting the determinant of this matrix to zero gives us the dispersion relation for ω.

$$\omega^3 + i\nu_{ni}(1 + \frac{\rho_n}{\rho_i})\omega^2 - \omega_k^2\omega - i\nu_{ni}\omega_k^2 = 0 \tag{2.5}$$

We can solve this perturbatively in the two limits $\omega_k \ll \nu_{ni}$, $\omega_k \gg \nu_{ni}$. Let us further assume we are in the $\epsilon = \rho_n/\rho_i \ll 1$ limit, to match the WIM[1]. Let's first consider the $\omega_k \ll \nu_{ni}$ case. To leading order in ω_k/ν_{ni} we have

$$i\nu_{ni}(1+\epsilon)\omega_0^2 - i\nu_{ni}\omega_k^2 = 0 \qquad \Rightarrow \omega_0 = \omega_k\sqrt{1+\epsilon} \tag{2.6}$$

The first order equation is

$$\omega_0^3 + 2i\nu_{ni}(1+\epsilon)\omega_0\omega_1 - \omega_k^2\omega_0 = 0$$

$$\Rightarrow \omega_k^3\epsilon\sqrt{1+\epsilon} + 2i\nu_{ni}(1+\epsilon)\omega_k\sqrt{1+\epsilon}\omega_1 = 0 \qquad \Rightarrow \omega_1 = -\frac{i\omega_k^2}{2\nu_{ni}}\frac{\epsilon}{1+\epsilon} \tag{2.7}$$

[1]Note that our ϵ is the inverse of the one used in [58]

So in this limit the waves are damped at a rate

$$\Gamma_{\rm in} = \frac{i\omega_k^2}{2\nu_{ni}} \frac{\epsilon}{1+\epsilon} \tag{2.8}$$

In the short wave limit, $\omega_k \gg \nu_{ni}$, which is the relevant limit for CR-generated waves, we have

$$\omega_0^3 - \omega_k^2 \omega_0 = 0 \Rightarrow \omega_0 = \omega_k \tag{2.9}$$

$$3\omega_k^2\omega_1 + i\nu_{ni}(1+\epsilon)\omega_k^2 - \omega_k^2\omega_1 - i\nu_{ni}\omega_k^2 = 0$$

$$\Rightarrow 2\omega_k^2\omega_1 + i\nu_{ni}\epsilon\omega_k^2 = 0 \qquad \Rightarrow \omega_1 = -\frac{i\nu_{ni}}{2}\epsilon = -\frac{i\nu_{in}}{2} \tag{2.10}$$

and so we have damping rate

$$\Gamma_{\rm in} = -\frac{\nu_{in}}{2} \tag{2.11}$$

Note that this is the same damping rate derived in [58], even though we are in the opposite limit of a mostly ionized gas rather than a mostly neutral one.

The ion-neutral collision frequency is

$$\nu_{in} = \frac{m_n}{m_i + m_n} n_n \langle \sigma v \rangle = \frac{1}{2} n_n \langle \sigma v \rangle = \frac{1}{2} \epsilon n_i \langle \sigma v \rangle \tag{2.12}$$

Here n_n is the density of the neutral component and $\langle \sigma v \rangle$ is the average rate of exchange of velocity per particle for ion-neutral collisions. For temperatures around 10^4 K, we have $\langle \sigma v \rangle \approx 10^{-8}$ cm^3 s^{-1} (see [61], [33]). We assume here that hydrogen is the dominant neutral species; up to 10% of the hydrogen in the WIM is thought to be neutral ([52]); He should be mostly neutral, but has a lower collision

rate ([33]). So in the short-wave, almost completely ionized limit, the ion-neutral damping rate is a function of only the density of the neutral component

$$\Gamma_{in} = -\frac{1}{4} n_n \langle \sigma v \rangle = -\frac{1}{4} \epsilon n_i \langle \sigma v \rangle. \tag{2.13}$$

2.2.2 Non-Linear Landau Damping

In some circumstances, non-linear Landau damping may be comparable to or dominate over ion-neutral damping. Non-linear Landau damping occurs when ions ride along the envelope of a beat wave formed by two interfering Alfvén waves. Ions whose random motions are slightly slower than the speed of this envelope will take energy from the waves, damping them. Ions that are slightly faster will give energy to the waves, but for a thermal distribution we expect there to be more of the slower particles, and so the net effect is a wave damping. The strength of this damping depends on the strength of the waves as ([59])

$$\Gamma_{\mathrm{NLLD}} = -\sqrt{\frac{\pi}{8}} v_i k \left(\frac{\delta B}{B} \right)_k^2 \tag{2.14}$$

Here, $v_i = \sqrt{k_B T / m}$ is the thermal speed of the ions.

2.2.3 Cosmic Ray Instability

A cosmic ray traveling along a magnetic field line with speed v and pitch angle cosine μ will interact with an Alfvén wave with parallel wave number k_z under

the resonance condition

$$k_z = \frac{\sqrt{1-\mu^2}}{\mu r_L} = \frac{\Omega_0}{\gamma v \mu} \tag{2.15}$$

Here, r_L is the cosmic ray's relativistic gyroradius, $\Omega_0 = eB_0/mc$ is its nonrelativistic gyrofrequency, and γ is its Lorentz factor. In other words, a cosmic ray and an Alfvén wave are resonant if the wave's wavelength is roughly equal to the distance the cosmic ray travels along the B-field in one gyration.

[112], [58] showed that a population of cosmic rays whose bulk velocity is faster than the Alfvén speed will spur unstable growth in the waves. If we have such a distribution of CRs $f(\mathbf{x}, \mathbf{p}, t)$, the resulting growth rate can be written, in the wave frame, ([105]):

$$\Gamma_{\text{growth}}(k_z) = \frac{\pi^2 m^2 \Omega_0^2 v_A}{2 k_z B^2} \int d^3\mathbf{p} (1-\mu^2) v \frac{\partial f}{\partial \mu} \left[\delta\left(\mu p - \frac{m\Omega_0}{k_z}\right) + \delta\left(\mu p + \frac{m\Omega_0}{k_z}\right) \right] \tag{2.16}$$

The above holds for Alfvén waves propagating nearly parallel to the background magnetic field $B\hat{z}$. From here on we drop the z subscripts. The delta functions encode the resonance condition for CRs travelling in both directions.

We can rewrite this expression in terms of the cosmic ray gradient along the background magnetic field $\frac{\partial f}{\partial z}$. In the absence of any sources or sinks, the cosmic ray transport equation is

$$\frac{\partial f}{\partial t} + \mu v \frac{\partial f}{\partial z} = \frac{\partial}{\partial \mu} \left[\frac{(1-\mu^2)}{2} \nu(\mu) \frac{\partial f}{\partial \mu} \right] \tag{2.17}$$

The scattering frequency ν is related to the energy density $\mathcal{E}$ of resonant Alfvén waves ([58]:

$$\nu(\mu) = \frac{2\pi^2\Omega}{B^2} k\mathcal{E}(k) = \frac{\pi}{4}\Omega\left(\frac{\delta B}{B}\right)^2, \qquad k = \frac{1}{|\mu| r_L} \tag{2.18}$$

This collision frequency is expected to be very large compared to the cosmic ray dynamical timescale (a condition we must check later for consistency), so we can expand f in inverse powers of ν, $f = f_0 + f_1 + f_2 + ...$ To lowest order, eqn. (2.17) becomes

$$0 = \frac{\partial}{\partial\mu}\left[\frac{(1-\mu^2)}{2}\nu(\mu)\frac{\partial f_0}{\partial\mu}\right] \Rightarrow \frac{\partial f_0}{\partial\mu} = 0 \tag{2.19}$$

To first order we have

$$\mu v\frac{\partial f_0}{\partial z} = \frac{\partial}{\partial\mu}\left[\frac{(1-\mu^2)}{2}\nu(\mu)\frac{\partial f_1}{\partial\mu}\right] \tag{2.20}$$

If we integrate both sides over μ,

$$\frac{\partial f_1}{\partial\mu} = -\frac{v}{\nu}\frac{\partial f_0}{\partial z} \tag{2.21}$$

We can now eliminate $\frac{\partial f}{\partial\mu}$ from eqn 2.16:

$$\Gamma_{\rm growth}(k) = -\frac{\pi^2 m^2\Omega_0^2 v_A}{2kB^2}\int d^3\mathbf{p}(1-\mu^2)\frac{v^2}{\nu}\frac{\partial f}{\partial z}\left[\delta\left(\mu p - \frac{m\Omega_0}{k}\right) + \delta\left(\mu p + \frac{m\Omega_0}{k}\right)\right] \tag{2.22}$$

Plugging in equation (2.18) for ν we have

$$\Gamma_{\rm growth}(k) = -\frac{2\pi m^2\Omega_0^2 v_A}{k\Omega(\delta B)_k^2}\int d^3p(1-\mu^2)v^2\frac{\partial f}{\partial z}\left[\delta\left(\mu p - \frac{m\Omega_0}{k}\right) + \delta\left(\mu p + \frac{m\Omega_0}{k}\right)\right]$$
$$= -\frac{2\pi m\Omega_0 v_A}{k(\delta B)_k^2}\int_0^\infty 2\pi p^2 dp\int_{-1}^1 d\mu(1-\mu^2)pv\frac{\partial f}{\partial z}\left[\delta\left(\mu p - \frac{m\Omega_0}{k}\right) + \delta\left(\mu p + \frac{m\Omega_0}{k}\right)\right]$$

Integrating the delta function over μ gives

$$\Gamma_{\rm growth}(k) = -\frac{8\pi^2 m\Omega_0 v_A}{k(\delta B)_k^2}\int_{p_k}^{\infty} dpv\frac{\partial f}{\partial z}(p^2-p_k^2) \tag{2.23}$$

where we have denoted $p_k = m\Omega_0/k$.

To make eqn. (2.23) look a bit simpler, let us rewrite the integral in terms of a unitless factor of order unity $A(k)$:

$$\int_{p_k}^{\infty} dpvf(p)(p^2-p_k^2) \equiv \frac{1}{4\pi}cn_{\rm CR}A(k)$$

$$A(k) = \frac{1}{n_{\rm CR}}\int_{p_k}^{\infty} dp\beta f(p)4\pi(p^2-p_k^2), \qquad 0 \le A(k) \le 1 \tag{2.24}$$

and let's define a CR length scale by

$$-\frac{\partial n_{\rm CR}}{\partial z} \equiv \frac{n_{\rm CR}}{L_{\rm CR}} \tag{2.25}$$

The growth rate is then[2]

$$\boxed{\Gamma_{\rm growth}(k) = \frac{2\pi m\Omega_0 v_A c}{k(\delta B)^2}\frac{n_{\rm CR}}{L_{CR}}A(k)} \tag{2.26}$$

Without specifying a cosmic ray distribution f we cannot say anything about $A(k)$. As an example, consider a power law in momentum, $f(\mathbf{x},p,t) = C(\mathbf{x},t)p^{-\alpha}$, with some lower momentum cutoff p_c and normalization:

$$n_{\rm CR}(\mathbf{x},t) = \int_{p_c}^{\infty} 4\pi p^2 f(\mathbf{x},p,t)dp = \frac{4\pi}{\alpha-3}Cp_c^{3-\alpha}$$

[2]In principle the quantity $A(k)$ could vary in space, but we ignore this possibility here. Alternatively we could adjust our definition of $L_{\rm CR}$ to include this effect.

$$\Rightarrow f(\mathbf{x},p,t) = n_{\rm CR}(\mathbf{x},t)\frac{\alpha-3}{4\pi p_c^3}\left(\frac{p}{p_c}\right)^{-\alpha}\Theta(p-p_c) \tag{2.27}$$

Then by definition (2.24) we get

$$A(k) = \frac{\alpha-3}{4\pi p_c^3}\int_{p_k}^{\infty} dp\beta 4\pi(p^2-p_k^2)\left(\frac{p}{p_c}\right)^{-\alpha}\Theta(p-p_c)$$

$$= (\alpha-3)\int_{\max(x_k,1)}^{\infty} dx\beta(x^{2-\alpha}-x_k^2x^{-\alpha}), \qquad x\equiv\frac{p}{p_c} \qquad x_k\equiv\frac{p_k}{p_c}$$

If we take the relativistic limit $\beta\approx 1$ and denote $\max(x_k,1)=y_k$ this becomes

$$A(k) = (\alpha-3)\left[-\frac{y_k^{3-\alpha}}{3-\alpha}+\frac{x_k^2y_k^{1-\alpha}}{1-\alpha}\right] = y_k^{1-\alpha}\left[y_k^2-\frac{\alpha-3}{\alpha-1}x_k^2\right]$$

or

$$A(k) = \begin{cases} \frac{2}{\alpha-1}\left(\frac{k}{k_c}\right)^{\alpha-3} & k<k_c \\ \left[1-\frac{\alpha-3}{\alpha-1}\left(\frac{k_c}{k}\right)^2\right] & k>k_c \end{cases} \tag{2.28}$$

where $k_c = m\Omega_0/p_c$ is determined from the lower momentum cutoff of the spectrum.

2.2.4 Equilibrium Power Spectrum

Now that we have the total damping and growth rates of the Alfvén waves we can enforce an equilibrium condition

$$\Gamma_{\rm growth}+\Gamma_{\rm in}+\Gamma_{\rm NLLD}=0 \tag{2.29}$$

Inserting our expressions (2.14), and (2.26) into eqn. (2.29),

$$\frac{2\pi m\Omega_0 v_A c}{k(\delta B)^2}\frac{n_{\rm CR}}{L_{CR}}A(k)-\Gamma_{in}-\sqrt{\frac{\pi}{8}}v_i k\left(\frac{\delta B}{B}\right)_k^2=0$$

or, rearranging terms,

$$\sqrt{\frac{\pi}{8}} v_i k^2 \mathcal{X}^2 + \Gamma_{in} k \mathcal{X} - \frac{2\pi m \Omega_0 v_A c}{B^2} \frac{n_{\rm CR}}{L_{CR}} A(k) = 0, \qquad \mathcal{X} \equiv \left(\frac{\delta B}{B}\right)_k^2$$

We solve analytically for $\mathcal{X}$

$$\left(\frac{\delta B}{B}\right)_k^2 = \sqrt{\frac{2}{\pi}} \frac{\Gamma_{in}}{k v_i} [-1 + \sqrt{1+\mathcal{R}}], \qquad \mathcal{R} \equiv \sqrt{\frac{\pi}{2}} \frac{c}{v_A} \frac{r_i}{L_{CR}} \frac{n_{CR}}{n_i} \frac{\Omega_0^2}{\Gamma_{in}^2} A(k), \quad (2.30)$$

where $r_i \equiv v_i/\Omega_0$ is the thermal ion gyroradius.

It is informative to determine the relative importance of each damping mechanism. We can do this by looking at the quantity $\mathcal{R}$. If $\mathcal{R}$ is small, the linear term (ion-neutral damping) dominates and

$$\left(\frac{\delta B}{B}\right)_k^2 \approx \frac{1}{2} \frac{c}{v_A} \frac{n_{CR}}{n_i} \frac{\Omega_0 A(k)}{k L_{CR} \Gamma_{in}}, \qquad \mathcal{R} \ll 1. \quad (2.31)$$

while if $\mathcal{R}$ is large, non-linear Landau damping dominates, and

$$\left(\frac{\delta B}{B}\right)_k^2 \approx \left(\sqrt{\frac{2}{\pi}} \frac{c}{v_A} \frac{n_{CR}}{n_i} \frac{A(k)}{k^2 r_i L_{CR}}\right)^{1/2}, \qquad \mathcal{R} \gg 1. \quad (2.32)$$

The transition between these two limiting cases occurs at $\mathcal{R} = 1$, or

$$A(k) \approx 2.8 \times 10^{-4} \left(\frac{v_i}{10^6 \text{ cm/s}}\right)^{-1} \left(\frac{n_i}{.01 \text{ cm}^{-3}}\right)^{5/2} \left(\frac{n_{\rm CR}}{10^{-9} \text{ cm}^{-3}}\right)^{-1} \left(\frac{L_{\rm CR}}{\text{kpc}}\right) \left(\frac{\epsilon}{.05}\right)^2 \quad (2.33)$$

where we have used eqn. (2.13) and taken $\langle \sigma v \rangle = 10^{-8}$ cm^3 s^{-1}. We introduce here a set of convenient fiducial values that we will use throughout this paper. For the power law spectrum with $\alpha = 4.7$ this gives us a transition wave number

k^* of

$$k^* \approx .012 k_c = .012 \frac{eB}{p_c c} = 3.6 \times 10^{-15} \text{ cm}^{-1} \left(\frac{B}{\mu\text{G}}\right) \left(\frac{p_c c}{\text{GeV}}\right)^{-1} \tag{2.34}$$

at the fiducial values in (2.33)[3]. For $k \ll k^*$, ion-neutral damping dominates and the wave power is given by (2.31). For $k \gg k^*$, non-linear Landau damping is dominant and the wave power is (2.32).

We are now in a position to check whether the cosmic rays are self-trapped, i.e. whether their mean free path to scattering by self generated turbulence is small compared to their scale height. This is a necessary condition for applying the heating theory derived in §§2.2.5 and 2.3. The mean free path λ is related to the scattering frequency given in eqn. (2.18) by

$$\lambda = \frac{v}{\nu}. \tag{2.35}$$

Using eqns. (2.18) and (2.30) in eqn. (2.35) yields a relatively compact expression for λ

$$\lambda = \sqrt{\frac{8}{\pi}} \frac{v_i}{\Gamma_{in}} \left(-1 + \sqrt{1 + \mathcal{R}}\right)^{-1}. \tag{2.36}$$

The mean free path in pc given by eqn. (2.36) is plotted as a function of p in units of the cutoff momentum p_c in Figure 2.1. The figure spans the transition from Landau damping dominated at low momentum to ion-neutral friction dominated

[3]We note here that the value of k^* depends heavily on these quantities, particularly the gas density n_i. In fact, for some values there is no region of k-space where non-linear Landau damping dominates.

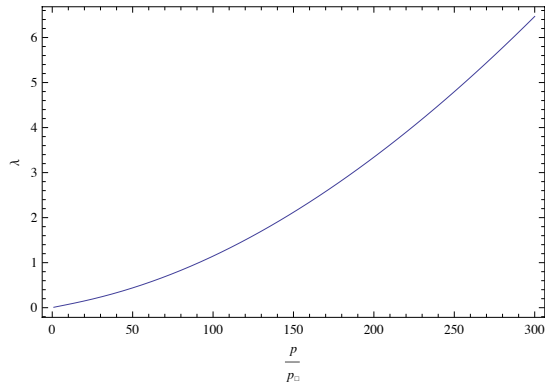

Figure 2.1: Cosmic ray mean free path to scattering by self generated turbulence, calculated from eqn. (2.36) with the parameters set equal to the fiducial values. The mean free path is given in pc and the cosmic ray momentum is given in terms of the cutoff momentum p_c.

at high momentum. It appears from Figure 2.1 that cosmic rays of energy even several hundred times the cutoff energy are quite well trapped ($\lambda \sim$ several pc). Most of the cosmic ray energy lies in the trans-relativistic ∼GeV regime. In the ISM, the spectra turns over at $p_{\rm c} \sim 10$ MeV due to Coulomb cooling. Thus, the regime of interest is $p/p_{\rm c} \sim 100$. At the upper end of the trapped range, where eqn. (2.31) holds, eqn. (2.36) can be written in the form

$$\frac{\lambda}{L_{CR}} \approx \frac{8}{\pi}\frac{\Gamma_{in}}{\Omega_0}\frac{v_A}{c}\frac{n_i}{n_{CR}A(k)} \rightarrow 4.0\times10^{-7}\left(\frac{p}{p_c}\right)^{1.7}, \tag{2.37}$$

where in the last expression we have used eqn. (2.28) and set all parameters to their fiducial values.

Figure 2.1 can also be used to check that the waves are small amplitude and well described by linear theory. From eqns. (2.18) and (2.35) was can see that

$(\delta B/B)_k^2 \sim r_L/\lambda$. Cosmic rays of energy a few hundred GeV and less have gyroradii of order 10s of AU or less, showing that $\delta B/B \ll 1$ even at low momenta where the mean free path is short.

2.2.5 Heating Rate

We can now determine the heating rate of the WIM due to the dissipation of Alfvén waves created by cosmic ray streaming. To do this we want to integrate the time-derivative of $\mathcal{E}(k) = \delta B_k^2/8\pi k$ over all wave numbers k. We know that the time-dependence of δB in an Alfvén wave is

$$\delta B \propto e^{-i\omega t} \tag{2.38}$$

$$\omega = \omega_R + i\Gamma_{\rm damp}$$

and so

$$\mathcal{E}(k) = \frac{\delta B_k^2}{8\pi k} \propto e^{2\Gamma_{\rm damp}t} \Rightarrow \frac{\partial \mathcal{E}(k)}{\partial t} = 2\Gamma_{\rm damp}\mathcal{E}(k) \tag{2.39}$$

(note that $\Gamma_{\rm damp} < 0$).

Let us remove the assumption of a power law spectrum and a relativistic limit and go back to any general distribution $f(\mathbf{x}, p, t)$. Let us also remove any assumptions about damping mechanisms, and only assume we have equilibrium for the Alfvén waves. Then from equation (2.26) and $\Gamma_{\rm growth} = \Gamma_{\rm damp}$,

$$H = \int_0^\infty dk 2\Gamma_{\rm damp}(k)\frac{\delta B_k^2}{8\pi k} = \int_0^\infty dk \Gamma_{\rm damp}(k)\frac{m\Omega_0 v_A c}{2\Gamma_{\rm damp}(k)k^2}\frac{n_{\rm CR}}{L_{CR}}A(k) \tag{2.40}$$

$$H = -\int_0^\infty dk \frac{m\Omega_0 v_A c}{2k^2} \frac{\partial}{\partial z} \left[\int_{p_k}^\infty dp \beta f(p) 4\pi (p^2 - p_k^2) \right] \tag{2.41}$$

In the last step we have rewritten $A(k)$ and $L_{\rm CR}$ in terms of their original definitions (2.24) and (2.25). We reformulate this double integral with a change of variable from k to p_k, $dp_k = -m\Omega_0/k^2 dk$. Let us also write $\mathbf{v_A} = v_A \mathbf{n}$ such that

$$H = -\frac{1}{2}\mathbf{v_A} \cdot \nabla \left[\int_0^\infty dp_k \int_{p_k}^\infty dp 4\pi f(p) v(p) (p^2 - p_k^2) \right] \tag{2.42}$$

Finally, let's exchange the order of the integrals by recognizing that the double integral is over all (p, p_k) under the constraint $0 \leq p_k \leq p$.

$$H = -\frac{1}{2}\mathbf{v_A} \cdot \nabla \left[\int_0^\infty dp \int_0^p dp_k 4\pi f(p) v(p) (p^2 - p_k^2) \right]$$

$$H = -\frac{1}{2}\mathbf{v_A} \cdot \nabla \left[\int_0^\infty dp 4\pi p^3 f(p) v(p) - \frac{1}{3} \int_0^\infty dp 4\pi p^3 f(p) v(p) \right] \tag{2.43}$$

These integrals are now very simple - they correspond to the total cosmic ray pressure

$$P_{\rm CR} = \frac{1}{3} \int_0^\infty dp 4\pi p^2 f(p) v(p) \tag{2.44}$$

We therefore obtain the very simple expression for the cosmic ray heating:

$$\boxed{H = -\mathbf{v_A} \cdot \nabla P_{\rm CR}} \tag{2.45}$$

in agreement with [114].

The heating rate is simply the cosmic ray pressure gradient times the Alfvén speed. Even without the above calculation we know this *must* be the solution,

since we require an equilibrium for the waves and (2.45) is always the rate at which cosmic rays give energy to the Alfvén waves regardless of damping ([70]). So, as hinted at in section 2.2, we require *only* that the Alfvén waves are in equilibrium and the cosmic rays are well-trapped to know that the cosmic ray heating is (2.45).

2.3 Application to our Galaxy

2.3.1 Observations

Let us carry through the dependence of v_A on the magnetic field and ion density, and pick some representative values. To write the cosmic ray pressure in terms of the energy density, we use $P_{\rm CR} = 0.45 E_{\rm CR}$ from [47]. Then we can estimate the heating rate in the WIM:

$$H \approx 5.2 \times 10^{-28} \frac{\rm erg}{\rm cm^3\ s} \frac{E_{\rm CR}}{\rm eV cm^{-3}} \frac{B}{\mu \rm G} \left(\frac{L}{\rm kpc}\right)^{-1} \left(\frac{n_i}{10^{-2}\ \rm cm^{-3}}\right)^{-1/2} \tag{2.46}$$

If we assume the cosmic ray energy density and magnetic energy density fall off with the same scale height L, we can determine the dependence of this heating rate on height z from the galactic plane

$$B(z) = B_0 e^{-|z|/2L}, \qquad E_{\rm CR}(z) = E_{\rm CR,0} e^{-|z|/L} \tag{2.47}$$

$$H(z) \approx 5.2 \times 10^{-28} \frac{\rm erg}{\rm cm^3\ s} \frac{E_{\rm CR,0}}{\rm eV cm^{-3}} \frac{B_0}{\mu \rm G} \left(\frac{L}{\rm kpc}\right)^{-1} \left(\frac{n_i}{10^{-2}\ \rm cm^{-3}}\right)^{-1/2} e^{-3|z|/2L} \tag{2.48}$$

Let's compare this to the heating that would be necessary to explain the inferred temperature profile $T(z)$. Following the prescription in [91] we find $T(z)$ in our model by solving a heating-cooling balance equation

$$G_0 n_e^2 + G_3 n_e^{-1/2} = \Lambda n_e^2 \tag{2.49}$$

where each term represents, from left to right, photoionization heating, cosmic ray heating, and the cooling rate. The temperature dependence of the electron density n_e, the cooling function Λ, and the photoionization heating G_0 are

$$n_e(|z|) = 0.125 T_4^{0.45} f^{-0.5} e^{-|z|/1\mathrm{kpc}}\,\mathrm{cm}^{-3} \tag{2.50}$$

$$\Lambda = 3.0 \times 10^{-24} T_4^{1.9}\ \mathrm{erg\ cm^3\ s^{-1}} \tag{2.51}$$

$$G_0 = 1.2 \times 10^{-24} T_4^{-0.8}\ \mathrm{erg\ cm^3\ s^{-1}} \tag{2.52}$$

T_4 denotes the temperature in units of 10^4 K, and f is a filling fraction describing the amount of ionized Hydrogen, which we will set to $f(z) = \mathrm{Min}[0.1e^{|z|/750\mathrm{pc}}, 1]$. Note that our assumptions imply that $\nabla P_\mathrm{c} < \rho g$ at all z, and is consistent with hydrostatic balance.

We then solve eqn 2.49 to obtain the model profile $T(z)$ and compare it to the profile infered from line ratio observations. We adjust G_3 to fit the model curve to the data, and we find, for $L = 2$ kpc:

$$G_{3,\mathrm{fit}} \approx 1.2 \times 10^{-27} \frac{\mathrm{erg}}{\mathrm{cm}^{9/2}\ \mathrm{s}} e^{-3|z|/4000\ \mathrm{pc}} \tag{2.53}$$

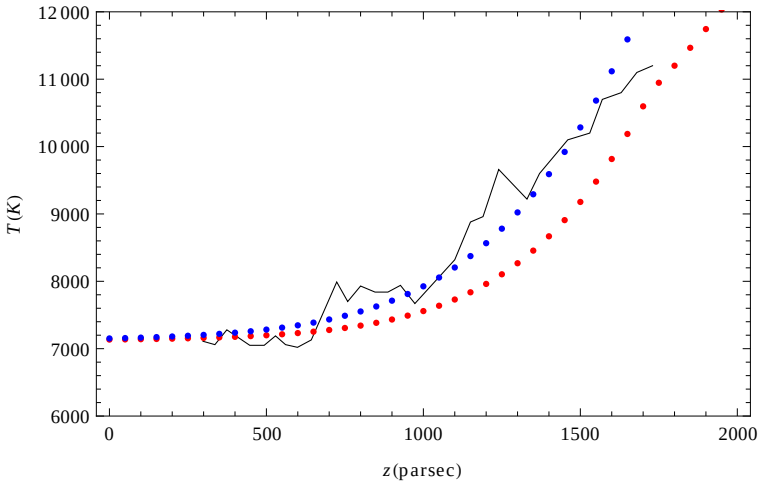

Figure 2.2: Temperature versus height for the WIM. The black line is derived from observations of line ratios in the Perseus spiral arm. The blue points show the fit solution using the above parameters. The red points show the profile using parameters based on observations.

$$\Rightarrow H_{\rm fit} = G_{3,\rm fit} n_e^{-1/2} = 1.2 \times 10^{-26} \frac{\rm erg}{\rm cm^3\ s} \left(\frac{n_i}{10^{-2}\ \rm cm^{-3}} \right)^{-1/2} e^{-3|z|/4000\ \rm pc} \tag{2.54}$$

See figure 2.2 (blue points) for this fit.

Comparing this to equation (2.48) with $L_{\rm CR} = 2$ kpc, we see that cosmic ray heating is sufficient to explain the observed line ratios if the magnetic field and CR energy density normalizations are high enough:

$$\frac{E_{\rm CR,0}}{\rm eV cm^{-3}} \frac{B_0}{\mu \rm G} \approx 46 \tag{2.55}$$

Is this the case? The magnetic field and CR energy density in the solar neighborhood are about $B_0 = 5\ \mu$G and $E_{\rm CR,0} = 1.8$ ev cm^{-3} ([47]). [11] showed that synchrotron emissivity in the galactic spiral arms is about 4 times greater than in the interarm regions. Synchrotron emissivity depends on the field and CR density

as ([83])

$$j_\nu \propto E_{\rm CR} B^{\alpha/2+1} \propto B^{\alpha/2+3} \tag{2.56}$$

for a power law CR density. We utilize our equipartition assumption in the last step. A spiral-arm enhancement of j_ν by a factor of 4 therefore implies the B-field increases by a factor of about 1.4 and the CR density increases by about 1.9 (for $\alpha = 4.7$). We might then expect the product of the B-field and the CR density in the Perseus arm to be about

$$E_{\rm CR,0} B_0 \approx (1.8 \text{ eV cm}^{-3})(5\ \mu\text{G}) * 1.4 * 1.9 \approx 24\ \mu\text{G eV cm}^{-3} \tag{2.57}$$

This falls short of the requirement from equation (2.55) but still comes close to reproducing the inferred temperature profile, as shown in the red points in figure 2.2. We also have not incorporated the orientation of the magnetic field. We have assumed a vertical field, but the actual field in the WIM may be much more random. This might be accounted for with an effective efficiency parameter.

One complication these estimates do not fully take into account is the multi-phase nature of the ISM: the WIM has a low ($\sim 20\%$) filling factor, and above the disk is interspersed with hot diffuse coronal gas. This can cause local variations in Alfven speed, and thus cosmic ray pressure. As long as B increases more slowly than $n_e^{1/2}$ (note that in the cooler diffuse ISM sampled by HI lines, B as measured by Zeeman splitting does not scale with density [32]), v_A will be reduced in the WIM relative to coronal gas, and thus P_c is higher. Thus, the relevant length scale

for cosmic ray pressure gradients could be the cloud size, rather than the global scale height we have adopted; this leads to larger heating rates[4]. On the other hand, if clouds are sufficiently small ($L_{\rm cloud} \lesssim \lambda \sim 10$pc), then the CRs smooth over these inhomogeneities and the global gradients are appropriate. Hα observations and photoionization modeling indicate that the WIM is likely to have both a smooth and a clumpy component which fluctuates on a wide range of length scales, but there is no consensus picture [52]. We regard these issues as beyond the scope of this paper, but such considerations are illustrative of possible variations in the cosmic rate heating rate.

2.3.2 Stability

We must check that the heating from the cosmic ray pressure gradient is stable under perturbations. If the heating increases compared to the cooling for a small element of gas perturbed to a higher temperature, the heating is unstable and we would get thermal runaway. To determine if this is the case, we need the change in the heating rate for a given perturbation.

$$\delta(\Lambda n^2 - H) = \delta(L_0 n^2 T^{1.9} - H_0 n^2 T^{-0.8} - H_3 B E_{\rm CR} n^{-1/2}) \qquad (2.58)$$

[4]It also implies most heating occurs when the cosmic rays exit the cloud, when $v_{\rm A} \cdot \nabla P_{\rm c} < 0$.

In terms of perturbed quantities this becomes

$$= L_0 n^2 T^2 \left(2\frac{\delta n}{n} + 1.9\frac{\delta T}{T}\right) - H_0 n^2 T^{-0.8} \left(2\frac{\delta n}{n} - 0.8\frac{\delta T}{T}\right) - H_3 B E_{\rm CR} n^{-1/2} \left(\frac{\delta B}{B} + \frac{\delta E_{\rm CR}}{E_{\rm CR}} - \frac{1}{2}\frac{\delta n}{n}\right) \quad (2.59)$$

Making use of the fact that the initial state was in thermal equilibrium, $L_0 n^2 T^2 = H_0 n^2 T^{-0.8} + H_3 B E_{\rm CR} n^{-1/2}$, we can write this most generally as

$$\begin{aligned}\delta(\Lambda n^2 - H) &= \frac{\delta T}{T}\left[1.9 L_0 n^2 T^{1.9} + 0.8 H_0 n^2 T^{-0.8}\right] \\ &+ \frac{\delta n}{n}\left[2 L_0 n^2 T^{1.9} - 2 H_0 n^2 T^{-0.8} - \frac{1}{2} H_3 B E_{\rm CR} n^{-1/2}\right] - H_3 B E_{\rm CR} n^{-1/2}\left(\frac{\delta B}{B} + \frac{\delta E_{\rm CR}}{E_{\rm CR}}\right) \\ &= \frac{\delta T}{T}\left[1.9 L_0 n^2 T^{1.9} + 0.8 H_0 n^2 T^{-0.8}\right] - H_3 B E_{\rm CR} n^{-1/2}\left(\frac{3}{2}\frac{\delta n}{n} + \frac{\delta B}{B} + \frac{\delta E_{\rm CR}}{E_{\rm CR}}\right)\end{aligned} \quad (2.60)$$

Without specifying the perturbation this is as far as we can go. Once we relate the perturbed quantities with δT, we can determine whether the heating is stable or unstable.

Let us consider an isobaric perturbation perpendicular to the magnetic field lines. The total pressure remains constant

$$P_{\rm tot} = P_g + P_B + P_{\rm CR} = const. \quad (2.61)$$

The above terms represent the gas pressure, magnetic pressure, and CR pressure respectively. The field lines are compressed along with the gas, so

$$\frac{\delta B}{B} = \frac{\delta n}{n} \quad (2.62)$$

Let us further assume that the cosmic rays respond adiabatically:

$$\frac{\delta E_{\rm CR}}{E_{\rm CR}} = \frac{\delta P_{\rm CR}}{P_{\rm CR}} = \gamma_{\rm CR}\frac{\delta n}{n} \tag{2.63}$$

Then we can use the constant pressure condition to relate δn and δT. From $P_g \propto nT$ and $P_B \propto B^2$ we get

$$\delta P_{\rm tot} = \delta P_g + \delta P_B + \delta P_{\rm CR} = 0$$

$$P_g\left(\frac{\delta n}{n} + \frac{\delta T}{T}\right) + 2P_B\frac{\delta B}{B} + \gamma_{\rm CR}P_{\rm CR}\frac{\delta n}{n} = 0$$

$$\frac{\delta n}{n} = -\frac{P_g}{P_g + 2P_B + \gamma_{\rm CR}P_{\rm CR}}\frac{\delta T}{T} \tag{2.64}$$

Putting this all together into equation (2.60) gives

$$\delta(\Lambda n^2 - H) = \frac{\delta T}{T}\left[1.9L_0n^2T^{1.9} + 0.8H_0n^2T^{-0.8} - H_3BE_{\rm CR}n^{-1/2}\left(\frac{3}{2} - \gamma_{\rm CR}\right)\left(\frac{P_g}{P_g + 2P_B + \gamma_{\rm CR}P_{\rm CR}}\right)\right] \tag{2.65}$$

If the term in the brackets is positive, a small increase in temperature causes the change in cooling to outweigh the change in heating and the perturbation is stable. If the term in brackets is negative, it is unstable. But note that both parenthesised factors in the third term must each be less than one. Also, by the thermal equilibrium condition, $H_3BE_{\rm CR}n^{-1/2}$ must be less than $L_0n^2T^{1.9}$. The first term must therefore be of higher magnitude than the third term, and so the expression in the brackets is positive and the heating is stable.

This is perhaps easier seen if we denote the total cooling by C, and the fraction of the total heating due to photoelectric heating by $0 \leq x \leq 1$. Then,

$$\delta(\Lambda n^2 - H) = C\frac{\delta T}{T}\left[1.9 + 0.8x - (1-x)\left(\frac{3}{2} - \gamma_{\rm CR}\right)\left(\frac{P_g}{P_g + 2P_B + \gamma_{\rm CR}P_{\rm CR}}\right)\right] \tag{2.66}$$

Now let us consider an acoustic perturbation. Equations (2.60),(2.62),and (2.63) still hold. Pressure is no longer fixed, but the gas responds almost adiabatically. As such

$$\frac{P_g}{\rho^{\gamma_g}} = const. \rightarrow \delta\left(\frac{P_g}{\rho^{\gamma_g}}\right) = 0 \tag{2.67}$$

$$\Rightarrow \frac{P_g}{\rho^{\gamma_g}}\left(\frac{\delta P_g}{P_g} - \gamma_g\frac{\delta\rho}{\rho}\right) = \frac{P_g}{\rho^{\gamma_g}}\left(\frac{\delta T}{T} + (1-\gamma_g)\frac{\delta n}{n}\right) = 0 \Rightarrow \frac{\delta n}{n} = \frac{1}{\gamma_g - 1}\frac{\delta T}{T} \tag{2.68}$$

We therefore have

$$\delta(\Lambda n^2 - H) = \frac{\delta T}{T}\left[1.9L_0 n^2 T^{1.9} + 0.8H_0 n^2 T^{-0.8} - H_3 B E_{\rm CR} n^{-1/2}\frac{3/2 - \gamma_{\rm CR}}{\gamma_g - 1}\right] \tag{2.69}$$

or, in terms of C and x,

$$\delta(\Lambda n^2 - H) = C\frac{\delta T}{T}\left[1.9 + 0.8x - (1-x)\frac{3/2 - \gamma_{\rm CR}}{\gamma_g - 1}\right] \tag{2.70}$$

By a similar argument as before, this is also stable.

2.4 Summary and Conclusions

The gaseous disk of the Milky Way has a warm ionized component (WIM) with scale height several times that of the predominantly neutral component. The magnetic field and cosmic ray components have similar thickness. Thick layers of warm ionized gas, and extended nonthermal emission, are seen in other galaxies as well [52].

It is widely accepted that starlight photoionizes and heats the WIM. Nevertheless, there is evidence for a supplemental heating mechanism. Detailed reconstruction of the WIM vertical temperature profile in the region of the Perseus spiral arm shows an increase in temperature with height that cannot be explained by radiative heating alone ([91]). These authors showed that these observations can be explained by an additional heating mechanism with a weaker density dependence than the n^2 dependence of radiative heating. Heating by magnetic reconnection ([89]), dissipation of turbulence ([74]), and photoelectric heating by dust ([111]) have all been invoked. All three are feasible on energetic grounds, but the rates of the first two, in particular, depend on many unknown factors and are quite uncertain.

In this paper, we estimated the heating rate due to dissipation of waves excited by streaming cosmic rays. When the cosmic rays are well scattered by this self-generated turbulence, the heating rate depends only on the cosmic ray pressure

gradient projected along the local magnetic field direction and the magnitude of the Alfvén speed (eqn. 2.45). Cosmic ray heating of the interstellar medium was discussed in general in [114] and is included in models of supernova driven shock waves ([108]), cosmic ray driven galactic winds ([16], [41]), and diffuse interstellar clouds ([40]) but up to now does not appear to have been considered for the WIM. In §2 we showed that when wave excitation by streaming is balanced against nonlinear Landau damping and ion-neutral friction, the resulting wave amplitude, while small enough to allow treating the waves in the small amplitude approximation, is large enough to scatter the majority of cosmic rays many times over one pressure scale height (Figure 1). This justifies the frequent scattering limit we used in §2.3.1 to estimate the cosmic ray heating rate for the WIM (eqns 2.46 and 2.48) and show that adding it to the thermal equilibrium model of the WIM for Perseus Arm conditions produces a reasonably good fit to the observations (Figure 2). Although the heating rate coefficient is about a factor of 2 too small (eqn. 2.57), the height dependence - which follows from the height dependence of the magnetic field, gas density, and cosmic ray pressure - leads to a temperature vs height relation of the correct shape. We regard this, and matching the inferred size of the supplemental heating rate to within a factor of two - as confirmation that cosmic ray heating is a viable supplementary heat source for the

WIM. Cosmic ray heating also seems to be a thermally stable mechanism (2.3.2), at least under the assumptions we considered.

The results in this paper should be generally applicable to warm ionized gas in other galaxies. In cases where synchrotron emission is detected or other estimates of the cosmic ray and magnetic field energy densities are available, it should be possible to estimate the magnitude of cosmic ray heating. It is important that the gas be diffuse and that the ionization fraction be high; in weakly ionized clouds, for example, ion-neutral friction is so strong that the cosmic rays are not well coupled to the medium ([40]). And, as long as the cosmic rays are well scattered, their pressure gradient along the ambient magnetic field exerts a force which may be important in determining the scale height of the gas and in driving an outflow even when the thermal speed of the gas is well below what is needed for escape.

Acknowledgments

We are happy to acknowledge useful discussions with J.S. Gallagher, M. Haffner and R. Reynolds and support from NSF Grants PHY0821899 and AST0907837 to the University of Wisconsin. JW and SPO acknowledge support from NASA grant NNX12AG73G to UCSB.

Chapter 3

Interaction of Cosmic Rays Incident on Cold Clouds in Galactic Halos

3.1 Introduction

The interaction of CRs with ionized plasma has long been studied ([58]; [105]). CRs scatter off of magnetohydrodynamic (MHD) waves traveling in the plasma, and can indirectly heat or push on the plasma via these waves. A CR population with a strong enough density gradient can serve as a substantial source of thermal heating [117]. This may occur if there is a spatially-varying MHD wave speed,

such as may occur at the interface of a cold cloud in the plasma. In some cases the resulting CR wave heating can alter this interface, possibly affecting observable ionic abundances. The CR pressure gradient may also impart significant momentum to cold clouds, accelerating them to escape speeds. Our goal in this paper is to quantify these effects.

First, we present here a qualitative explanation of CR-plasma interaction. Consider a gas with density ρ_g threaded with a magnetic field of strength B. CRs travel through the gas in helical paths along magnetic field lines. The angle between an individual CR and the background magnetic field is called the pitch angle. A well-known instability called the streaming instability will give rise to MHD Alfvén waves if the bulk CR streaming velocity is greater than the local Alfvén wave speed $v_A = B/\sqrt{4\pi\rho_g}$. These waves then scatter the CRs in pitch angle until they are isotropic in the wave frame and the instability is shut off. Therefore in the absence of significant wave damping, CRs cannot stream faster than v_A. The CRs are said to be locked to the wave frame.

However, in the absence of an external source of waves, the CRs can stream *slower* than v_A, and in fact they will if the right conditions are met. Namely, if we have a region of plasma with a spatially-varying Alfvén speed, and there is a point where the Alfvén speed is a minimum, then in the steady-state all CRs upstream of this point will be forced to stream at this minimum v_A. If they were

to stream any faster, this would result in CRs streaming up their density gradient. This cannot happen without external waves to impart energy to the CRs. This bottleneck effect has important implications for CRs in galaxies that have cool clouds.

This paper examines the dynamic effects of CRs on cold clouds on two separate length scales - the large scale pushing of the cloud by the CR pressure gradient, and the much smaller scale thickening of the thermally conducting interface by CR wave heating. We use simple 1D simulations to study the first effect, and derive simple 1D steady-state models to study the second.

In §3.4.1 we introduce the evolution equations for CRs and for the thermal gas that will be relevant in our models. §3.3 describes the time-dependent simulations that simulate the pushing action, while §3.4 explains the steady-state models for the cloud interface thickened by CR heating.

3.2 Evolution Equations

3.2.1 CR Dynamics

In the fluid approximation, the bulk properties of the CR population are governed by the CR transport equation

$$\frac{\partial P_c}{\partial t} = (\gamma_c - 1)(\mathbf{u} + \mathbf{v_A}) \cdot \nabla P_c - \nabla \cdot \mathbf{F_c} + Q, \tag{3.1}$$

$$\mathbf{F_c} = \gamma_c P_c(\mathbf{u} + \mathbf{v_A}) - \mathbf{n}\kappa_c(\mathbf{n} \cdot \nabla P_c).$$

Here, P_c is the CR pressure, $\gamma_c = 4/3$ is the adiabatic index of the CRs (assumed to be relativistic), $\mathbf{u}$ and $\mathbf{v_A}$ are the local gas and Alfvén velocities respectively, and Q contains any CR sources and sinks. $\mathbf{F_c}$ represents a kind of CR energy flux, and the CR diffusion coefficient κ_c quantifies the movement of the CRs relative to the wave frame.

Consider a simple case where we have no sources or sinks, and no CR diffusion. That is, the CRs are locked to the wave frame everywhere. Let's also assume the bulk gas motion is negligible, so $u = 0$. Then (3.1) reduces to

$$\frac{\partial P_c}{\partial t} = -\mathbf{v_A} \cdot \nabla P_c - \gamma_c P_c \nabla \cdot \mathbf{v_A}. \tag{3.2}$$

If we further consider a one-dimensional, plane-symmetric system, this becomes

$$\frac{\partial P_c}{\partial t} = -v_A \frac{\mathrm{d}P_c}{\mathrm{d}z} - \gamma_c P_c \frac{\mathrm{d}v_A}{\mathrm{d}z}. \tag{3.3}$$

This has a steady-state solution:

$$\begin{aligned} 0 &= -v_A \frac{\mathrm{d}P_c}{\mathrm{d}z} - \gamma_c P_c \frac{\mathrm{d}v_A}{\mathrm{d}z} \\ \frac{\mathrm{d}P_c}{P_c} &= -\gamma_c \frac{\mathrm{d}v_A}{v_A} \\ P_c v_A^{\gamma_c} &= \text{constant}. \end{aligned} \tag{3.4}$$

We caution that this solution assumes that waves are present regardless of the spatial variation of P_c. If there is some external source of Alfvén waves that is

driving the CR population in one coherent direction through the plasma, then (3.4) is valid as written. Note that you can have CRs streaming up their own gradient in this case, but this is okay since the CRs are being driven by the external wave source.

If no such source exists, and only CR gradients produce Alfvén waves, then we must take care when using (3.4). This is because the direction of v_A must now always point down the CR gradient. As such P_c and v_A are not entirely independent. Note that (3.4) is perfectly fine so long as the solution is monotonic. Problems arise when there is a minimum in $|v_A| = B/\sqrt{4\pi\rho_g}$. Then the solution to (3.4) may have v_A pointing *up* the CR gradient, which is a contradiction.

What happens in this case? Suppose CRs are all moving together in one direction, say to the right, at a speed $|v_A|$ which varies in space. At some critical point in this flow there is a local minimum in $|v_A|$. As the CRs approach this minimum, their flow speed is decreasing, and so P_c is increasing as we move to the right. But this means the gradient of P_c now points to the left – the CR flow changes direction. Now there is an increasing flow speed to the left, so P_c at the critical point begins to fall. The equilibrium state is one where all of the CRs to the left of the critical point are moving to the right with equal speed, and equal P_c. Their speed is that of $|v_A|$ at the critical point and no Alfvén waves are present. To the right of the critical point, where $|v_A|$ is increasing towards the

right, there is a gradient in P_c, Alfvén waves are generated, and (3.4) holds. The situation is analogous to a traffic jam – drivers are stuck moving slower than they normally would because there are other cars ahead of it that are in the way.

Why exactly does (3.4) fail? The reason is that (3.4) assumes there are Alfvén waves present everywhere. For any monotonic solution this assumption holds. But for any solution where the gradient of P_c vanishes anywhere, this assumption is contradicted. The true solution is as described above. In the region upstream of the critical point, where P_c is flat, there simply are no Alfvén waves since there is no CR gradient to drive them. Note that although the CRs aren't flowing at the local value of $|v_A| = B/\sqrt{4\pi\rho_g}$, there is no diffusion. Diffusion describes drift of the CR population relative to the local wave frame. In the absence of any waves, "diffusion" has no real meaning.

3.2.2 Gas Dynamics

The typical evolution equations for a thermal gas are determined from mass, momentum, and energy conservation. In one dimension they are:

$$\frac{\partial \rho}{\partial t} + \frac{\partial (\rho u)}{\partial z} = 0 \tag{3.5}$$

$$\frac{\partial (\rho u)}{\partial t} + \frac{\partial}{\partial z}(\rho u^2 + P_g + P_c) = 0 \tag{3.6}$$

$$\frac{\partial E_g}{\partial t} + \frac{\partial}{\partial z}\left[(E_g + P_g)u - \kappa_g \frac{\partial T}{\partial z}\right] = -\rho\mathcal{L} - v_A \frac{\partial P_c}{\partial z} \tag{3.7}$$

In the above, ρ and u are the gas density and velocity, P_g and E_g are the gas thermal pressure and gas *total* energy density $E_g = P_g/(\gamma_g - 1) + 1/2\rho v^2$, and κ_g is the thermal conduction coefficient. P_c represents the CR pressure, and $\rho\mathcal{L}$ represents the net cooling function. Note that the effect of CRs is contained in a pressure gradient term in the momentum equation and a heating term in the energy equation. The heating rate due to CR pressure gradients is derived in [117].

Our time-dependent simulations use various simplifications of the above set of equations. Our simplest test cases do not evolve the gas at all. For computational reasons we ignore thermal conduction and radiative losses in our other simulations, $\kappa_g = 0$, $\rho\mathcal{L} = 0$ (see §3.3.4 for further details).

3.3 Hydrodynamic Simulation

We use a 1D version of the MHD simulation code ZEUS3D, adapted to include cosmic ray dynamics. Equation (3.1) is integrated in time using a finite-difference method on a fixed spatial grid. In this simulation we do not keep track of any momentum-dependent quantities – only P_c is evolved.

To account for the bottleneck effect discussed in §3.2.1, we must account for direction when calculating Alfvén velocities. The most straightforward way to do

this is to define the wave velocity in each grid cell to be

$$v_A = -\frac{B}{\sqrt{4\pi\rho_g}}\mathrm{sgn}\left(\frac{\mathrm{d}P_c}{\mathrm{d}z}\right). \tag{3.8}$$

But this lends itself to numerical instability – spatial oscillations will develop as CRs slosh back and forth between adjacent grid cells. We use a graceful solution introduced by [103], where we use a hyberbolic tangent as a smooth version of the sign function. That is, we define the wave velocity as

$$v_A = -\frac{B}{\sqrt{4\pi\rho_g}}\mathrm{Tanh}\left(\frac{\mathrm{d}P_c/\mathrm{d}z}{\epsilon}\right). \tag{3.9}$$

for some scale value ϵ. The simulation is then stable to numerical oscillations provided we use the accompanying time-step restriction

$$\Delta t \leq \Delta x^2 \epsilon / 2P_c|v| \tag{3.10}$$

at every local extremum of P_c. For $|v|$ we use a fixed value of 4.0×10^7 cm/s, which we expect to be greater than $|v_A|$ anywhere in the simulated region at any time.

3.3.1 Simple Case 1

We first test to see if the code will reach an equilibrium in the presence of a localized CR source. To do this we set up a slightly sloped gas density profile and a CR source one end. Reflecting boundary conditions are used at the location

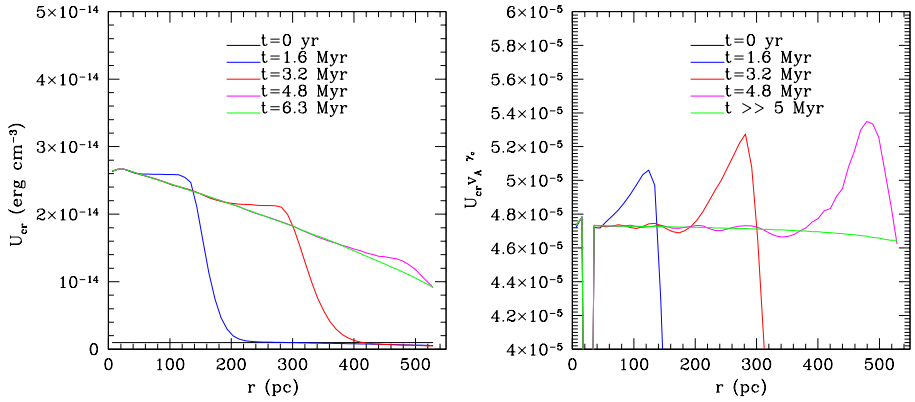

Figure 3.1: A simple test case. A CR source is placed at the far left. Left: CR energy density $U_{\rm cr}$. Right: The quantity $U_{cr}v_A^{\gamma_c}$. In equilibrium, this quantity is nearly constant, as expected from the solution (3.4).

of the CR source, and outflow conditions are used at the other boundary. We set a magnetic field of 3 μG throughout. There is no gravitational field and no wave damping. The gas temperature is set such that the initial configuration is in pressure equilibrium. The properties of the gas are held fixed – CR pressure feedback and wave heating are turned off. The only purpose of this simulation is ensure that we obtain an equilibrium in a region of strictly increasing $|v_A|$. This simulation very quickly reaches an equilibrium CR profile (see figure 3.1, left plot).

We can also see that in this case, which has no local minima in $|v_A|$ and hence no bottleneck effect, the solution (3.4) is correct. The right plot of figure 3.1 shows how, away from the CR source, $P_c v_A^{\gamma_c}$ is constant to within 2% once equilibrium is reached.

3.3.2 Simple Case 2

Let us now set up a system with a warm cloud, but not yet allow the gas to evolve. This will test if the code handles the bottleneck effect correctly. The density of the cloud edge is described by a Tanh function, as in [40], with a smoothing scale of 25 pc. The scale is chosen to be large to avoid a need for high spatial resolution for this test. The hot medium outside the cloud has temperature 10^6 K and density 10^{-3} cm^{-3}. The inside of the cloud is at 10^5 K with 10^{-2} cm^{-3}. We again have a 3 μG field throughout.

As before we use reflecting boundary conditions at the location of the CR source and outflow conditions at the other end. There is also a slight gradient in the gas density (with corresponding gradient in temperature to ensure equal gas pressure everywhere) so that the Alfvén speed is not spatially uniform at the boundary. We find that when the Alfvén speed is uniform, the CR profile becomes flat, and when the CR profile is flat at the boundary, the smoothing scheme (3.9) prevents CRs from leaving the domain.

This effect can be seen in figures 3.2 and 3.3. Figure 3.2 shows the CR profile for the simulation with the slight gas density gradient plus cloud. The Alfvén speed is a minimum at the center of the cloud, so there is a bottleneck there. The CR profile quickly reaches an equilibrium. Figure 3.3 shows the CR profile for the same simulation without the slight gas density gradient. The CR profile reaches

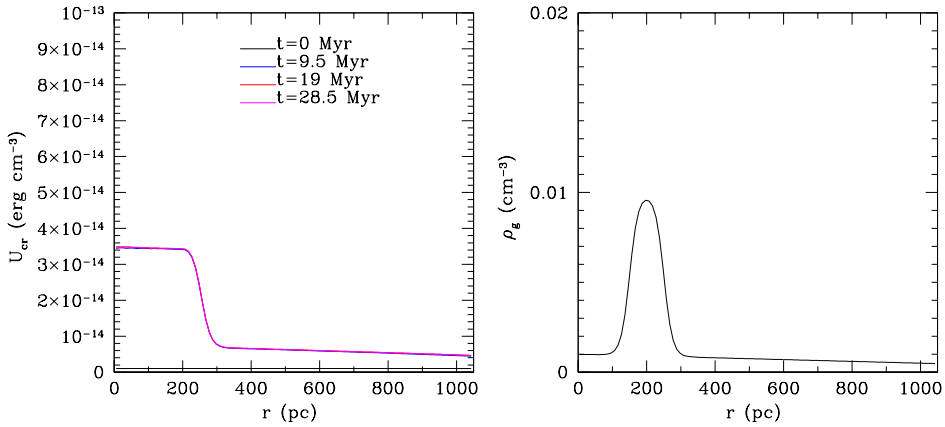

Figure 3.2: A simple test case. A CR source is placed at the far left, with a warm cloud a short distance away.

a state similar to that in 3.2, but since CRs cannot exit through the boundary they slowly build up in the region behind the cloud.

3.3.3 Simple Case 3

For the next simple test we use the same cloud setup as in test 2, but with a "cool" cloud temperature and density of 10^4 K and 10^{-1} cm^{-3}. Additionally, we turn on the effects of CR pressure and wave heating on the gas. Other effects such as thermal conduction and cooling mechanisms are not considered here. The result is a rapid ($\sim$ 100 Myr) destruction of the cloud followed by a slow deterioration of what remains afterward. This is shown in the two density plots in figure 3.4.

This simulation also exhibits some interesting properties. Figure 3.5 shows the different pressures at different times. The dotted lines at the bottom display

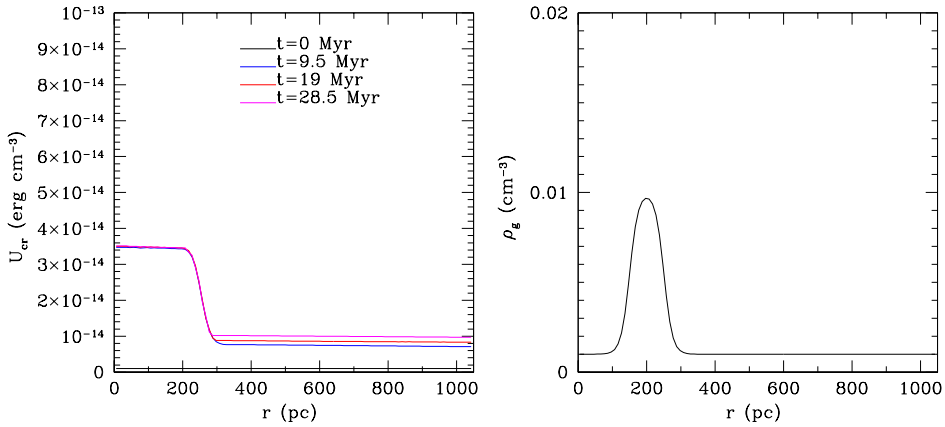

Figure 3.3: A simple test case. The setup is the same as figure 3.2, but the gas density is flat at the boundary.

the CR pressure, the dashed lines above them are the gas pressure, and the solid lines are the total (CR + gas) pressure. We can see a sound wave propagating outward – this is created by the impact of the first source-produced CRs on the rear edge of the cloud. This wave initially caused some issues since, despite the outflow conditions at the outer boundary, it would bounce back and interfere with the simulation. To avoid this we simply place the outer boundary far away from the cloud, using a non-uniform spatial grid. The test case shown here uses a grid that spans about 40 kpc, with 200 cells. The width of each cell is larger than the one preceding it by a constant factor, in this case 1.022. This results in grid widths of about 12 pc on the left end, increasing to 900 pc at the right end.

There is also a small feature leading the sound wave. This is a "streaming front," which traces the position of the first source-emitted CRs as they stream

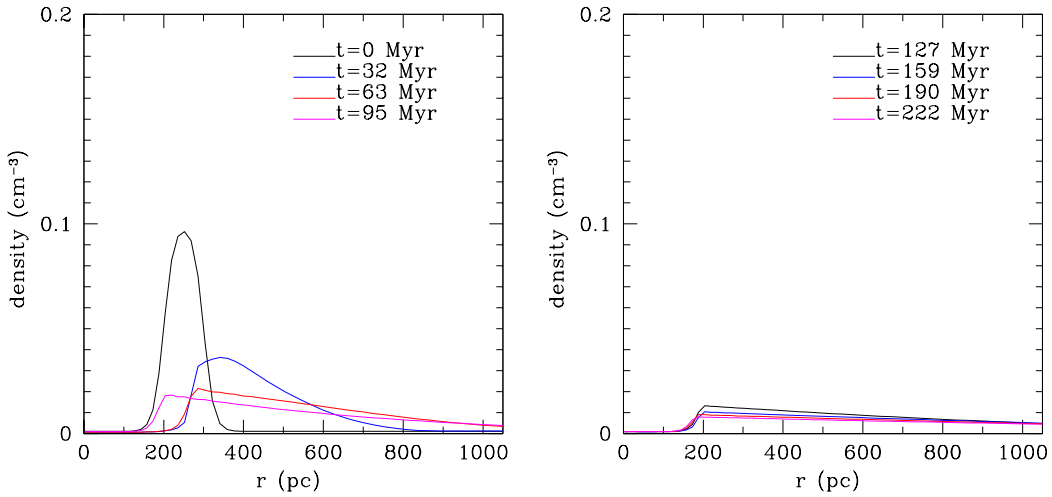

Figure 3.4: Evolution of the gas density from an initial cool cloud due to the presence of a CR source.

outward. Whether this feature is resolved well or not depends on the smoothing scale ϵ in equation (3.9). We note that for this simple test we use very modest resolutions to reduce computation time. Because of this, neither the streaming front nor the sound wave front are well-resolved, but these are not the focus of this test.

We can investigate the relative effects of CR pressure and wave heating by turning each off selectively. What we find is pretty straightforward – if we turn off wave heating but leave in the effect of CR pressure on the gas, the cloud is slowly pushed on, but not significantly distorted beyond a slight stretching. If we turn on wave heating but remove the effect of CR pressure on the gas, the cloud is destroyed, but doesn't move from its initial position (see figure 3.6).

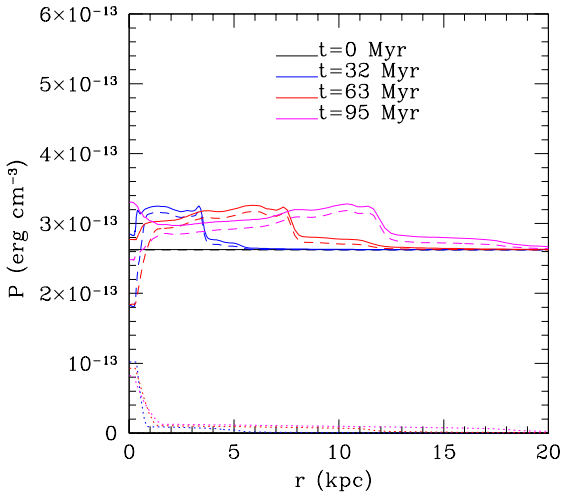

Figure 3.5: Evolution of the CR pressure (dotted lines), gas pressure (dashed lines), and total pressure (solid lines). A sound wave propagates outward, led by the streaming CRs.

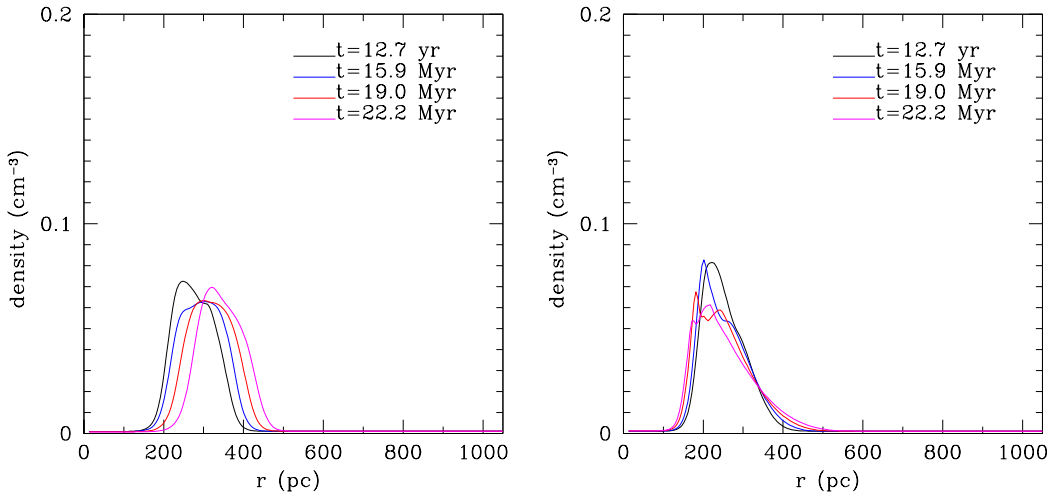

Figure 3.6: Evolution of the gas density with different components turned off. The left plot has no wave heating, whereas the right plot has no CR pressure.

3.3.4 Imparting Momentum to Cool Clouds

Ideally we would incorporate radiative cooling and thermal conduction into these 1D simulations. But the spatial resolution required to resolve relevant length scales such as the Field length is computationally very expensive. We therefore continue our analysis under the assumption that radiative cooling removes nearly all the thermal energy the gas may gain from CR heating. The effect of the CRs can then be broken down into two separate arenas: the CR pressure gradient imparts momentum to the cool cloud as a whole, while wave heating heats and thickens the cloud interface. The former effect can be studied with our simulations above so long as we turn off CR heating (the energy loss of CRs from this effect of course remains active). The latter effect can be studied in steady-state approximations, as we describe in section 3.4.

To consider again the time-dependent simulation without CR heating, see figure 3.7. This is the same setup as above in figure 3.6 but with the cloud positioned further away from the source. This is to minimize the effect of our 1D plane symmetry which we discuss shortly.

The overall effect of the CR pressure gradient is best seen in the right plot of figure 3.7, which shows the total pressure (solid lines), gas pressure (dashed lines), and CR pressure (dotted lines) at different times in the simulation. As the CRs first build up at the rear edge of the cold cloud, the resulting total pressure

gradient pushes the cloud to the right. The cloud (as well as the hot material to its left) is stretched as it moves, gradually lowering the density and thermal pressure to the left of the CR bottleneck until total pressure equilibrium is re-established[1].

The large-scale picture we get is this: CRs build up at the rear edge of the cloud, inducing a total pressure gradient, and filling up the region of space from the CR source to the cloud with CRs. The column of gas extending from the CR source to the cloud is then momentarily over-pressurized. The cloud is pushed away from the CR source, with the material inside the column dropping in density and pressure as the volume it occupies increases. We can then describe the large scale effect of the CRs on the cloud in two parts. The CRs have stretched the cloud, reducing the density inside. They have also imparted momentum to the cloud, accelerating it to some maximum velocity (figure 3.8).

We note that the maximum velocity achieved here ($\sim$ 10 km/s) is small compared to observed velocities of clouds in the Milky Way. But the CR source in this simulation is also weak - P_{CR} in the hot region to the right of the cloud is much less than P_{th}, whereas in the Milky Way halo they are observed to be in rough equipartition. Future simulations will determine of CRs can accelerate cold clouds to the high velocities that are observed.

[1]In 1D, this rarefaction continues as the cloud progresses, eventually inverting the total pressure gradient and pulling back on the cloud like a spring. We do not expect this behavior in higher dimensions, as hot gas is available to flow in from directions perpendicular to the CR flow, preventing the pressure leftward of the cloud from dropping further. We therefore do not do not consider the results of these simulations to be robust at late times.

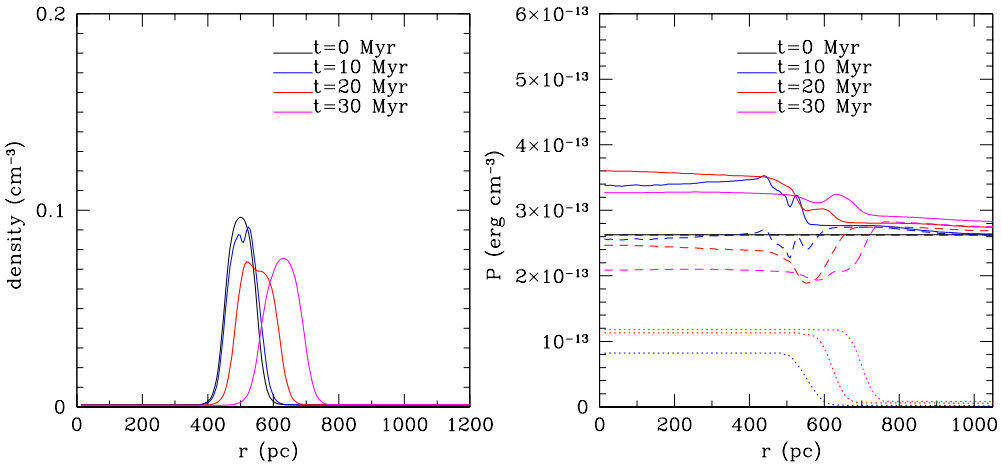

Figure 3.7: Evolution of the gas density and different pressure components in the efficient cooling limit (the CR heating term in the gas energy equation is turned off). The cloud reacts to the sudden push from the CRs by stretching out and lowering its density and thermal pressure.

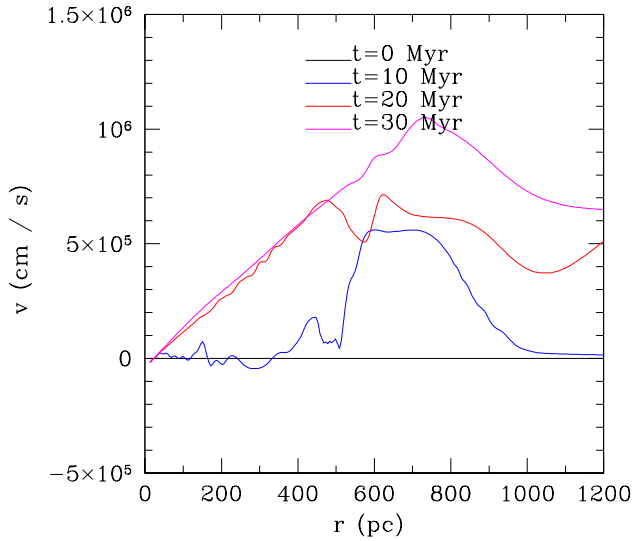

Figure 3.8: Evolution of the gas velocity in the efficient cooling limit (the CR heating term in the gas energy equation is turned off). The cloud reaches a maximum speed of about 10 km/s in this simulation.

3.4 Steady State 1D Thermal Fronts

Having examined the large-scale effects of a CR pressure gradient, we now zoom in on the interface between the cold and hot gas phases to describe the small-scale effect of CR wave heating. We derive a 1D analytic model of such an interface in the steady state, where radiative losses are balanced by CR heating and thermal conduction.

Our main goal in this section is to understand the effect of CRs on the interfaces of cold molecular clouds embedded in the hot medium of a galaxy. Inside these clouds we expect CRs to be uncoupled from the gas, either because of strong ion-neutral wave damping or, in the bottleneck situation we are considering, because CRs stream slowly and the streaming instability is not activated. We can therefore focus on the temperature profile at the rear edge of the cloud only, where the CRs exit and recouple to the gas.

Our simple model then consists of a 1D plane parallel symmetric profile of gas. The cold region, representing the inside of the cloud, is on the left, and the hot region outside of the cloud is on the right. A thermally conducting interface lies between these two regions, and we imagine a CR source on the far left. As long as the gradient in gas density is monotonic, we can use equation (3.1) to determine CR pressure (again, in the limit of negligible CR diffusion).

3.4.1 CR and Gas Equations

Since we are only considering the structure of the cloud interface our v_A profile will be monotonic. We can therefore use equation (3.1) for our analysis here, although we remove the assumption that u is negligible compared to v_A.

$$P_c(u + v_A)^{\gamma_c} = \text{constant}. \tag{3.11}$$

To model the gas we use equations (3.5) - (3.7) with the partial time derivatives set to zero to emulate a steady state.

$$\frac{\partial(\rho u)}{\partial z} = 0 \tag{3.12}$$

$$\frac{\partial}{\partial z}(\rho u^2 + P_g + P_c) = 0 \tag{3.13}$$

$$\frac{\partial}{\partial z}\left[(E_g + P_g)u - \kappa_g \frac{\partial T}{\partial z}\right] = -\rho\mathcal{L} - v_A \frac{\partial P_c}{\partial z} \tag{3.14}$$

In the steady state we can quickly identify some useful constants of integration:

$$J = \rho u = \text{constant} \tag{3.15}$$

$$M = P_g + P_c + \rho u^2 = \text{constant} \tag{3.16}$$

The mass flux J and total pressure M will be used to characterize the simple 1D front solutions discussed in this paper.

Unlike our time-dependent ZEUS simulations, we now include the thermal conduction and radiative loss terms that appear in equation (3.14). We use a combination of standard Spitzer conductivity and conductivity of a neutral medium

for the thermal conduction coefficient κ_g. In cgs units,

$$\kappa_g(T) = 5.6 \times 10^{-7} T^{2.5} + 2.5 \times 10^3 \sqrt{T}. \tag{3.17}$$

To calculate the net cooling $\rho\mathcal{L}$ we assume a heating rate proportional to the gas density Γn with $\Gamma = 1.2 \times 10^{-24}$ erg s^{-1} and a radiative cooling rate of the form $\Lambda(T)n^2$. We use an artificially modified version of the radiative cooling function $\Lambda(T)$ determined from assuming collisional ionization equilibrium (CIE) and solar metallicity. We modify this cooling function above $T \sim 7 \times 10^5$ K such that the high temperature equilibrium at $T \sim 1 \times 10^6$ K (for $M = 10000\ k_B$ and $J = 0$) is formally stable instead of unstable (see figure 3.9). We describe the motivation and justification for this choice in §3.4.3.

3.4.2 Efficient Cooling Limit

Consider the limiting case where cooling is extremely efficient. In this limit the conduction front is infinitesimally thin, the mass flux J vanishes, and CR heating can be neglected. The solution consists of just the two stable cooling equilibria side by side, separated by the infinitesimally thin conduction front. Examining such a regime allows us to isolate the dynamic effect of a CR source, ignoring any possible contributions from heating. This does not give us any information about the structure of the front itself, but serves as a useful check of the time-dependent results in §3.3.

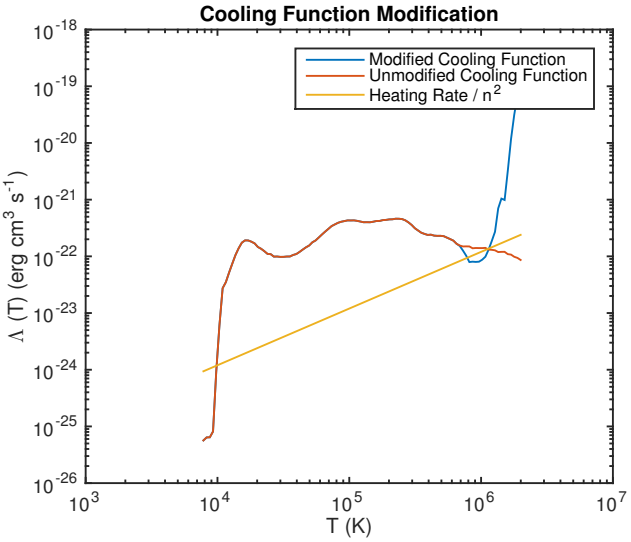

Figure 3.9: Modification of the CIE cooling function $\Lambda(T)$. This modified cooling function artificially makes the hot phase of the gas formally stable to radiative cooling. The heating rate for $M = 10000\ k_b$ and $J = 0$ is also plotted to show the location of the equilibria.

For a given total pressure M, we can then parametrize our solutions by X_{CR}, defined as the ratio of CR pressure to thermal pressure in the cold region. We can then find the solutions by simply demanding pressure balance on either side of the front.

$$M = P_{c,1} + n_1 k_B T_1 = P_{c,2} + n_2 k_B T_2 \tag{3.18}$$

To solve this we substitute $P_{c,1} = X_{CR} n_1 k_B T_1$ and $P_{c,2} = P_{c,1}(n_2/n_1)^{\gamma_c/2}$ (from (3.11) with $u \approx 0$). We end up with

$$n_1 k_B T_1 = \frac{M}{1 + X_{CR}} \tag{3.19}$$

$$n_2 k_B T_2 = M \left[1 - \frac{X_{CR}}{1 + X_{CR}} \left(\frac{n_2}{n_1} \right)^{\gamma_c/2} \right] \tag{3.20}$$

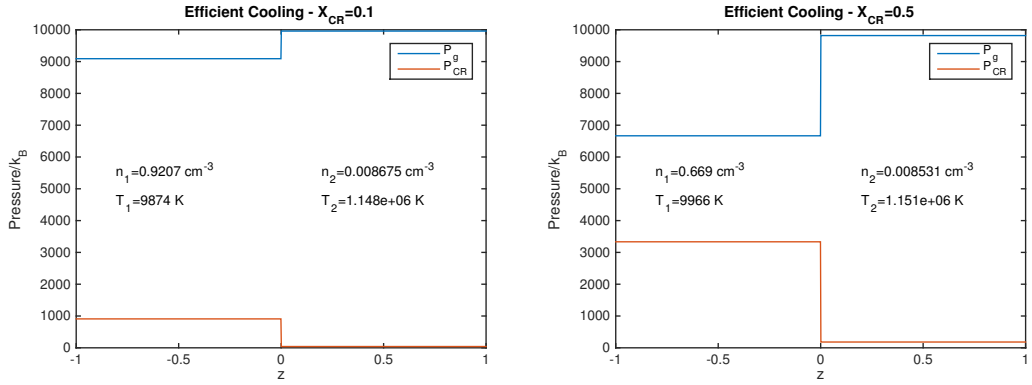

Figure 3.10: Solutions for gas pressure P_g and CR pressure P_{CR} in the simplified, efficient cooling regime. Equilibrium values in the cold (left) and hot (right) regions are shown. The main effect of an increased CR source is to reduce the density in the cold region.

These equations relate n and T in each region. We then numerically solve for these by demanding $\rho\mathcal{L}(n,T) = 0$ in both regions. Example plots of these solutions for $M = 10000k_B$ are shown in figure 3.10.

As we vary X_{CR} in these solutions we find that the equilibrium in the hot region is nearly unchanged. This is expected since P_{CR} should be very low in the hot region unless the CR source is unrealistically strong. Similarly the temperature in the cold region does not change much. We attribute this to the steepness of the cooling function $\Lambda(T)$ in this temperature range. The main effect seen on the gas due to CRs in these simplified solutions is a reduction in the density of the cold region with increased CR source strength.

3.4.3 General 1D Front

To include the effects of conduction and CR heating we must numerically solve equation (3.14) in the steady state. We do this by recasting everything in terms of the gas density ρ. We have, from equation (3.11)

$$P_c = P_{c0}\left(\frac{u_0 + v_{A0}}{u + v_A}\right)^{\gamma_c} = P_c(\rho) \tag{3.21}$$

The gas quantities can then also be rewritten using the integration constants (3.15) and (3.16)

$$T(\rho) = \frac{\bar{m}}{k_B}\left[\frac{M}{\rho} - \frac{J^2}{\rho^2} - \frac{P_c(\rho)}{\rho}\right] \tag{3.22}$$

$$(E_g + P_g)u = \frac{\gamma_g}{\gamma_g - 1}\frac{J(M - P_c(\rho))}{\rho} + \left(\frac{1}{2} - \frac{\gamma_g}{\gamma_g - 1}\right)\frac{J^3}{\rho^3} \tag{3.23}$$

Here, P_{c0} and ρ_0 are scale values of the CR pressure and gas density, with $u_0 = J/\rho_0$ and $v_{A0} = B/\sqrt{4\pi\rho_0}$ the gas and Alfvén speeds at this scale density. $\bar{m}$ is the mean molecular weight of the gas.

With these replacements, equation (3.14) reduces to a second order ODE in one variable which can be solved numerically for $\rho(x)$ and subsequently $T(x)$. This process includes finding the correct value of the mass flux J for which a solution exists. However, we found that for a fixed total pressure the equations allowed for a range of solutions with different values of J. There appears to be a degeneracy in the solutions of $T(x)$ where thermal pressure in the hot phase is traded off for ram pressure, and solutions exist for a range of values of J. By adopting the

modified cooling function alluded to in §3.4.1, which artificially makes the hot equilibrium thermally stable, the degeneracy is eliminated and unique solutions with unique eigenvalues J are found.

Note that, since J is consistently determined from the total amount of heating or cooling throughout the front, this modification in the cooling function impacts the resulting values of J in our numerical solutions. We therefore caution that the actual values of J here are not physical and we do not ascribe any importance to them. However, since all values of J we obtain in the solutions presented here are small (u is never greater than 30% of the sound speed) we maintain faith that the front solutions themselves are robust.

Figure 3.11 shows the gas and CR pressure profiles for two such solutions using a total pressure of $M = 10000 k_b$. Comparing with figure 3.10 we see that the equilibrium states of the gas are very well approximated in the simplified treatment. The full treatment however has the advantage of providing a temperature profile (figure 3.12) that we can use to calculate theoretical ion abundances and line ratios to compare with observation.

Using ionization fractions $X_i(T)$ from [49] and relative abundances A_X from [4] we can calculate the column densities of ions defined by $N_X = A_X \int X_i(T) n \mathrm{d}x$, where n is the gas density and we integrate across the front. To avoid dependence on the length of integration we use, we limit our integral to temperatures below

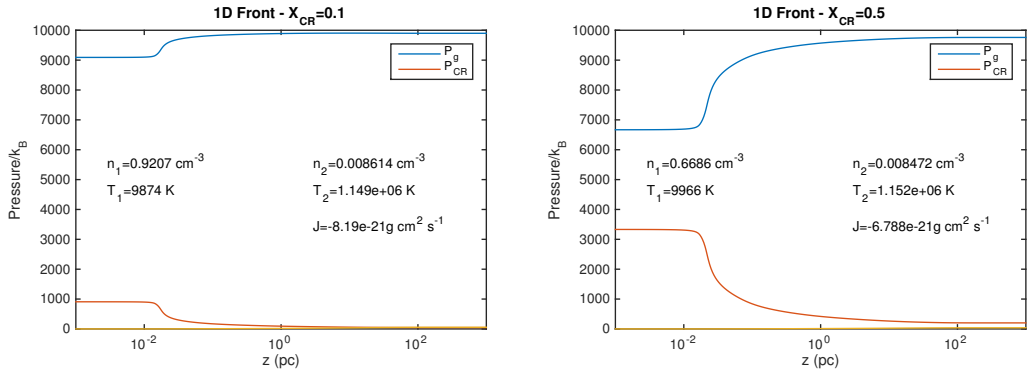

Figure 3.11: Solutions for gas pressure P_g and CR pressure P_{CR} in the full calculation. Density and temperature of the left (cold) and right (hot) equilibrium states and mass flux eigenvalues J are also shown.

some critical temperature $T_{\rm crit}$, for which we choose the temperature where the OVI ionization fraction drops below $\sim$0.01, or $T_{\rm crit} = 7 \times 10^5\ K$.

We calculate column densities for CIV, OVI, and SIV for each solution, covering a variety of values of M and X_{CR}. The resulting ratios for some of these are shown in figure 3.13 alongside line ratio data from observations of high velocity clods (HVCs) in the Milky Way from [110].

3.5 Conclusion

We have discussed the possible consequences of a bottleneck effect that occurs when a population of CRs undergoing streaming is incident upon a cold cloud embedded in a hot galactic halo. Although strong wave damping in the interior of these clouds prevents coupling between the CRs and the cold gas, as CRs exit

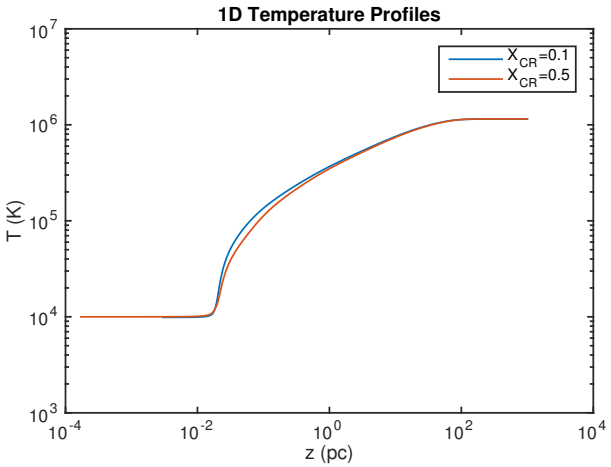

Figure 3.12: Temperature profiles for the two solutions shown in figure 3.11, translated in the x-axis so the positions of the fronts match. The profile with the stronger CR source is slightly wider.

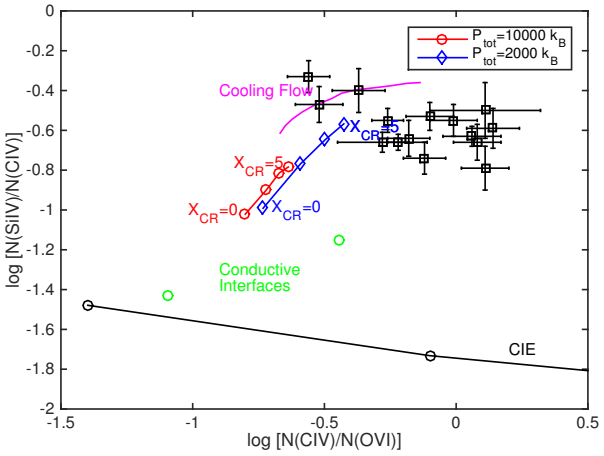

Figure 3.13: Line ratios for the 1D plane parallel models with thermal conduction and CR heating. Also shown are a few other interface models for comparison.

the cloud they will recouple, and at some point there will be a minimum CR drift speed. This point will serve as a bottleneck for all CRs traveling through the cloud and cause a CR pressure gradient to build up.

The consequence of this pressure gradient can be split into two effects. On the largest scale the gradient itself pushes on the cloud material, rarefying the material inside and accelerating it to potentially high velocities for a strong CR source. We described this effect with 1D plane symmetric, time-dependent simulations using the ZEUS hydrodynamic code.

On much smaller scales, CR wave heating thickens the thermal interface between the cold gas inside the cloud and hot gas outside. This thickening has a measurable affect on ionic abundances in the interface - our models show that conductive interfaces that receive significant wave heating from a strong CR source more closely match observed ionic abundance ratios than conductive interfaces with no CR heating.

We again note that all the simulations and steady state models introduced here were performed in one dimension only. The magnetic field structure is not considered, and wave damping is also not accounted for. Full 3D simulations that include the effects of different magnetic field orientations and wave damping mechanisms are necessary to verify the claims made here.

Chapter 4

Cosmic Ray Transport: Streaming vs. Diffusion

Much effort has been made over the past few years to accurately simulate individual galaxies with the goal of determining the viability of CR driven winds [53, 97, 98]. CRs are appealing as drivers of galactic winds, since they do not suffer radiative losses that a thermally driven wind would have, and so can potentially accelerate gas over much longer distances. However, CR transport relative to the background medium is generally treated with a pure diffusion term in these simulations, often with a constant diffusion coefficient. Such a treatment ignores much of the physics of CR transport, and may dangerously simplify the dynamics in a way that alters the simulation results. Our goal here is to qualitatively

compare simulations which use pure diffusion with those that instead use pure streaming, to demonstrate how the differing dynamics affect the ambient medium in different ways.

4.1 Methodology

4.1.1 Equations

The evolution equations for a plasma plus cosmic rays are basically a modified set of standard fluid equations, with an extra fluid equation for the cosmic rays. They are:

$$\frac{\partial \rho}{\partial t} + \nabla \cdot (\rho \mathbf{u}) = 0 \tag{4.1}$$

$$\frac{\partial (\rho \mathbf{u})}{\partial t} + \nabla \cdot (\rho \mathbf{u}\mathbf{u}) = -\nabla P_g - \nabla P_c - \rho \nabla \Phi \tag{4.2}$$

$$\frac{\partial E_g}{\partial t} + \nabla \cdot (E_g \mathbf{u}) = -P_g \nabla \cdot \mathbf{u} - \mathbf{v}_A \cdot \nabla P_c - n_e^2 \Lambda(T) \tag{4.3}$$

$$\frac{\partial E_c}{\partial t} + \nabla \cdot [E_c(\mathbf{u} + \mathbf{v_s})] = -P_c \nabla \cdot (\mathbf{u} + \mathbf{v_s}) + \mathbf{v}_A \cdot \nabla P_c + \nabla \cdot (\kappa \nabla P_c) \tag{4.4}$$

Equation (4.1) represents mass conservation as usual. Equation (4.2) is a standard force equation (including gravity) with an extra term included for the cosmic ray pressure gradient. Equation (4.3) describes the evolution of the gas thermal energy, with usual adiabatic loss and radiative cooling terms, but also an additional wave heating term from the cosmic rays. Equation (4.4) is the evolution equation

for a population of CRs in the fluid approximation, streaming at velocity $\mathbf{v_s}$ relative to the gas, with a possible diffusion coefficient κ included. A more complete treatment would use an equation for the distribution function of CRs, $f(\mathbf{x}, \mathbf{p}, t)$, with a momentum dependent streaming speed $\mathbf{v_s}(p)$, but this simplified version will serve for our purposes.

4.1.2 Streaming vs. Diffusion

The basis for the streaming term introduced in (4.4) is derived in [105] and relies on the existence of the streaming instability. A population of CRs moving at bulk speed v_s with respect to the ambient medium, along the background magnetic field, will generate magnetohydrodynamic (MHD) Alfvén waves if v_s is greater than the local Alfvén speed v_A. CRs will give up energy to these waves, inducing a wave growth rate that depends explicitly on v_s. Equilibrium is determined by equating this growth rate with whatever wave damping rates are imposed by the background plasma. Therefore, if these damping mechanisms are linear, demanding a steady state for the waves uniquely determines the bulk speed v_s of the CRs at every point. This is the self-confinement picture, where the transport of CRs is governed by scattering off of self-generated Alfvén waves.

We can examine the self-confinement picture in more rigorous detail. Following [58, 105], we start with a collisionless Vlasov equation for the cosmic ray distri-

bution function f. Shifting to the frame of Alfvén waves and using the Lorentz force for the external forces, the equation can be greatly simplified if we assume f to be nearly isotropic,

$$f(\mathbf{x}, \mathbf{p}, t) \approx f_0(\mathbf{x}, p, t) + f_1(\mathbf{x}, p, \mu, t), \tag{4.5}$$

where μ is the cosine of the particle's pitch angle, the angle its trajectory makes with the background magnetic field. This assumption is valid in the limit of strong pitch angle scattering off of magnetic field fluctuations, which holds in the self-confinement regime so long as the wave damping is not too effective. The evolution of f_0 is then governed by the rate of this scattering ν.

$$\frac{\partial f_0}{\partial t}_{\text{sc}} = \nabla \cdot \left(v^2 \Big\langle \frac{1-\mu^2}{\nu(\mu, p)} \Big\rangle (\mathbf{n} \cdot \nabla f_0) \mathbf{n} \right) \tag{4.6}$$

The angle brackets above indicate an average over pitch angle and $\mathbf{n}$ indicates a unit vector in the direction of the local magnetic field. For a given wave damping rate Γ_{damp}, and assuming the streaming instability is the only source of waves, this average can be computed, and the result is

$$\frac{\partial f_0}{\partial t}_{\text{sc}} = \frac{1}{p^3} \nabla \cdot \left(\frac{\Gamma_{\text{damp}} B_0^2}{4\pi^3 m \Omega_0 v_A} \frac{(\mathbf{n} \cdot \nabla f_0)\mathbf{n}}{|\mathbf{n} \cdot \nabla f_0|} \right). \tag{4.7}$$

This term encompasses the deviation of CRs from the wave frame due to external wave damping. Note that the "flux" of this term is always pointing parallel to the magnetic field, in the direction opposite the CR gradient.

We might question now how best to characterize this term in the CR transport equation. Equation (4.7) resembles a diffusion term – indeed, it comes from the calculation of a pitch angle diffusion term. However, the "diffusive" flux, the term inside the parentheses, is independent of $|\nabla f_0|$[1]. In this respect it loses nearly all of the properties that define a diffusion term. We could alternatively classify it as a streaming term with energy-dependent streaming speed $\mathbf{v_s}(p)$. But it behaves unlike simple advection in that the direction of the velocity field $\mathbf{v_s}$ depends on the direction of the CR gradient ∇f_0. Still, the pitch angle diffusion term is most accurately described by streaming, and the distinction is important.

A true diffusion term contains two spatial derivatives. This is why any diffusive medium will smooth out in density over time – the shape of any initial density profiles will become flatter, and it will do this at all points evenly. In contrast, an advection term only has one spatial derivative, and so profile shapes are maintained (except for changes due to divergence of the velocity field). What we have isn't quite either of these. Because the direction of the velocity field depends on the direction of the density gradient, the profile will flatten out at extrema. However, the profile shape will be preserved everywhere else. And even

[1]Note that this is not generally true even in the self-confinement regime - there are some damping mechanisms, such as non-linear Landau damping, where the damping rate itself will have some dependence on $|\nabla f_0|$. However it is still true that this term will in general not be a constant diffusion term. The remainder of this discussion is restricted to the case where $\Gamma_{\rm damp}$ is independent of f_0.

at the extrema, the nature of the flattening is independent of the magnitude of the gradient, and cannot be correctly described as diffusive.

4.1.3 Simulation Setups

To carefully demonstrate the dynamical difference between streaming and diffusion, we perform a number of simulations using the SPH code Gadget-2 modified to include CR streaming (see [107]). We first simulate a very simple environment, a uniform periodic slab of background gas. As in [107] Appendix B we superimpose onto this background a plane-parallel gaussian initial CR pressure distribution. Gravity is turned off, but hydrodynamics are turned on, so the CR pressure will affect the background gas. With this setup we evolve the system once using CR diffusion with a constant diffusion coefficient, and once using CR streaming at the Alfvén speed v_A (i.e. the weak wave damping limit). The results of these simulations are discussed in section 4.2.1.

Second, we simulate a long vertical cut through a gravitationally stratified disk (also plane-parallel). We steadily inject CRs into the central regions to emulate stellar feedback. Again we compare results of CRs evolving with constant diffusion coefficient to those streaming at the Alfvén speed (4.2.2).

Lastly we have a suite of isolated, spherically collapsing galaxy formation simulations. We simulate galaxies with halo masses of 10^9 and 10^{10} $M_\odot$, with

and without CR injection from star formation. For simulations with CRs, we run separately cases with streaming, with diffusion, and with neither (4.2.3).

In all of the simulations described here, the streaming time constraint is the same is described in [107], with the same parameters. Namely,

$$\Delta t < \epsilon \frac{1}{\lambda c_s} \left(\frac{m}{\rho} \right)^{1/3} \tag{4.8}$$

with $\epsilon = 0.004$ and $\lambda = 1$.

4.2 Simulation Results

4.2.1 Simple Flux Tube Models

We compare the dynamics of CRs undergoing diffusion and streaming for two different initial CR profiles in the simple flux tubes. The background gas density in these simulations is set to $n = 0.01$ cm^{-3}. The temperature and magnetic field are chosen such that the sound speed c_s and the Alfvén speed v_A are both 100 km/s at this density. For simulations evolving with diffusion we use a constant diffusion coefficient of $\kappa = 3 \times 10^{28}$ cm^2 s^{-1}. The domain is a long periodic box 100 kpc long, with a 10kpc by 10 kpc cross section[2]. The lowest resolution runs are filled with 10^4 SPH particles with a roughly even inter-particle spacing of 1 kpc - other runs have resolution increased as necessary.

[2] An exception is the sharp-peaked initial distribution with streaming. The required resolution here was very high, so we only simulate a 10 kpc long box.

The first setup has a plane-parallel "broad" gaussian of width 1 kpc for the initial CR pressure profile with $X_{CR} \equiv P_{CR}/P_{th} = 1$ at the central maximum. This length scale L is chosen such that the initial diffusive flux $\kappa \nabla P_c \sim \kappa P_c/L$ in the diffusion-only runs is roughly the same as the streaming flux $v_A P_c$ in the streaming-only runs.

The results of this profile evolving under diffusion are shown in figure 4.1, top left. The CR pressure profile essentially just widens with time while remaining nearly a gaussian distribution. Small density perturbations are excited initially by the CR pressure gradient - these then travel outward at the sound speed.

In contrast, the CR profile flattens from the center out for the constant streaming speed case (figure 4.1 top right). In this case CR wave heating is dumping a significant amount of energy into the gas wherever the CR pressure gradient is strong. The result is a larger density perturbation compared to the diffusive case.

This difference is magnified when we start with a sharper CR profile. A second setup uses an initial gaussian CR pressure profile of width 0.2 kpc and $X_{CR} = 5$ at the central maximum, such that the total initial CR energy is the same as the first setup. The diffusive case is nearly the same as before (figure 4.1 bottom left): the CR pressure profile evolves almost exactly as a gaussian, so starting with a sharper peak amounts to merely a slight offset in time. However, because the CR pressure gradients are much stronger here, the streaming case is vastly different

(figure 4.1 bottom right). Most of the energy is dumped into the gas on a very short time scale (note the different time stamps in this plot) resulting in a huge spike in density.

We can also see differences if we start with no CRs and steadily inject CR energy in the center. Figure 4.2 shows the density and CR pressure profiles for this case. Again, the streaming profile is characterized by a flat expanding center, while the diffusing profile maintains a gradient through most of the volume. This results in an evacuation of gas from the central regions that is wider than in the streaming case. Also, as in the other setups, the outgoing density peaks are higher in the streaming run because of the additional transfer of energy through wave heating that is absent in the diffusion run.

4.2.2 Gravitationally Stratified Disk

To simulate a stratified disk we use a 10 kpc by 10 kpc periodic box in the directions parallel to the disk, with the third direction unbounded. We impose a fixed gravitational potential of the kind described in [31]

$$\nabla\phi \propto \tanh\left(\frac{z}{b}\right) \tag{4.9}$$

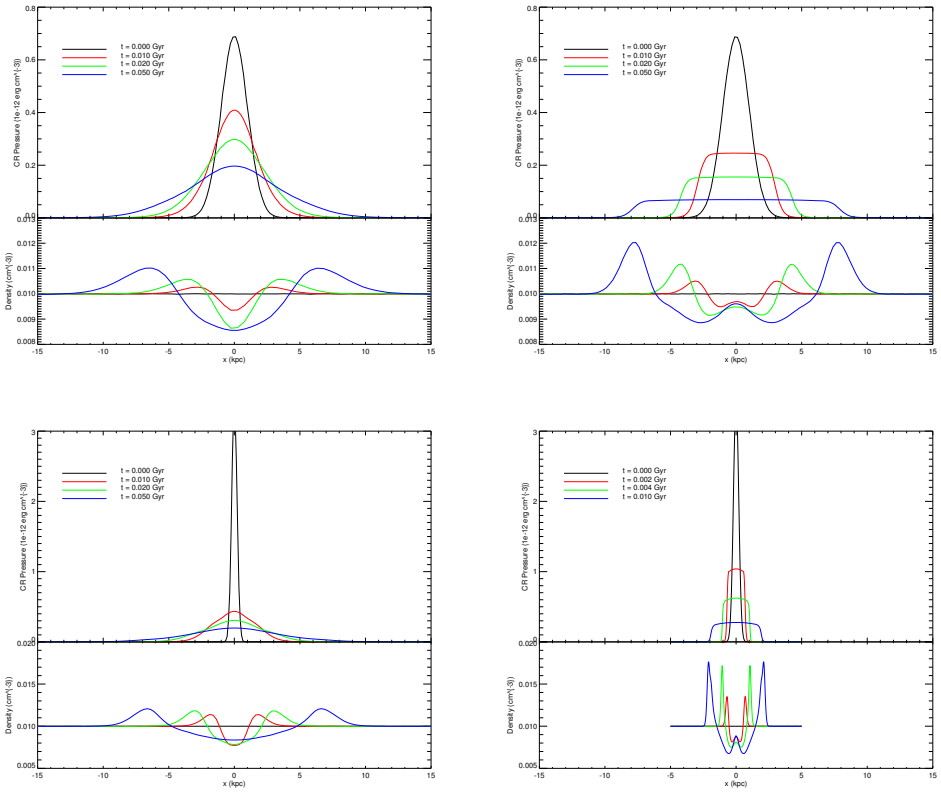

Figure 4.1: CR pressure and density profiles for the homogeneous background diffusion (left) and streaming (right) simulations, starting with broad (top) and narrow (bottom) initial CR peaks.

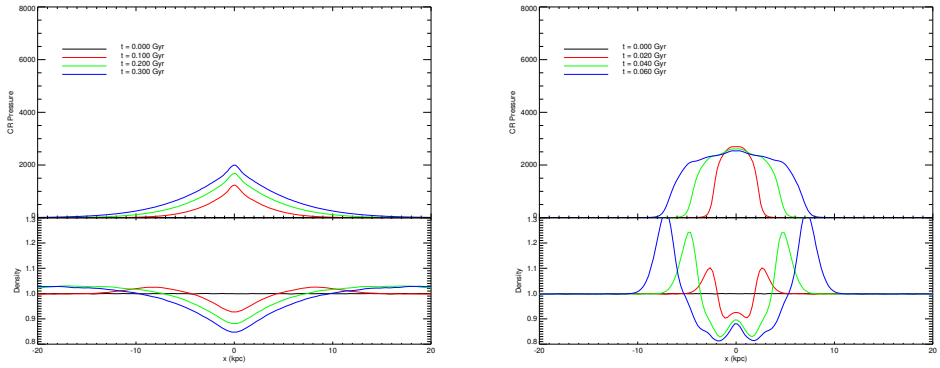

Figure 4.2: Steady central injection of CR energy evolving with a constant diffusion coefficient (left) and constant streaming speed (right).

where the scale height b is a free parameter that we choose to be 1 kpc[3]. This potential is intended to mimic that of a stellar disk. The initial background gas is chosen to be isothermal and in hydrostatic equilibrium

$$\rho(z) = \frac{\Sigma_g}{2b}\mathrm{sech}^2\left(\frac{z}{b}\right). \tag{4.10}$$

We are free to choose the density at the center of the disk by adjusting the parameter Σ_g, and then ensure hydrostatic equilibrium by subsequently adjusting the normalization of the gravitational potential. We choose a central density of $n_0 = 0.01$ cm^{-3} and a temperature $T \approx 5 \times 10^5$ K (giving sound speed $c_s = 100$ km/s).

[3]We use this form since it is the potential of a self-gravitating disk. Although we do not incorporate self-gravity of the gas in these simple setups, by choosing this potential we could easily include self-gravity if we so chose.

We inject CRs into the centers of these distributions, once with a broad 750 pc width gaussian, and once with a narrow 100 pc gaussian of the same total energy injection rate. The resulting time evolution for each run is shown in figure 4.3. For all but the last of these simulations, the central region is largely unaffected, with CR pressure gradients causing small acceleration of gas in the sparse outskirts. The narrow-scale CR injection with streaming shows instead a significant effect in the central disk region, although we note that a higher resolution may be necessary here.

4.2.3 Isolated Galaxy Formation

We initialize our isolated galaxy simulations with a fixed NFW dark matter potential, and a sphere of gas in hydrostatic equilibrium with a small amount of rotation. Radiative cooling and star formation begin with the onset of the simulation, and the gas collapses into a disk. For each halo mass we perform four simulations, each with a different method of CR feedback. In the first of these we include no CR production, and all feedback is thermal. In the second we include CR injection, but do not include any CR transport other than passive advection with the background gas (i.e. no streaming and no diffusion). In the third the CRs diffuse with a constant diffusion coefficient $\kappa = 3 \times 10^{28}$ cm^2 s^{-1}, and in the fourth they stream out at the Alfvén speed, determined by a constant

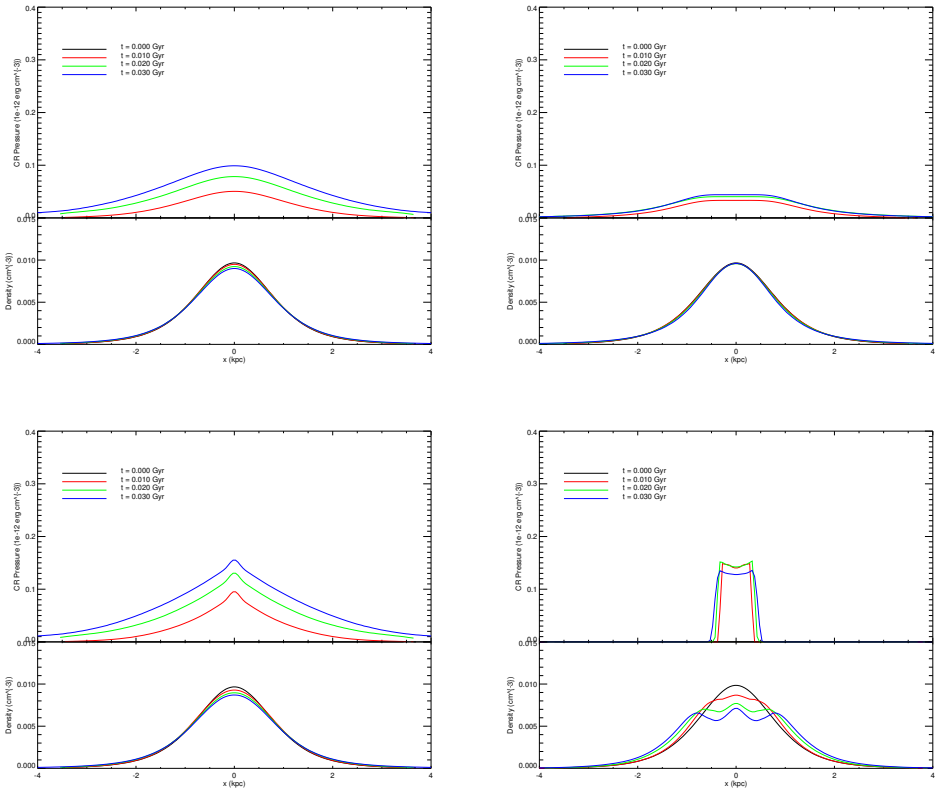

Figure 4.3: CR pressure and density profiles for the stratified tube diffusion (left) and streaming (right) simulations, with CRs injected on broad (top) and narrow (bottom) length scales.

magnitude B-field. B-field orientation is *not* taken into account here - CRs will always stream at the Alfvén speed in the direction of their pressure gradient.

Some snapshots of these simulations after 1 Gyr of star formation for a 10^{10} $M_{\odot}$ halo are shown below. Figure 4.4 displays the gas density in vertical slices through the disk center, and 4.5 displays the vertical velocity. Figure 4.6 shows the total mass contained within the virial radius $R_{\rm vir}$ of the halo, as well as how much of this mass is contained in gas versus stars.

Note that there is an overall mass loss even in simulations without CRs. This is due to the slight excess of energy in the equator of the initial gas setup due to the rotation, and is an artifact of the fixed gravitational potential we use - simulating a live dark matter halo greatly reduces this mass loss. Discussion of CR driven outflows will therefore be defined relative to this unphysical mass loss.

Consider first the simulation without CRs. By 1 Gyr the gas has formed a disk, and gas continues to fall into the disk, continually forming stars at a large rate. Compare this to the case with CRs but no CR transport. In this case, CRs are injected in the disk, but essentially cannot leave it. They thus act as an additional source of pressure support for the disk, puffing it up (compare top two plots of figure 4.4). Gas still falls into the disk (top two plots of figure 4.5), but because the disk itself is less dense here the star formation rate is much lower (top two plots of figure 4.6).

Now consider the case with CR streaming. As CRs are able to leave the disk they are capable of driving outflow of material (see bottom left of figure 4.5). However, these winds are launched at large heights above the disk, where the density is low, and so although the star formation rate is noticeably reduced, the mass loss out of the virial radius is not significantly greater than in the case without CRs (left two plots of figure 4.6).

The simulation with CR diffusion, in stark contrast, shows a strong wind launched much lower in the disk, driving a significant amount of mass loss from the halo (bottom right of figures 4.5 and 4.6). This effect is so strong that it alters the shape of the galaxy (bottom right of figure 4.4).

Unfortunately it is difficult to draw conclusions at this stage, as outflow and star formation will ultimately depend on the diffusion coefficient and magnetic fields we use. But we can tentatively claim that properties of galactic winds do change considerably when CRs evolve via streaming instead of diffusion. It is therefore vital to model the CR transport physics correctly, as well as determine where the CRs are self-confined and where they are not.

4.3 Conclusions

We have introduced a series of simple simulations of increasing physical complexity which demonstrate the dynamical differences between CR streaming and

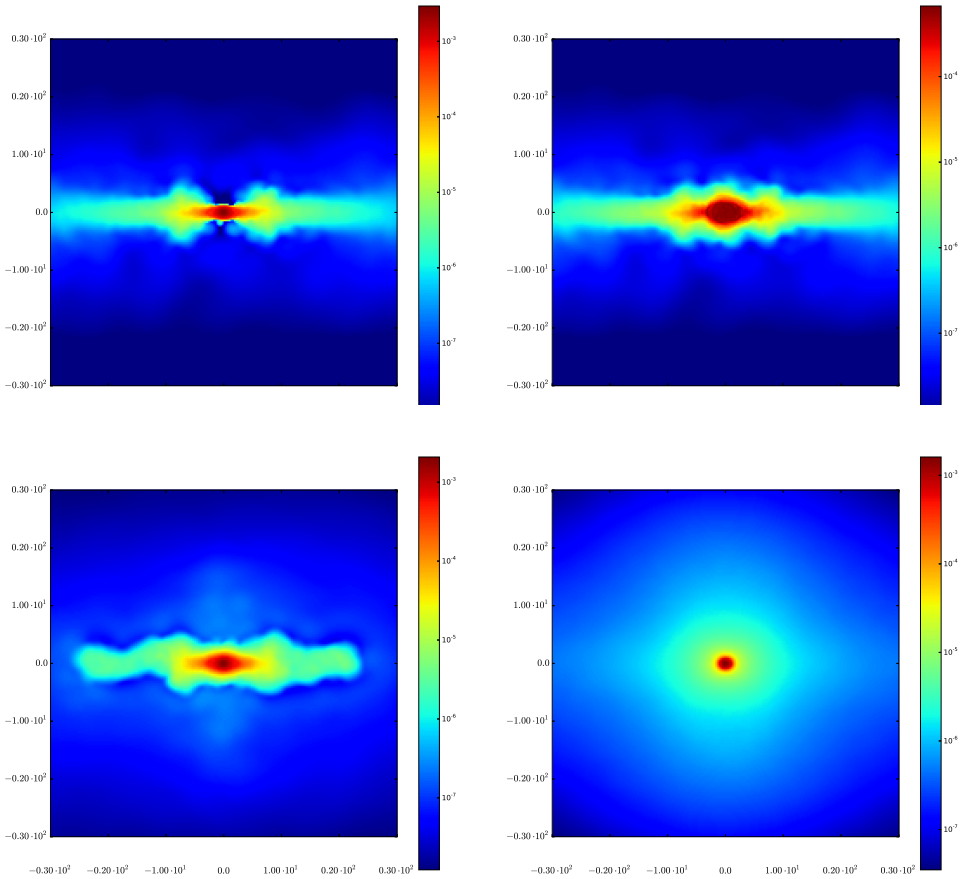

Figure 4.4: Vertical slices through the 10^{10} $M_{\odot}$ halo for the four different simulations, displaying density. Distances on the x and y axes are in kpc. Top left: No CRs. Top Right: CRs with advective transport only. Bottom left: CRs streaming at the Alfvén speed. Bottom right: CRs diffusing with constant diffusion coefficient.

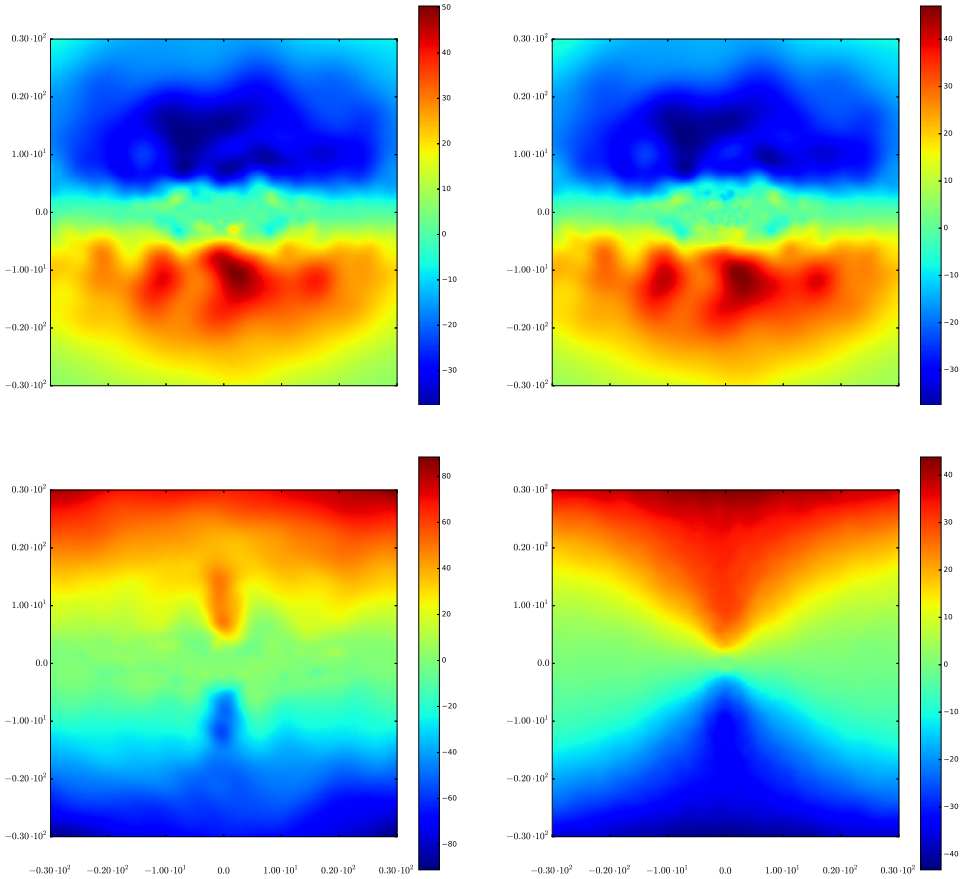

Figure 4.5: Vertical slices through the 10^{10} $M_{\odot}$ halo for the four different simulations, displaying vertical velocity in km/s. Distances on the x and y axes are in kpc. Top left: No CRs. Top Right: CRs with advective trapnsport only. Bottom left: CRs streaming at the Alfvén speed. Bottom right: CRs diffusing with constant diffusion coefficient.

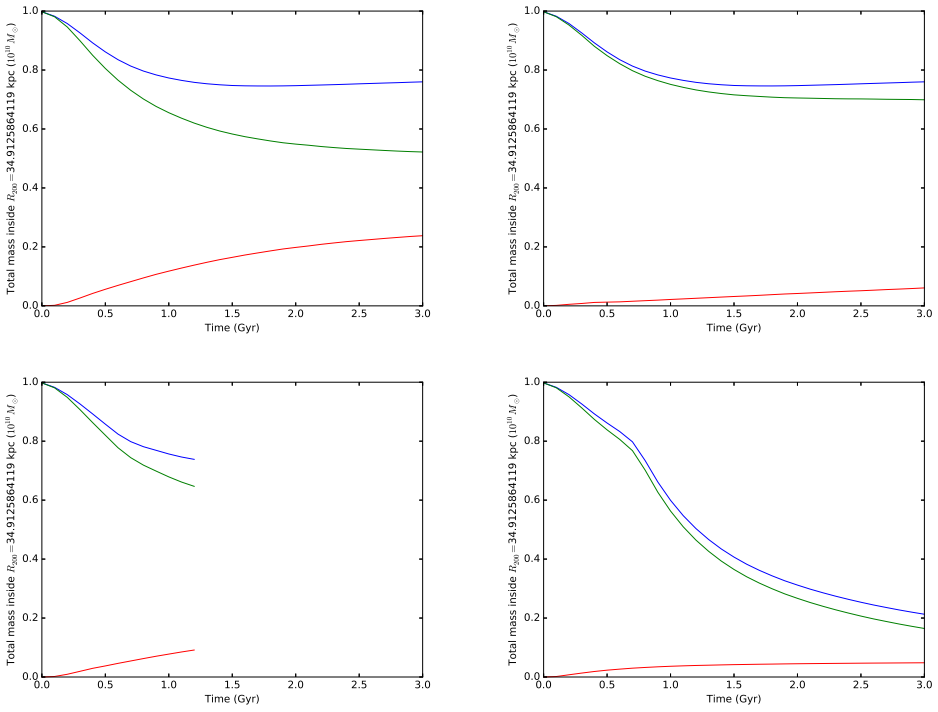

Figure 4.6: Total mass within the virial radius $R_{\rm vir}$ as a function of time for the 10^{10} $M_\odot$ halo for the four different simulations, normalized to the initial mass. Combined gas and stellar mass is shown as the blue lines. Gas mass is displayed in the green lines, and stellar mass in the red lines. Top left: No CRs. Top Right: CRs with advective trapnsport only. Bottom left: CRs streaming at the Alfvén speed. Bottom right: CRs diffusing with constant diffusion coefficient.

CR diffusion. In the simplest scenario of a gaussian peak of CR pressure expanding into a homogeneous background, the differences between streaming and diffusion are evident. The evolution of the CR pressure profile itself is qualitatively different when CR transport is dictated by streaming versus when it is dictated by diffusion. In addition, the extra energy coupling from the wave heating term causes a larger density perturbation in the streaming case.

Simulations of a gravitationally stratified disk with plane-parallel symmetry show less clear differences that strongly depend on the length scale of CR injection. More needs to be done for a full understanding of the physics.

Lastly, we simulated an isolated 10^{10} $M_{\odot}$ galactic halo that forms under gravitational collapse. We showed that injection of CRs will regulate the star formation rate regardless of transport mechanism, but the level of regulation may depend strongly on the kind of transport used. Simulations which use streaming or diffusion both generate outflowing galactic winds, but CRs evolving with diffusion blew out a much larger amount of mass than CRs evolving with streaming. Although it remains to be seen how these wind properties depend on parameters such as halo mass, diffusion coefficient, or magnetic field, it is clear that different treatments give different results. As such we highly emphasize the importance of incorporating correct CR transport physics in galactic wind simulations.

4.4 Appendix: Simulations without Hydrodynamics

To perform the simplest possible tests of the Gadget-2 code, we ran simulations with no hydrodynamics. These runs test solely the evolution of the CR quantities. We start with a uniform background gas and a gaussian CR specific energy, with $\alpha = 2.5$ and $q_0 = 10$. This setup is then evolved using a) a constant diffusion coefficient, and b) a constant streaming speed.

For constant diffusion, the solution is analytic. A gaussian profile with initial width σ_0 undergoing constant diffusion with diffusion coefficient κ will simply spread out in time, according to

$$E_{\rm cr}(x,t) = E_{\rm cr,max}\sqrt{\frac{\sigma_0^2}{\sigma_0^2 + 2\kappa t}}\exp\left(\frac{-x^2}{2(\sigma_0^2 + 2\kappa t)}\right). \tag{4.11}$$

The top plot of figure 4.7 shows the simulation result, compared with the analytic result above. The match is perfect, with the small deviation in the outermost regions being attributed to the periodicity of the simulation box - CRs which would normally leave the domain simply build up near the edges.

The streaming case has no analytic solution, but we can compare it to other numerical codes. The bottom plot of figure 4.7 shows the streaming result, compared with the same setup evolved in a modified version of the ZEUS code (see

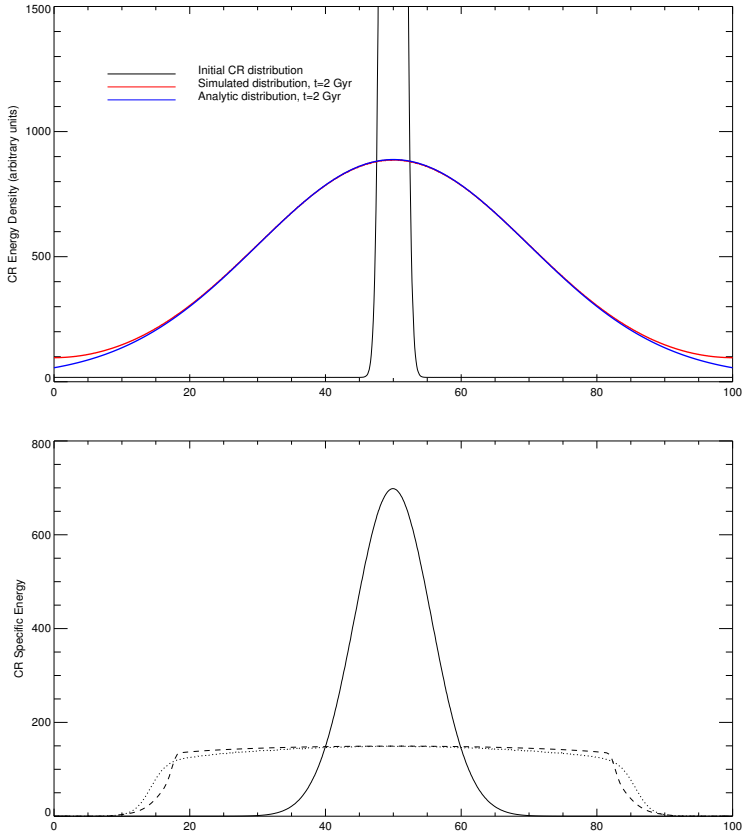

Figure 4.7: Initial gaussian $E_{\rm cr}$ distribution evolving with a constant diffusion coefficient (top) and with constant streaming speed (bottom). In the top plot the simulation result is compared with the analytic evolution from equation (4.11). In the bottom plot, the results (dotted line) are compared with those of the ZEUS grid code in 1D (dashed line).

[51]). Again, the results match well, although the GADGET-2 result is more diffusive. This behavior is expected in an SPH code, and was in fact seen in [107].

Bibliography

[1] A. Achterberg. On the propagation of relativistic particles in a high beta plasma. *A&A*, 98:161–172, May 1981.

[2] J. Aleksić, E. A. Alvarez, L. A. Antonelli, P. Antoranz, M. Asensio, M. Backes, U. Barres de Almeida, J. A. Barrio, D. Bastieri, J. Becerra González, W. Bednarek, A. Berdyugin, K. Berger, E. Bernardini, A. Biland, O. Blanch, R. K. Bock, A. Boller, G. Bonnoli, D. Borla Tridon, I. Braun, T. Bretz, A. Cañellas, E. Carmona, A. Carosi, P. Colin, E. Colombo, J. L. Contreras, J. Cortina, L. Cossio, S. Covino, F. Dazzi, A. de Angelis, G. de Caneva, E. de Cea Del Pozo, B. de Lotto, C. Delgado Mendez, A. Diago Ortega, M. Doert, A. Domínguez, D. Dominis Prester, D. Dorner, M. Doro, D. Eisenacher, D. Elsaesser, D. Ferenc, M. V. Fonseca, L. Font, C. Fruck, R. J. García López, M. Garczarczyk, D. Garrido, G. Giavitto, N. Godinović, S. R. Gozzini, D. Hadasch, D. Häfner, A. Herrero, D. Hildebrand, D. Höhne-Mönch, J. Hose, D. Hrupec, T. Jogler,

H. Kellermann, S. Klepser, T. Krähenbühl, J. Krause, J. Kushida, A. La Barbera, D. Lelas, E. Leonardo, N. Lewandowska, E. Lindfors, S. Lombardi, M. López, R. López, A. López-Oramas, E. Lorenz, M. Makariev, G. Maneva, N. Mankuzhiyil, K. Mannheim, L. Maraschi, M. Mariotti, M. Martínez, D. Mazin, M. Meucci, J. M. Miranda, R. Mirzoyan, J. Moldón, A. Moralejo, P. Munar-Adrover, A. Niedzwiecki, D. Nieto, K. Nilsson, N. Nowak, R. Orito, S. Paiano, D. Paneque, R. Paoletti, S. Pardo, J. M. Paredes, S. Partini, M. A. Perez-Torres, M. Persic, L. Peruzzo, M. Pilia, J. Pochon, F. Prada, P. G. Prada Moroni, E. Prandini, I. Puerto Gimenez, I. Puljak, I. Reichardt, R. Reinthal, W. Rhode, M. Ribó, J. Rico, S. Rügamer, A. Saggion, K. Saito, T. Y. Saito, M. Salvati, K. Satalecka, V. Scalzotto, V. Scapin, C. Schultz, T. Schweizer, M. Shayduk, S. N. Shore, A. Sillanpää, J. Sitarek, I. Snidaric, D. Sobczynska, F. Spanier, S. Spiro, V. Stamatescu, A. Stamerra, B. Steinke, J. Storz, N. Strah, S. Sun, T. Surić, L. Takalo, H. Takami, F. Tavecchio, P. Temnikov, T. Terzić, D. Tescaro, M. Teshima, O. Tibolla, D. F. Torres, A. Treves, M. Uellenbeck, H. Vankov, P. Vogler, R. M. Wagner, Q. Weitzel, V. Zabalza, F. Zandanel, R. Zanin, MAGIC Collaboration, C. Pfrommer, and A. Pinzke. Constraining cosmic rays and magnetic fields in the Perseus galaxy cluster with TeV observations by the MAGIC telescopes. *A&A*, 541:A99, May 2012.

[3] T. Arlen, T. Aune, M. Beilicke, W. Benbow, A. Bouvier, J. H. Buckley, V. Bugaev, K. Byrum, A. Cannon, A. Cesarini, L. Ciupik, E. Collins-Hughes, M. P. Connolly, W. Cui, R. Dickherber, J. Dumm, A. Falcone, S. Federici, Q. Feng, J. P. Finley, G. Finnegan, L. Fortson, A. Furniss, N. Galante, D. Gall, S. Godambe, S. Griffin, J. Grube, G. Gyuk, J. Holder, H. Huan, G. Hughes, T. B. Humensky, A. Imran, P. Kaaret, N. Karlsson, M. Kertzman, Y. Khassen, D. Kieda, H. Krawczynski, F. Krennrich, K. Lee, A. S. Madhavan, G. Maier, P. Majumdar, S. McArthur, A. McCann, P. Moriarty, R. Mukherjee, T. Nelson, A. O'Faoláin de Bhróithe, R. A. Ong, M. Orr, A. N. Otte, N. Park, J. S. Perkins, M. Pohl, H. Prokoph, J. Quinn, K. Ragan, L. C. Reyes, P. T. Reynolds, E. Roache, J. Ruppel, D. B. Saxon, M. Schroedter, G. H. Sembroski, C. Skole, A. W. Smith, I. Telezhinsky, G. Tešić, M. Theiling, S. Thibadeau, K. Tsurusaki, A. Varlotta, M. Vivier, S. P. Wakely, J. E. Ward, A. Weinstein, R. Welsing, D. A. Williams, B. Zitzer, C. Pfrommer, and A. Pinzke. Constraints on Cosmic Rays, Magnetic Fields, and Dark Matter from Gamma-Ray Observations of the Coma Cluster of Galaxies with VERITAS and Fermi. *ApJ*, 757:123, October 2012.

[4] M. Asplund, N. Grevesse, A. J. Sauval, and P. Scott. The Chemical Composition of the Sun. *ARA&A*, 47:481–522, September 2009.

[5] S. A. Balbus. Stability, Instability, and "Backward" Transport in Stratified Fluids. *ApJ*, 534:420–427, May 2000.

[6] N. Battaglia, J. R. Bond, C. Pfrommer, and J. L. Sievers. On the Cluster Physics of Sunyaev-Zel'dovich and X-Ray Surveys. I. The Influence of Feedback, Non-thermal Pressure, and Cluster Shapes on Y-M Scaling Relations. *ApJ*, 758:74, October 2012.

[7] A. R. Bell. The acceleration of cosmic rays in shock fronts. II. *MNRAS*, 182:443–455, February 1978.

[8] A. R. Bell. Turbulent amplification of magnetic field and diffusive shock acceleration of cosmic rays. *MNRAS*, 353:550–558, September 2004.

[9] A. Beresnyak and A. Lazarian. Wave Decay in Magnetohydrodynamic Turbulence. *ApJ*, 678:961–967, May 2008.

[10] V. S. Berezinsky, P. Blasi, and V. S. Ptuskin. Clusters of Galaxies as Storage Room for Cosmic Rays. *ApJ*, 487:529–+, October 1997.

[11] K. Beuermann, G. Kanbach, and E. M. Berkhuijsen. Radio structure of the Galaxy - Thick disk and thin disk at 408 MHz. *A&A*, 153:17–34, December 1985.

[12] R. Blandford and D. Eichler. Particle acceleration at astrophysical shocks: A theory of cosmic ray origin. *Phys. Rep.*, 154:1–75, October 1987.

[13] H. Boehringer and G. E. Morfill. On the dynamical role of cosmic rays in cooling flows in clusters of galaxies. *ApJ*, 330:609–619, July 1988.

[14] A. Bonafede, L. Feretti, M. Murgia, F. Govoni, G. Giovannini, D. Dallacasa, K. Dolag, and G. B. Taylor. The Coma cluster magnetic field from Faraday rotation measures. *A&A*, 513:A30, April 2010.

[15] A. Bonafede, F. Govoni, L. Feretti, M. Murgia, G. Giovannini, and M. Brüggen. Fractional polarization as a probe of magnetic fields in the intra-cluster medium. *A&A*, 530:A24, June 2011.

[16] D. Breitschwerdt, J. F. McKenzie, and H. J. Voelk. Galactic winds. I - Cosmic ray and wave-driven winds from the Galaxy. *A&A*, 245:79–98, May 1991.

[17] U. G. Briel, J. P. Henry, and H. Boehringer. Observation of the Coma cluster of galaxies with ROSAT during the all-sky survey. *A&A*, 259:L31–L34, June 1992.

[18] S. Brown, A. Emerick, L. Rudnick, and G. Brunetti. Probing the Off-state of Cluster Giant Radio Halos. *ApJ*, 740:L28, October 2011.

[19] S. Brown and L. Rudnick. Diffuse radio emission in/around the Coma cluster: beyond simple accretion. *MNRAS*, 412:2–12, March 2011.

[20] G. Brunetti, P. Blasi, O. Reimer, L. Rudnick, A. Bonafede, and S. Brown. Probing the origin of giant radio haloes through radio and γ-ray data: the case of the Coma cluster. *MNRAS*, 426:956–968, October 2012.

[21] G. Brunetti, S. Giacintucci, R. Cassano, W. Lane, D. Dallacasa, T. Venturi, N. E. Kassim, G. Setti, W. D. Cotton, and M. Markevitch. A low-frequency radio halo associated with a cluster of galaxies. *Nat*, 455:944–947, October 2008.

[22] G. Brunetti and A. Lazarian. Compressible turbulence in galaxy clusters: physics and stochastic particle re-acceleration. *MNRAS*, 378:245–275, June 2007.

[23] G. Brunetti, G. Setti, L. Feretti, and G. Giovannini. Particle reacceleration in the Coma cluster: radio properties and hard X-ray emission. *MNRAS*, 320:365–378, January 2001.

[24] P. R. Capelo, P. S. Coppi, and P. Natarajan. The polytropic approximation and X-ray scaling relations: constraints on gas and dark matter profiles for galaxy groups and clusters. *MNRAS*, 422:686–703, May 2012.

[25] B. D. G. Chandran. Scattering of Energetic Particles by Anisotropic Magnetohydrodynamic Turbulence with a Goldreich-Sridhar Power Spectrum. *Physical Review Letters*, 85:4656–4659, November 2000.

[26] B. D. G. Chandran and Y. Rasera. Convection and AGN Feedback in Clusters of Galaxies. *ApJ*, 671:1413–1433, December 2007.

[27] C. H. K. Chen, A. Mallet, T. A. Yousef, A. A. Schekochihin, and T. S. Horbury. Anisotropy of Alfvénic turbulence in the solar wind and numerical simulations. *MNRAS*, 415:3219–3226, August 2011.

[28] J. Cho and A. Lazarian. Compressible magnetohydrodynamic turbulence: mode coupling, scaling relations, anisotropy, viscosity-damped regime and astrophysical implications. *MNRAS*, 345:325–339, October 2003.

[29] J. Cho and E. T. Vishniac. The Anisotropy of Magnetohydrodynamic Alfvénic Turbulence. *ApJ*, 539:273–282, August 2000.

[30] E. Churazov, W. Forman, C. Jones, and H. Böhringer. XMM-Newton Observations of the Perseus Cluster. I. The Temperature and Surface Brightness Structure. *ApJ*, 590:225–237, June 2003.

[31] P. Creasey, T. Theuns, R. G. Bower, and C. G. Lacey. Numerical overcooling in shocks. *MNRAS*, 415:3706–3720, August 2011.

[32] R. M. Crutcher, B. Wandelt, C. Heiles, E. Falgarone, and T. H. Troland. Magnetic Fields in Interstellar Clouds from Zeeman Observations: Inference of Total Field Strengths by Bayesian Analysis. *ApJ*, 725:466–479, December 2010.

[33] B. De Pontieu, P. C. H. Martens, and H. S. Hudson. Chromospheric Damping of Alfvén Waves. *ApJ*, 558:859–871, September 2001.

[34] B. M. Deiss, W. Reich, H. Lesch, and R. Wielebinski. The large-scale structure of the diffuse radio halo of the coma cluster at 1.4ghz. *A&A*, 321:55–63, May 1997.

[35] Y. Dubois and R. Teyssier. Cosmological MHD simulation of a cooling flow cluster. *A&A*, 482:L13–L16, May 2008.

[36] T. Enßlin, C. Pfrommer, F. Miniati, and K. Subramanian. Cosmic ray transport in galaxy clusters: implications for radio halos, gamma-ray signatures, and cool core heating. *A&A*, 527:A99+, March 2011.

[37] T. A. Enßlin, P. L. Biermann, P. P. Kronberg, and X.-P. Wu. Cosmic-Ray Protons and Magnetic Fields in Clusters of Galaxies and Their Cosmological Consequences. *ApJ*, 477:560, March 1997.

[38] T. A. Enßlin, C. Pfrommer, V. Springel, and M. Jubelgas. Cosmic ray physics in calculations of cosmological structure formation. *A&A*, 473:41–57, October 2007.

[39] T. A. Ensslin, Y. Wang, B. B. Nath, and P. L. Biermann. Black hole energy release to the Gaseous Universe. *A&A*, 333:L47–L50, May 1998.

[40] J. E. Everett and E. G. Zweibel. The Interaction of Cosmic Rays with Diffuse Clouds. *ApJ*, 739:60, October 2011.

[41] J. E. Everett, E. G. Zweibel, R. A. Benjamin, and et al. The Milky Way's Kiloparsec-Scale Wind: A Hybrid Cosmic-Ray and Thermally Driven Outflow. *ApJ*, 674:258–270, February 2008.

[42] A. J. Farmer and P. Goldreich. Wave Damping by Magnetohydrodynamic Turbulence and Its Effect on Cosmic-Ray Propagation in the Interstellar Medium. *ApJ*, 604:671–674, April 2004.

[43] G. M. Felice and R. M. Kulsrud. Cosmic-Ray Pitch-Angle Scattering through 90 Degrees. *ApJ*, 553:198–210, May 2001.

[44] L. Feretti, G. Giovannini, F. Govoni, and M. Murgia. Clusters of galaxies: observational properties of the diffuse radio emission. *AAPR*, 20:54, May 2012.

[45] G. J. Ferland, A. C. Fabian, N. A. Hatch, R. M. Johnstone, R. L. Porter, P. A. M. van Hoof, and R. J. R. Williams. The origin of molecular hydrogen emission in cooling-flow filaments. *MNRAS*, 386:L72–L76, May 2008.

[46] G. J. Ferland, A. C. Fabian, N. A. Hatch, R. M. Johnstone, R. L. Porter, P. A. M. van Hoof, and R. J. R. Williams. Collisional heating as the origin of filament emission in galaxy clusters. *MNRAS*, 392:1475–1502, February 2009.

[47] K. M. Ferrière. The interstellar environment of our galaxy. *RvMP*, 73:1031–1066, October 2001.

[48] E. A. Foote and R. M. Kulsrud. Hydromagnetic waves in high Beta plasmas. *ApJ*, 233:302–316, October 1979.

[49] O. Gnat and A. Sternberg. Time-dependent Ionization in Radiatively Cooling Gas. *ApJS*, 168:213–230, February 2007.

[50] P. Goldreich and S. Sridhar. Toward a theory of interstellar turbulence. 2: Strong alfvenic turbulence. *ApJ*, 438:763–775, January 1995.

[51] F. Guo and S. P. Oh. Feedback heating by cosmic rays in clusters of galaxies. *MNRAS*, 384:251–266, February 2008.

[52] L. M. Haffner, R.-J. Dettmar, J. E. Beckman, and et al. The warm ionized medium in spiral galaxies. *RvMP*, 81:969–997, July 2009.

[53] M. Hanasz, H. Lesch, T. Naab, A. Gawryszczak, K. Kowalik, and D. Wóltański. Cosmic Rays Can Drive Strong Outflows from Gas-rich High-redshift Disk Galaxies. *ApJ*, 777:L38, November 2013.

[54] G. D. Holman, J. A. Ionson, and J. S. Scott. Particle streaming - Is the Alfven velocity the ultimate speed limit. *ApJ*, 228:576–581, March 1979.

[55] T. S. Horbury, M. Forman, and S. Oughton. Anisotropic Scaling of Magnetohydrodynamic Turbulence. *Physical Review Letters*, 101(17):175005, October 2008.

[56] W. J. Jaffe. Origin and transport of electrons in the halo radio source in the Coma cluster. *ApJ*, 212:1–7, February 1977.

[57] P. Kuchar and T. A. Enßlin. Magnetic power spectra from Faraday rotation maps. REALMAF and its use on Hydra A. *A&A*, 529:A13, May 2011.

[58] R. Kulsrud and W. P. Pearce. The Effect of Wave-Particle Interactions on the Propagation of Cosmic Rays. *ApJ*, 156:445–+, May 1969.

[59] R. M. Kulsrud. Propagation of cosmic rays through a plasma. In A. Reiz and T. Andersen, editors, *Astronomical Papers Dedicated to Bengt Stromgren*, pages 317–326, 1978.

[60] R. M. Kulsrud. *Plasma physics for astrophysics*. Princeton University Press, 2005.

[61] R. M. Kulsrud and C. J. Cesarsky. The Effectiveness of Instabilities for the Confinement of High Energy Cosmic Rays in the Galactic Disk. *Astrophys. Lett.*, 8:189, March 1971.

[62] M. W. Kunz, A. A. Schekochihin, S. C. Cowley, J. J. Binney, and J. S. Sanders. A thermally stable heating mechanism for the intracluster medium: turbulence, magnetic fields and plasma instabilities. *MNRAS*, 410:2446–2457, February 2011.

[63] M. A. Lee and H. J. Völk. Damping and Non-Linear Wave-Particle Interactions of Alfvén-Waves in the Solar Wind. *Astrophysics and Space Science*, 24:31–49, September 1973.

[64] I. Lerche. Unstable Magnetosonic Waves in a Relativistic Plasma. *ApJ*, 147:689–+, February 1967.

[65] Y. Lithwick and P. Goldreich. Compressible Magnetohydrodynamic Turbulence in Interstellar Plasmas. *ApJ*, 562:279–296, November 2001.

[66] M. Loewenstein, E. G. Zweibel, and M. C. Begelman. Cosmic-ray heating of cooling flows - A critical analysis. *ApJ*, 377:392–402, August 1991.

[67] C. Loken, M. L. Norman, E. Nelson, J. Burns, G. L. Bryan, and P. Motl. A Universal Temperature Profile for Galaxy Clusters. *ApJ*, 579:571–576, November 2002.

[68] K. Mannheim and R. Schlickeiser. Interactions of cosmic ray nuclei. *A&A*, 286:983–996, June 1994.

[69] J. Maron and P. Goldreich. Simulations of Incompressible Magnetohydrodynamic Turbulence. *ApJ*, 554:1175–1196, June 2001.

[70] J. F. McKenzie and H. J. Voelk. Self-consistent shock structure in the presence of cosmic rays and Alfven waves. In *International Cosmic Ray Conference*, volume 9 of *International Cosmic Ray Conference*, page 242, November 1981.

[71] B. R. McNamara and P. E. J. Nulsen. Heating Hot Atmospheres with Active Galactic Nuclei. *ARA&A*, 45:117–175, September 2007.

[72] J. A. Miller. Magnetohydrodynamic turbulence dissipation and stochastic proton acceleration in solar flares. *ApJ*, 376:342–354, July 1991.

[73] F. Miniati, D. Ryu, H. Kang, and T. W. Jones. Cosmic-Ray Protons Accelerated at Cosmological Shocks and Their Impact on Groups and Clusters of Galaxies. *ApJ*, 559:59–69, September 2001.

[74] A. H. Minter and S. R. Spangler. Heating of the Interstellar Diffuse Ionized Gas via the Dissipation of Turbulence. *ApJ*, 485:182, August 1997.

[75] O. Nachtmann. *Elementary particle physics: Concepts and phenomena*. Springer, 1990.

[76] S. V. Nazarenko and A. A. Schekochihin. Critical balance in magnetohydrodynamic, rotating and stratified turbulence: towards a universal scaling conjecture. *Journal of Fluid Mechanics*, 677:134–153, June 2011.

[77] I. J. Parrish, E. Quataert, and P. Sharma. Anisotropic Thermal Conduction and the Cooling Flow Problem in Galaxy Clusters. *ApJ*, 703:96–108, September 2009.

[78] I. J. Parrish, J. M. Stone, and N. Lemaster. The Magnetothermal Instability in the Intracluster Medium. *ApJ*, 688:905–917, December 2008.

[79] A. Pedlar, H. S. Ghataure, R. D. Davies, B. A. Harrison, R. Perley, P. C. Crane, and S. W. Unger. The Radio Structure of NGC1275. *MNRAS*, 246:477, October 1990.

[80] V. Petrosian. On the Nonthermal Emission and Acceleration of Electrons in Coma and Other Clusters of Galaxies. *ApJ*, 557:560–572, August 2001.

[81] C. Pfrommer. Simulating cosmic rays in clusters of galaxies - III. Non-thermal scaling relations and comparison to observations. *MNRAS*, 385:1242–1256, April 2008.

[82] C. Pfrommer and J.L. Dursi. Detecting the orientation of magnetic fields in galaxy clusters. *Nature Physics*, 6:520–526, July 2010.

[83] C. Pfrommer and T. A. Enßlin. Constraining the population of cosmic ray protons in cooling flow clusters with γ-ray and radio observations: Are radio mini-halos of hadronic origin? *A&A*, 413:17–36, January 2004.

[84] C. Pfrommer, T. A. Enßlin, and V. Springel. Simulating cosmic rays in clusters of galaxies - II. A unified scheme for radio haloes and relics with predictions of the γ-ray emission. *MNRAS*, 385:1211–1241, April 2008.

[85] A. Pinzke and C. Pfrommer. Simulating the γ-ray emission from galaxy clusters: a universal cosmic ray spectrum and spatial distribution. *MNRAS*, 409:449–480, December 2010.

[86] J. J. Podesta. Dependence of Solar-Wind Power Spectra on the Direction of the Local Mean Magnetic Field. *ApJ*, 698:986–999, June 2009.

[87] R. J. Rand. A Very Deep Spectrum of the Diffuse Ionized Gas in NGC 891. *ApJ*, 474:129, January 1997.

[88] R. J. Rand. Further Spectroscopy of the Diffuse Ionized Gas in NGC 891 and Evidence for a Secondary Source of Ionization. *ApJ*, 501:137, July 1998.

[89] J. C. Raymond. Microflare heating of the galactic halo. *ApJ*, 384:502–507, January 1992.

[90] P. Rebusco, E. Churazov, H. Böhringer, and W. Forman. Effect of turbulent diffusion on iron abundance profiles. *MNRAS*, 372:1840–1850, November 2006.

[91] R. J. Reynolds, L. M. Haffner, and S. L. Tufte. Evidence for an Additional Heat Source in the Warm Ionized Medium of Galaxies. *ApJ*, 525:L21–L24, November 1999.

[92] M. A. Riquelme and A. Spitkovsky. Nonlinear Study of Bell's Cosmic Ray Current-Driven Instability. *ApJ*, 694:626–642, March 2009.

[93] M. Ruszkowski, D. Lee, M. Brüggen, I. Parrish, and S. P. Oh. Cosmological Magnetohydrodynamic Simulations of Cluster Formation with Anisotropic Thermal Conduction. *ApJ*, 740:81, October 2011.

[94] M. Ruszkowski and S. P. Oh. Shaken and Stirred: Conduction and Turbulence in Clusters of Galaxies. *ApJ*, 713:1332–1342, April 2010.

[95] M. Ruszkowski and S. P. Oh. Galaxy motions, turbulence and conduction in clusters of galaxies. *MNRAS*, 414:1493–1507, June 2011.

[96] G. B. Rybicki and A. P. Lightman. *Radiative Processes in Astrophysics*. New York: Wiley, 1979.

[97] M. Salem and G. L. Bryan. Cosmic ray driven outflows in global galaxy disc models. *MNRAS*, 437:3312–3330, February 2014.

[98] M. Salem, G. L. Bryan, and C. Hummels. Cosmological Simulations of Galaxy Formation with Cosmic Rays. *ApJ*, 797:L18, December 2014.

[99] R. Schlickeiser. *Cosmic Ray Astrophysics*. Berlin: Springer, 2002.

[100] C. Shang and S. P. Oh. Disentangling Resonant Scattering and Gas Motions in Galaxy Cluster Emission Line Profiles. *ArXiv e-prints*, November 2012.

[101] C. Shang and S. P. Oh. Probing gas motions in the intra-cluster medium: a mixture model approach. *MNRAS*, 426:3435–3454, November 2012.

[102] P. Sharma, B. D. G. Chandran, E. Quataert, and I. J. Parrish. Buoyancy Instabilities in Galaxy Clusters: Convection Due to Adiabatic Cosmic Rays and Anisotropic Thermal Conduction. *ApJ*, 699:348–361, July 2009.

[103] P. Sharma, P. Colella, and D. F. Martin. Numerical Implementation of Streaming Down the Gradient: Application to Fluid Modeling of Cosmic Rays. *SIAM J. of Scient. Comp.*, 32:3564, September 2010.

[104] L. D. Shaw, D. Nagai, S. Bhattacharya, and E. T. Lau. Impact of Cluster Physics on the Sunyaev-Zel'dovich Power Spectrum. *ApJ*, 725:1452–1465, December 2010.

[105] J. Skilling. Cosmic Rays in the Galaxy: Convection or Diffusion? *ApJ*, 170:265–+, December 1971.

[106] L. Spitzer, Jr. and M. G. Tomasko. Heating of H i Regions by Energetic Particles. *ApJ*, 152:971, June 1968.

[107] M. Uhlig, C. Pfrommer, M. Sharma, B. B. Nath, T. A. Enßlin, and V. Springel. Galactic winds driven by cosmic ray streaming. *MNRAS*, 423:2374–2396, July 2012.

[108] H. J. Voelk, L. O. Drury, and J. F. McKenzie. Hydrodynamic estimates of cosmic ray acceleration efficiencies in shock waves. *A&A*, 130:19–28, January 1984.

[109] H. J. Völk, F. A. Aharonian, and D. Breitschwerdt. The Nonthermal Energy Content and Gamma-Ray Emission of Starburst Galaxies and Clusters of Galaxies. *Space Science Reviews*, 75:279–297, January 1996.

[110] B. P. Wakker, B. D. Savage, A. J. Fox, R. A. Benjamin, and P. R. Shapiro. Characterizing Transition Temperature Gas in the Galactic Corona. *ApJ*, 749:157, April 2012.

[111] J. C. Weingartner and B. T. Draine. Electron-Ion Recombination on Grains and Polycyclic Aromatic Hydrocarbons. *ApJ*, 563:842–852, December 2001.

[112] D. G. Wentzel. Hydromagnetic Waves Excited by Slowly Streaming Cosmic Rays. *ApJ*, 152:987, June 1968.

[113] D. G. Wentzel. The Propagation and Anisotropy of Cosmic Rays. I. Theory for Steady Streaming. *ApJ*, 156:303–+, April 1969.

[114] D. G. Wentzel. Acceleration and Heating of Interstellar Gas by Cosmic Rays. *ApJ*, 163:503, February 1971.

[115] D. G. Wentzel. Cosmic-ray propagation in the Galaxy - Collective effects. *ARA&A*, 12:71–96, 1974.

[116] R. T. Wicks, T. S. Horbury, C. H. K. Chen, and A. A. Schekochihin. Power and spectral index anisotropy of the entire inertial range of turbulence in the fast solar wind. *MNRAS*, 407:L31–L35, September 2010.

[117] J. Wiener, S. P. Oh, and F. Guo. Cosmic ray streaming in clusters of galaxies. *MNRAS*, 434:2209–2228, September 2013.

[118] H. Yan and A. Lazarian. Scattering of Cosmic Rays by Magnetohydrodynamic Interstellar Turbulence. *Physical Review Letters*, 89:B1102+, December 2002.

[119] H. Yan and A. Lazarian. Cosmic-Ray Scattering and Streaming in Compressible Magnetohydrodynamic Turbulence. *ApJ*, 614:757–769, October 2004.

[120] H. Yan and A. Lazarian. Cosmic-Ray Propagation: Nonlinear Diffusion Parallel and Perpendicular to Mean Magnetic Field. *ApJ*, 673:942–953, February 2008.

[121] F. Zandanel, C. Pfrommer, and F. Prada. On the Physics of Radio Halos in Galaxy Clusters: Scaling Relations and Luminosity Functions. *ArXiv e-prints*, July 2012.

[122] I. Zhuravleva, E. Churazov, A. Kravtsov, and R. Sunyaev. Constraints on the ICM velocity power spectrum from the X-ray lines width and shift. *ArXiv e-prints*, March 2012.

[123] E. G. Zweibel. Cosmic-Ray History and Its Implications for Galactic Magnetic Fields. *ApJ*, 587:625–637, April 2003.

[124] E. G. Zweibel and J. E. Everett. Environments for Magnetic Field Amplification by Cosmic Rays. *ApJ*, 709:1412–1419, February 2010.